Metastabilities in Zn(O,S)-buffered Cu(In,Ga)(S,Se)$_2$ Thin Film Solar Cells

Chua Rou Hua

Interdisciplinary Graduate School, Energy Research Institute @NTU

2016

Metastabilities in Zn(O,S)-buffered $Cu(In,Ga)(S,Se)_2$ Thin Film Solar Cells

Interdisciplinary Graduate School, Energy Research Institute
@NTU

A thesis submitted to the Nanyang Technological University
in partial fulfilment of the requirement for the degree of
Doctor of Philosophy

2016

Abstract

Cu(In,Ga)(S,Se) (CIGSSe) solar cells buffered with zinc oxysulfide (Zn(O,S)) have reached record cell efficiencies of 22.3%. However, the key limitation of Zn(O,S) buffered CIGSSe solar cells comes from its requirement of an extra light soaking step during fabrication, as opposed by conventional Cu(In,Ga)(Se)$_2$ (CIGS) solar cells buffered by toxic cadmium sulfide, which reaches 21.7% cell efficiency. In this thesis, long term thermal ageing tests at 60 °C and 105 °C establish the difference in behavior of CdS buffered versus Zn(O,S) buffered solar cells. During these tests, metastability, in other words *transient* cell efficiency loss recoverable by light soaking, is observed in Zn(O,S) buffered solar cells but not in CdS buffered solar cells. This PhD thesis investigates the mechanism for metastability in zinc oxysulfide (Zn(O,S)) buffered CIGSSe solar cells, and demonstrates a solution to mitigate cell efficiency loss.

In the first part, long term stability tests at 60 °C and 105 °C were performed to compare the ageing behavior of CdS-buffered and Zn(O,S)-buffered CIGSSe solar cells. In addition to the loss of cell efficiency in Zn(O,S) buffered devices an acceleration of cell efficiency relaxation was also observed for Zn(O,S) samples that had previously undergone 1000 h 105 °C thermal ageing. Whereas pristine Zn(O,S) sample relaxed in the time frame of weeks, thermally aged solar cells recovered by light soaking were seen to lose ~70-80% of their original efficiencies in 1–2 days, even at room temperature. X-ray photoemission spectroscopy showed an increase of sulfur in the Zn(O,S) buffer layer after thermal ageing, implying out-diffusion of sulfur from the CIGSSe absorber during the high temperature stability test.

In order to understand the mechanism of cell efficiency loss, Time Resolved Photoluminescence was employed to characterize the minority carrier lifetimes of Zn(O,S) devices of different buffer ratios. Charge separation strength of the *p-n* junction were evaluated for Zn(O,S) devices with different [O]:[S] prepared by atomic layer deposition. Efficient charge separation was found in devices with low sulfur content [O]:[S] of 1:0–4:1. A biexponential decay lifetime, accompanied by high photoluminescence intensity count, was observed in relaxed devices with [O]:[S] of 2:1 and both relaxed and light soaked devices with [O]:[S] of 1:1. Corroborated with one-dimensional electronic band structure simulation results, it was demonstrated for the first time that minority carrier lifetime of Zn(O,S) buffered solar cells were dependent on the sulfur content of the buffer layer. The additional decay lifetime was attributed to radiative recombination in the absorber due to excessive acceptor-type defects in sulfur-rich Zn(O,S) buffer layer that caused a buildup in interface-barrier for charge transport.

Having identified the detrimental effect of sulfur in the Zn(O,S) buffer on metastability, a CIGSSe device with significantly reduced metastability can then be fabricated. A high cell efficiency was obtained by matching the buffer composition of 11% atomic ratio of sulfur to an CIGSSe absorber with surface sulfur/selenium ratio of 3.4. The main accomplishment of this work is to obtain a 16.5% device with negligible metastability by means of depositing a stoichiometrically controlled composition of zinc, oxygen, and sulfur onto an absorber with high surface sulfur content.

Acknowledgements

Prof. Subodh Mhaisalkar and Dr. Lydia Helena Wong for being dedicated professors whom made my PhD journey a fulfilling, memorable and enriching four years. Coming from industry, I definitely appreciated the many discussions from the academic perspective that led to the fruitful development of my PhD thesis.

Dr. Teh Lay Kuan for the time, effort and commitment, always being there for discussions during this duration. I will always remember the amount of time and energy you spent with me, guiding me through this journey from the initial stages until the end. To Dr. Suresh Palale and colleagues at CR/RTC1-AP, thank you for the many things you helped me with and the great time in Robert Bosch SEA Pte Ltd.

The CIGS Group and Staff of ERI@N, NTU for experimental support, discussions, and the fun activities we all enjoyed during various gatherings.

Danken möchte ich Dr. Christoph Treutler für seine fortwährende Unterstützung meiner Doktorarbeit, insbesondere für seine Hilfe zu Beginn des Projekts.

Dr. Jochen Feichtinger, Dr. Siegmund Zweigart und ihren Kollegen in Stuttgart danke ich für ihre freundliche Unterstützung während meiner Aufenthalte in Deutschland und für ihre Beiträge zu meiner Arbeit. Außerdem möchte ich mich dafür bedanken, dass sie den Kontakt zu weiteren wichtigen Ansprechpartnern für meine Experimente ermöglicht haben.

Den Kollegen von Bosch Solar CISTech GmbH, insbesondere Frank Hergert, Frederick Stober, Andrea Wachau und Thomas Hahn danke ich für ihre technische Unterstützung, für wertvolle Diskussionen während vieler Monate, das Bereitstellen von CIGS Material und für ihre Gastfreundschaft während meines Aufenthalts in Brandenburg.

Björn Jakob Müller, Ulrich Berner und Christian Hönes danke ich für die nützlichen Diskussionen über unsere Doktorarbeiten während zahlreicher Telefonkonferenzen.

Bei Prof. Dr. Thomas Walter und Tetiana Lavrenko bedanke ich mich für die besonders freundliche Aufnahme während meiner beiden Aufenthalte an der Hochschule Ulm. Dort habe ich viel über die elektronischen Eigenschaften der CIGS Materialien gelernt, und dafür bedanke ich mich sehr herzlich.

Table of Contents

Table Captions

Figure Captions

Abbreviations

1D	One-dimensional
AES	Auger electron spectroscopy
ALD	Atomic layer deposition
AM1.5G	1000 W/m^2
AS	Admittance spectroscopy
AZO	Aluminum-doped zinc oxide
BC	Back contact
BLS	Blue light soaking
CBD	Chemical bath deposition
CBM	Conduction band minimum
CBO	Conduction band offset
CdS	Cadmium sulfide
C-f	Capacitance-frequency
CIGS	$Cu(In,Ga)Se_2$
CIGSSe	$Cu(In,Ga)(S,Se)_2$
C-V	Capacitance-voltage
DFT	Density functional theory
DLTS	Deep level transient spectroscopy
DrH	Dry heat
EBIC	Electron beam induced current
EDX	Energy dispersive X-ray spectroscopy
EMPA	Swiss Federal Laboratories for Materials Science and Technology
EQE	External quantum efficiency
FIB	Focused ion beam
FLP	Fermi-level pinning
IF	Interface
In_2S_3	Indium sulfide
IPES	Inverse photoelectron spectroscopy

IQE	Internal quantum efficiency
I-V	Current-voltage
I-V-T	Temperature-dependent current-voltage
i-ZnO	Intrinsic zinc oxide
LS	Light soaking
OVC	Ordered vacancy compound
PVD	Physical vapor deposition
QNR	Quasi-neutral region
RLS	Red light soaking
SCAPS-1D	a Solar Cell Capacitance Simulator (one-dimensional)
SCR	Space charge region
SEM	Scanning electron microscopy
SRH	Shockley-Read-Hall
TEM	Transmission electron microscopy
TOF-SIMS	Time-of-flight Secondary ions mass spectrometry
TRPL	Time-resolved photoluminescence
VBM	Valence band maximum
WLS	White light soaking
XPS	X-ray photoelectron spectroscopy
XRF	X-ray fluorescence
Zn(O,S)	Zinc oxysulfide
ZSW	Zentrum für Sonnenenergie und Wasserstoff-Forschung Baden-Württemberg

Symbols

$a*$	1 s^{-1}
b	Bowing parameter
B	Material property constant
C	Capacitance
c_A	Elemental concentration
C_HF	Capacitance at high frequencies
C_LF	Capacitance at low frequencies
D_c	Diffusion coefficient of electrons
D_h	Diffusion coefficient of holes
e	Elemental charge
E_a	Activation energy
E_BE	Binding energy of electrons
E_C	Conduction band minimum
E_F	Fermi level
$\bar{E}_\mathrm{Fn}$	Difference in energy between Fermi level and conduction band minimum
$\bar{E}_\mathrm{Fp}$	Difference in energy between Fermi level and valence band maximum
$\bar{E}_\mathrm{n}$	Demarcation level of electron traps
E_g	Band gap
E_KE	Kinetic energy of emitted photoelectrons
E_t	Defect energy
E_V	Valence band maximum
FF	Fill factor
G	Conductance
$h\nu$	X-ray photon energy
J	X-ray flux
J_0	Saturation current density
J_{00}	Reference current density
J_e	Electron current density
J_h	Hole current density
$J_\mathrm{illum}(V)$	Diode current under illumination
J_mpp	Current density at the maximum power point
$J_\mathrm{ph}(V)$	Photocurrent under illumination

J_{SC}	Short circuit current
K_{s}	Solubility constant
K_{sp}	Solubility product constant
$L_{\mathrm{A}}(\lambda)$	Angular asymmetry parameter of the photoelectron line
L_{e}	Electron diffusion length
L_{h}	Hole diffusion length
$\mathrm{m_e}^*/\mathrm{m_0}$	Electron effective mass
$\mathrm{m_h}^*/\mathrm{m_0}$	Hole effective mass
mpp	Maximum power point of the solar cell output
N1	Shallow defects
N2	Deep defects
N_{a}	Doping density of the *p*-type semiconductors
$N_{\mathrm{A,abs}}$	Net acceptor density in absorber
N_A^-	Ionized acceptor density
N_{C}	Effective density of states in the conduction band
N_{CV}	Doping profile in depleted region
N_{d}	Doping density of the *n*-type semiconductors
N_D^+	Ionized donor density
n_{i}	Intrinsic charge carrier density of a material
n_{id}	Diode quality factor
n_{p0}	*p*-side equilibrium electron density
N_{t}	Defect density
N_{V}	Effective density of states in the valence band
p_{n0}	*n*-side equilibrium hole density
R_{s}	Series resistance
R_{sh}	Shunt resistance
S_{BC}	Recombination velocity of back contact
$S_{\mathrm{e,h}}$	Recombination velocity of electrons or holes
S_i	Sulfur interstitials
R	Recombination rate
T	Temperature
V	Voltage
V_{Cu}	Copper vacancy
V_{dc}	Applied direct current bias
V_{mpp}	Voltage at the maximum power point
V_{OC}	Open circuit voltage
V_{Se}	Selenium vacancy

$v_{\mathrm{th,e,h}}$	Thermal velocity of electrons or holes
V_{Zn}	Zinc vacancies
w_{SCR}	Total space charge region width
x_{n}	Width of the space charge region on the *n*-side
x_{p}	Width of the space charge region on the *p*-side
$\lambda_{\mathrm{A}}(\mathrm{E}_{\mathrm{KE}})$	Inelastic mean free path of electrons
μ_{e}	Electron mobility
μ_{h}	Hole mobility
$\rho(\mathrm{x})$	Charge density
$\sigma(h\upsilon)$	Photoionization cross section for the emission line
$\sigma_{\mathrm{e,h}}$	Capture cross section for electrons or holes
$\tau_{\mathrm{e,h}}$	Lifetime of electrons and holes
Φ	Electrical potential
Φ_{b}	Contact barrier
χ_{e}	Electron affinity
Ψ	Electric potential
ω	Frequency
ω_0	Inflection point of frequency

Chapter 1

Introduction

1.1. Background

The discovery of thin-film solar cells in the 1970s provided a viable alternative to silicon solar cells. Recent advancements in cell performance of copper indium gallium diselenide (CIGS) solar cells has allowed rapid transfer of this technology into industrial-standard modules with high output. Breakthroughs in recent years include the 22.3% world record efficiency on a 0.5 cm^2 cell from Japan's Solar Frontier [1] and a 21.7% cell efficiency of cadmium-buffered CIGS cells by the Zentrum für Sonnenenergie und Wasserstoff-Forschung Baden-Württemberg (ZSW) [2]. These records make CIGS technology highly competitive next to silicon solar cells. The main advantages of thin-film CIGS solar cells come from their thinness of 2 μm [3, 4] which translates into materials cost savings, and the possibility to be grown on flexible substrates for a wide range of applications [5, 6].

CIGS solar modules deployed in outdoor stability studies for 20 years generally showed little degradation when well-encapsulated [7]. Detailed studies of these modules have pinpointed the main cause of degradation to the window layer. Conventional modules are fabricated with cadmium sulfide (CdS) as its buffer layer, typically deposited by Chemical Bath Deposition (CBD). Due to its carcinogenic properties, the European Union has recently imposed a ban on its inclusion in manufacturing processes. Alternative, cadmium-free buffer layers like zinc oxysulfide (Zn(O,S)) and indium sulfide (In_2S_3) exist and can achieve similar efficiencies as their CdS buffered counterparts [8-10]; however, pre-conditioning Zn(O,S) buffered CIGS solar cells with hot-light soaking is necessary to enable devices to reach their maximum efficiencies [11-14]. External factors like moisture and heat lead to a characteristic 'kink' in its current-voltage (I-V) curve over the span of hours or days [15-17] which are not seen in CdS-buffered devices.

So far, pioneering studies on alternative buffer layers are focused on improving their efficiencies to reach or surpass the benchmark of the standard CdS system. Although some preliminary studies showed strong [18-21] or weak [22] light soaking effects for different materials' systems, the mechanisms for these metastable states have not been thoroughly understood. While these studies have been developed primarily to understand the mechanism of metastable Cu(In,Ga)Se_2 absorber-CdS buffer systems [23-30], significantly less have been studied with modifications to the absorber, e.g. Cu(In,Ga)(S,Se)$_2$ (CIGSSe) [31, 32] and the alternative buffer layers, e.g. In_2S_3 [33, 34] or Zn(O,S) [35, 36] introduced into the CIGSSe device architecture. So far, changes to the buffer material leading to fill factor losses of devices that come with a rollover in the I-V curve have not been satisfactorily explained.

1.2. Motivation

Since the mechanism for metastability, i.e. temporary cell efficiency loss which is recoverable by light soaking, in CIGSSe solar cells with zinc-based buffer layers is less well understood, this PhD work aims to explain plausible mechanism based on materials and electrical characterizations, supported by simulation studies. With an understanding in hand, this work also attempts to find solutions to reduce or even completely eliminate the transient loss of efficiencies, i.e. cell relaxation, in Zn-based devices.

1.3. Research Objectives and Scope

The objective of this thesis is as follows: to investigate the metastabilities in Zn(O,S)-buffered Cu(In,Ga)(S,Se)$_2$ thin film solar cells, with coverage of the following aspects:

- **Investigation and comparison of thermally induced metastabilities in CdS and Zn(O,S) buffered CIGSSe devices**

  Thermal Storage (Ageing) and Light Soaking Tests for CdS and Zn(O,S) buffered CIGSSe devices to induce and evaluate the metastable phenomenon. Quantification of changes in traps and defects will be performed by capacitance-voltage (C-V) experiments. This is complemented by a basic understanding of the chemical distribution of full devices having cadmium and cadmium-free buffers with time-of-flight secondary ions mass spectrometry (TOF-SIMS).

- **Understanding the mechanism of metastability for Zn(O,S) buffered CIGSSe devices**

  The composition of Zn(O,S) and its contribution to metastability, as well as chemical changes linked to light soaking effects and long term ageing will be investigated by depth-profiling of X-ray photoelectron spectroscopy (XPS) measurements, inverse photoelectron spectroscopy (IPES) and complemented by scanning electron microscopy with energy dispersive X-ray spectroscopy (SEM/EDX). The mechanism will be proposed, which will be verified by SCAPS-1D simulations and validated by time-resolved photoluminescence (TRPL) experiments on devices with varying Zn(O,S) buffer compositions prepared by atomic layer deposition (ALD).

- **Mitigation of metastabilities in Zn(O,S) buffered CIGSSe devices**

  In order to mitigate the reduction of efficiencies for zinc-based devices, the absorber and zinc-buffer will be studied on the basis of the conduction band offset (CBO) matching. Admittance spectroscopy (AS) and temperature-dependent current-voltage (I-V-T) measurements will be performed to understand the inherent electrical properties of each absorber batch and the recombination sites in different CIGSSe cells. The buffer/absorber compositions at the interface will be considered to find an ideal combination for sulfur-to-oxygen ratio in the buffer and the stoichiometry at the absorber surface.

1.4. Organization of the report

Chapter 2 describes the working principles of CIGS solar cells from the basis of the *p-n* junction. Chapter 3 describes the experimental methods for fabrication of CIGSSe/Zn(O,S) devices. Also, the physical, optical, and electronic methods to characterize the CIGS solar cells and SCAPS-1D, a simulation software used for the modelling in this PhD, are described. Chapter 4 reports a first evaluation of the device stability based on CdS or Zn(O,S) buffer layers. A subsequent evaluation of CIGSSe/CBD-Zn(O,S) devices of different Zn(O,S) compositions is performed. The acceleration of metastability of CIGSSe/CBD-Zn(O,S) devices after thermal ageing is reported. Chapter 5 details the proposed origin of metastability based on simulated scenarios and experimental verification with Time-Resolved Photoluminescence experiments. Chapter 6 evaluates the different growth techniques of the Zn(O,S) buffer in terms of composition and correlate this factor to metastability, in particular focusing on control of stoichiometry by ALD and how the matching of absorber and buffer effectively mitigates metastability. Chapter 7 discusses the conclusions drawn from the current work and future work in this area.

References

[1] http://www.solar-frontier.com/eng/news/2015/C051171.html, **2015**.

[2] M. A. Green, K. Emery, Y. Hishikawa, W. Warta, E. D. Dunlop, *Prog. Photovoltaics Res. Appl.* **2016**, *24*, 3–11.

[3] K. L. Chopra, P. D. Paulson, V. Dutta, *Prog. Photovoltaics Res. Appl.* **2004**, *12*, 69–92.

[4] S. Niki, M. Contreras, I. Repins, M. Powalla, K. Kushiya, S. Ishizuka, K. Matsubara, *Prog. Photovoltaics Res. Appl.* **2010**, *18*, 453–466.

[5] A. Chirilă, P. Bloesch, S. Seyrling, A. Uhl, S. Buecheler, F. Pianezzi, C. Fella, J. Perrenoud, L. Kranz, R. Verma, D. Guettler, S. Nishiwaki, Y. E. Romanyuk, G. Bilger, D. Brémaud, A. N. Tiwari, *Prog. Photovoltaics Res. Appl.* **2011**, *19*, 560–564.

[6] M. Powalla, W. Witte, P. Jackson, S. Paetel, E. Lotter, R. Wuerz, F. Kessler, C. Tschamber, W. Hempel, D. Hariskos, R. Menner, A. Bauer, S. Spiering, E. Ahlswede, T. M. Friedlmeier, D. Blazquez-Sanchez, I. Klugius, W. Wischmann, *IEEE J. Photovoltaics* **2014**, *4*, 440–446.

[7] J. A. del Cueto, S. Rummel, B. Kroposki, C. Osterwald, A. Anderberg, in *Photovoltaic Specialists Conference, 2008. PVSC '08. 33rd IEEE*, **2008**, pp. 1–6.

[8] A. Shimizu, S. Chaisitsak, T. Sugiyama, A. Yamada, M. Konagai, *Thin Solid Films* **2000**, *361–362*, 193–197.

[9] A. Ennaoui, W. Eisele, M. Lux-Steiner, T. P. Niesen, F. Karg, *Thin Solid Films* **2003**, *431–432*, 335–339.

[10] D. Hariskos, R. Menner, P. Jackson, S. Paetel, W. Witte, W. Wischmann, M. Powalla, L. Bürkert, T. Kolb, M. Oertel, B. Dimmler, B. Fuchs, *Prog. Photovoltaics Res. Appl.* **2012**, *20*, 534–542.

[11] K. Kushiya, M. Tachiyuki, T. Kase, Y. Nagoya, T. Miura, D. Okumura, M. Satoh, I. Sugiyama, O. Yamase, in *Photovoltaic Specialists Conference, 1997, Conference Record of the Twenty-Sixth IEEE*, **1997**, pp. 327-330.

[12] T. Nakada, M. Mizutani, *Jpn. J. Appl. Phys.* **2002**, *41*, L165.

[13] T. Nakada, M. Hongo, E. Hayashi, *Thin Solid Films* **2003**, *431–432*, 242–248.

[14] T. N. M. A Contreras, M. Hongo, A. O. Pudov, and J. R. Sites, *Proc. 3rd World Conf. Photovoltaic Energy Convers.* **2003**, 570–573.

[15] J. Serhan, Z. Djebbour, A. Darga, D. Mencaraglia, N. Naghavi, G. Renou, D. Lincot, J. F. Guillemeoles, *Sol. Energy Mater. Sol. Cells* **2010**, *94*, 1884–1888.

[16] J. Serhan, Z. Djebbour, W. Favre, A. Migan-Dubois, A. Darga, D. Mencaraglia, N. Naghavi, G. Renou, J. F. Guillemoles, D. Lincot, *Thin Solid Films* **2011**, *519*, 7606–7610.

[17] K. Kushiya, M. Tachiyuki, Y. Nagoya, A. Fujimaki, B. Sang, D. Okumura, M. Satoh, O. Yamase, *Sol. Energy Mater. Sol. Cells* **2001**, *67*, 11–20.

[18] F. J. Haug, D. Rudmann, H. Zogg, A. N. Tiwari, *Thin Solid Films* **2003**, *431–432*, 431–435.

[19] M. R. Balboul, A. Jasenek, O. Chernykh, U. Rau, H. W. Schock, *Thin Solid Films* **2001**, *387*, 74–76.

[20] A. E. Delahoy, A. Ruppert, M. Contreras, *Thin Solid Films* **2000**, *361–362*, 140–144.

[21] J. Pettersson, C. Platzer-Björkman, M. Edoff, *Prog. Photovoltaics Res. Appl.* **2009**, *17*, 460–469.

[22] J. C. A. E. Delahoy, L. Chen, and Z. J. Kiss, **2002**.

[23] F. Engelhardt, M. Schmidt, T. Meyer, O. Seifert, J. Parisi, U. Rau, *Phys. Lett. A* **1998**, *245*, 489–493.

[24] V. Nadenau, U. Rau, A. Jasenek, H. W. Schock, *J. Appl. Phys.* **2000**, *87*, 584–593.

[25] M. Igalson, M. Edoff, *Thin Solid Films* **2005**, *480–481*, 322–326.

[26] M. Igalson, M. Bodegård, L. Stolt, A. Jasenek, *Thin Solid Films* **2003**, *431–432*, 153–157.

[27] M. Igalson, A. Urbaniak, M. Edoff, *Thin Solid Films* **2009**, *517*, 2153–2157.

[28] T. Eisenbarth, T. Unold, R. Caballero, C. A. Kaufmann, H.-W. Schock, *J. Appl. Phys.* **2010**, *107*, 034509.

[29] K. Decock, S. Khelifi, S. Buecheler, F. Pianezzi, A. N. Tiwari, M. Burgelman, *J. Appl. Phys.* **2011**, *110*, 063722.

[30] A. Urbaniak, M. Igalson, A. Krysztopa, A. Chirilă, S. Buecheler, F. Pianezzi, A. N. Tiwari, *Thin Solid Films* **2013**, *535*, 314–317.

[31] I. L. Repins, B. J. Stanbery, D. L. Young, S. S. Li, W. K. Metzger, C. L. Perkins, W. N. Shafarman, M. E. Beck, L. Chen, V. K. Kapur, D. Tarrant, M. D. Gonzalez, D. G. Jensen, T. J. Anderson, X. Wang, L. L. Kerr, B. Keyes, S. Asher, A. Delahoy, B. Von Roedern, *Prog. Photovoltaics Res. Appl.* **2006**, *14*, 25–43.

[32] A. Darga, D. Mencaraglia, Z. Djebbour, A. Migan Dubois, V. Bermúdez, J. P. Connolly, C. M. Ruiz, J. F. Guillemolles, *Thin Solid Films* **2008**, *516*, 6999-7003.

[33] J. Marlein, K. Decock, M. Burgelman, *Thin Solid Films* **2009**, *517*, 2353–2356.

[34] A. Darga, D. Mencaraglia, Z. Djebbour, A. M. Dubois, R. Chouffot, J. Serhan, F. Couzinié-Devy, N. Barreau, J. Kessler, *Thin Solid Films* **2009**, *517*, 2423–2426.

[35] W. Witte, D. Hariskos, M. Powalla, *Thin Solid Films* **2011**, *519*, 7549–7552.

[36] W. Witte, D. Hariskos, A. Eicke, R. Menner, O. Kiowski, M. Powalla, *Thin Solid Films* **2013**, *535*, 180–183.

Chapter 2

Literature Review

The p-n junction provides the fundamental basis to define the working principles of solar cells. First, the p-n junction solar cell is discussed, followed by charge separation. From that, the equations for the current-voltage curve of a CIGS solar cell are obtained. Next, recombination effects limiting the output of the solar cell is discussed in greater detail. Finally, the chapter is concluded with the discussion of metastability, a transient state of high efficiency that relaxes into a state of low efficiency over time, in devices buffered with CdS and alternative buffers.

2.1. The *p-n* junction

First developed by Shockley [1, 2] and subsequently expanded and refined by others [2-4], the principles of a *p-n* junction applies not only for solar cells, but in many other electronic applications and semiconductor devices. The *p-n* junction that exists in a solar cell is discussed below.

2.1.1. Homojunctions

The prerequisite for a working solar cell is its ability to separate charges. The *p-n* junction serves this purpose with two terminals placed next to each other to achieve this effect. When there are no applied voltage and current flow, the solar cell is under thermodynamic equilibrium. At this point, the electrochemical potential on the *p*- and *n*-sides remain constant. A direct consequence of spatial separation of charged particles, the difference in electric potential between the two layers leads to a diffusion of electrons from *n*- to *p*-side and the opposite direction for holes. This is counterbalanced by a drift current of electrons and holes going in opposite directions. Depleted of moving charge carriers, a space charge region (SCR) forms between the two layers. This creates a potential drop (the built-in potential V_{bi}) with the equation [5]

$$eV_{bi} = e(\varphi(-\infty) - (\varphi(-\infty)) = E_g - \bar{E}_{F_p} - \bar{E}_{F_n} \tag{2.1}$$

where φ is the electrical potential, $\bar{E}_{\mathrm{Fp}}$ is the difference in energy between Fermi level and valence band maximum (VBM) of the neutral region in the *p*-side, and ĒFn is the difference in energy between Fermi level and conduction band minimum (CBM) of the neutral region in the *n*-side.

Defining the CBM as E_{C}, VBM as E_{V}, and Fermi level as E_{F}, the charge carrier densities are then $n = N_C \exp\left(-\frac{\bar{E}_{Fn}}{kT}\right)$ and $p = N_V \exp\left(-\frac{\bar{E}_{Fp}}{kT}\right)$, respectively. The following equation [5] is obtained from the Boltzmann approximation, since $np = N_C N_V \exp\left(-\frac{E_g}{kT}\right) = n_i^2$,

$$eV_{bi} = kT \ln\left(\frac{N_d N_a}{n_i^2}\right) \tag{2.2}$$

with the assumption that all the doping atoms are ionized, i.e. $p = N_a$ and $n = N_d$, where N_a and N_d stand for the doping density of the *p*-type or *n*-type semiconductors, respectively, n_i is the intrinsic charge carrier density of the material, and e is the elemental charge. Integrating the Poisson equation leads to the spatial dependence of the electrical potential $\varphi(\vec{x})$

$$-\Delta\varphi(\vec{x}) = \frac{\rho(\vec{x})}{\varepsilon\varepsilon_0} \tag{2.3}$$

where ε_0 denotes the electric constant, ε the relative permittivity of the semiconductor material, and $p(\vec{x})$ the local charge density. Assuming a constant translational symmetry in the *p*-*n* junction, this problem can be rendered as one-dimensional (1D).

The Schottky approximation for semiconductors assumes that when the impurity concentration in a semiconductor changes abruptly from N_a to N_d, one obtains an abrupt, one-sided p^+-n junction. This is true in the *p*-type CIGS absorber where $N_a >> N_d$. Consequently, the charge density at the edge of the SCR and the interface between the *p*- and *n*-side are expected to change abruptly. The charge density is illustrated in Figure 2.1 (a). From that, the built-in potential V_{bi} may be derived in (b), and the electric potential $\varphi(\vec{x})$ in (c), resulting in the electronic band diagram of the homojunction in (d).

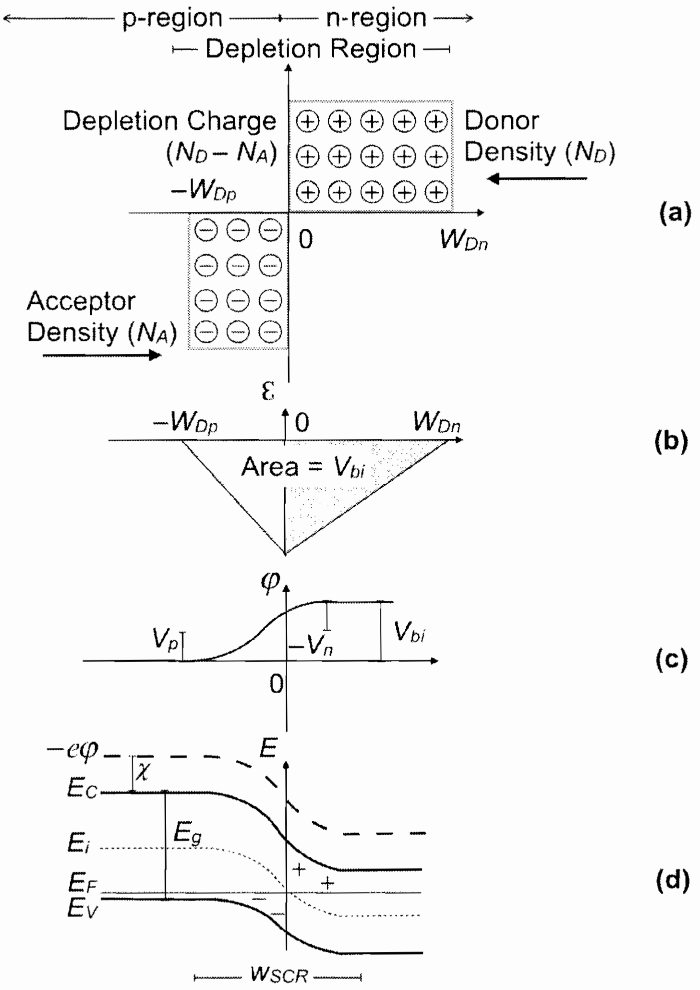

Figure 2.1 (a) *p-n* junction, thermal equilibrium, with space-charge distribution. (b) Distribution of electric field. (c) Electric potential distribution, with built-in potential of V_{bi}. (d) Electronic Band Diagram. Image adapted from Sze [5].

When charge neutrality is assumed, the following ratio can be obtained for the respective widths of the SCR occupied by the *p*-side and *n*-side,

$$x_p = \frac{N_d}{N_a} x_n \tag{2.4}$$

with x_p being the width of the SCR on the *p*-side, and x_n on the n-side. Since the *n*-side is more heavily doped, $N_d >> N_a$ for the *p-n* junction in the entire CIGS solar cell. As a result, the SCR width on the p-side is substantially larger than on the n-side, and the total width w_{SCR} is given by

$$w_{SCR} = x_p + x_n = \left(1 + \frac{N_d}{N_a}\right) x_n \tag{2.5}$$

When one integrates the Poisson equation on the n-side of the junction, assuming that boundary conditions $E(-x_n) = 0$ and $\varphi(-x_n) = \varphi(-\infty)$:

$$\varphi_n(x) = \frac{eN_d}{2\varepsilon\varepsilon_0}(x + x_n)^2 + \varphi(-\infty) \tag{2.6}$$

For the p-side, assuming that boundary conditions $E(x_p) = 0$ and $\varphi(x_p) = \varphi(\infty)$:

$$\varphi_p(x) = \frac{eN_a}{2\varepsilon\varepsilon_0}(x - x_p)^2 + \varphi(\infty) \tag{2.7}$$

When $\varphi_n(0) = \varphi_p(0)$, the equation for V_{bi} is derived as

$$V_{bi} = \varphi(-\infty) + \varphi(\infty) = \frac{e}{2\varepsilon\varepsilon_0}(N_d x_n^2 + N_a x_p^2) \tag{2.8}$$

With Equations 2.4 and 2.5, it is obtained

$$x_n = \left(\frac{2\varepsilon\varepsilon_0}{e} \frac{N_a}{N_d(N_a + N_d)} V_{bi}\right)^{\frac{1}{2}} \tag{2.9}$$

$$x_p = \left(\frac{2\varepsilon\varepsilon_0}{e} \frac{N_d}{N_a(N_a + N_d)} V_{bi}\right)^{\frac{1}{2}} \tag{2.10}$$

$$w_{SCR} = \left(\frac{2\varepsilon\varepsilon_0}{e} \frac{N_a + N_d}{N_a N_d} V_{bi}\right)^{\frac{1}{2}} \tag{2.11}$$

For the one-sided abrupt p^+-n junction, V_{bi} is calculated by inserting Equations 2.4 and 2.8 into 2.7 to arrive at:

$$\varphi(x = 0) = \frac{eN_a}{2\varepsilon\varepsilon_0} x_p^2 = V_{bi} \frac{N_d}{N_a + N_d} \tag{2.12}$$

2.1.2. CIGSSe/Buffer/*i*-ZnO Heterojunction

For CIGSSe devices with a heterojunction configuration, the *p-n* junction does not form continuous valence and conduction bands along interfaces of different materials. This is a result of dissimilar materials with different band gaps E_g, different electron affinities χ and alignment of the E_F. Consequently, band offsets form in the interface between the CIGSSe/buffer and buffer/window interfaces, which starkly contrasts with the homojunction model discussed in the previous section. The different work functions of adjacent layers redistribute charges of electrons in the valence band, resulting in an atomically thin dipole layer that changes the electrostatic potential at this point. This dipole moment, as well as charged interfaces states, are neglected when one assumes the Anderson model [6], hence one only considers the discontinuities of these heterogeneous materials that are adjacent to each other. In reality, discontinuations in the valence and conduction bands are influenced by defects at the interfaces, since with these heterogeneous materials one might expect a high defect density to be located at the interfaces.

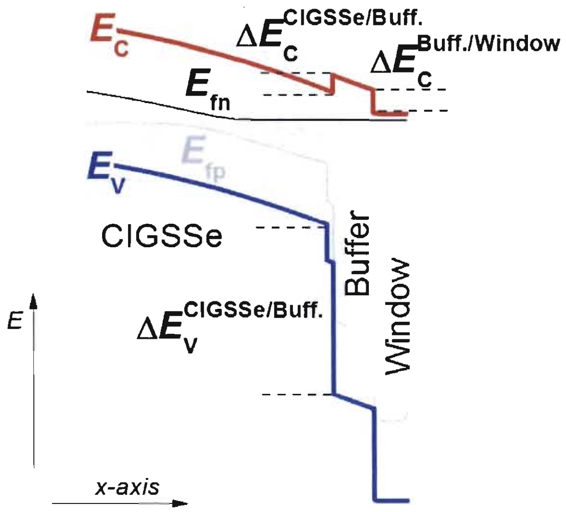

Figure 2.2 Electronic Band Diagram of CIGSSe/Buffer/*i*-ZnO Heterojunction. A spike occurs at $+\Delta E_C$ (CIGSSe/Buffer) and cliffs at $-\Delta E_V$ (CIGSSe/Buffer) and $-\Delta E_C$ (Buffer/*i*-ZnO).

It has been experimentally proven by X-ray Photoemission Spectroscopy (XPS) studies on the valence band edge of devices that there are band discontinuities between the

CIGSSe/Buffer and Buffer/Window [7-9]. For a standard $CuInSe_2$ (E_g^{CIS}= 1.05 eV) and CdS buffer (E_g^{CdS} = 2.4 eV), one might calculate a Valence Band Offset (VBO) of $\Delta E_V^{CIS/CdS}$ = 0.8±(0.2) eV for $CuInSe_2$ and a Conduction Band Offset (CBO) of $\Delta E_C^{CIS/CdS} = E_g^{CdS} - E_g^{CIS} - \Delta E_V^{CIS/CdS} \approx$ 0.55 eV [10]. This is validated by theoretical calculations for CIS with the values $\Delta E_V^{CIS/CdS} = -1.03$ eV and $\Delta E_C^{CIS/CdS} = 0.3$ eV [7]. When one introduces gallium into the CIS, $E_g^{CuIn_{1-x}Ga_xSe_2}$ is then determined by the following [8, 11]

$$E_g^{CuIn_{1-x}Ga_xSe_2} = E_g^{CuInSe_2}(1-x) + E_g^{CuGaSe_2}x - bx(1-x) \tag{2.13}$$

with b denoting a bowing coefficient of 0.20 eV, describing the deviation of E_g^{CIS} from linear behavior. Pure $CuInSe_2$ has a band gap of 1.01 eV and pure $CuGaSe_2$ of 1.68 eV. The CBM at the CIS layer is increased the higher the quantity of gallium in the CIS. The initial spike from a positive ΔE_C ($CuInSe_2$/CdS) will eventually become a cliff from a negative ΔE_C ($CuGaSe_2$/CdS) due to widening $E_g^{CuIn_{1-x}Ga_xSe_2}$.

Additionally, the replacement of selenium with sulfur also widens E_g^{CIS}, mainly by lowering the VBM and increasing the CBM [8]. The band gap of the $CuIn(Se_{1-y}S_y)_2$ system could be tuned from 1.02 to 1.52 eV [12]. It was found that [S]/[Se] depended on the chalcogen strongly for Cu-poor films, whereas sulfur incorporation was preferential for Cu-rich systems [13].

Since the absorbers in this study are fabricated with a $Cu(In_{1-x}Ga_x)(Se_{1-y}S_y)_2$ stoichiometry, one has carefully consider the effects of both sulfur and gallium on defect formation and their role in changing the band alignment between the absorber/buffer interface [14]. By changing these two important parameters, i.e. the [In]:[Ga] ratio and the [Se]:[S] ratio, it is possible to tune $E_g^{CuIn_{1-x}Ga_x(Se_{1-y}S_y)_2}$ to achieve a good match with the buffer and window layers in order to improve the charge collection.

2.2. Charge Collection in Cu(In,Ga)(S,Se)₂ Devices

A working solar cell converts energy from incident photons into electrical energy. Irradiating photons with wavelengths ≥ E_g of the material leads to absorption within the solar cell, which in turn generates electron-hole pairs within the layers. These separated charges have the possibility to either 1) recombine or 2) separate. Charge separation generates an external current or voltage which is measured.

The *p-n* junction of a CIGS solar cell provides a voltage drop across the SCR. During charge separation, electrons move towards the *n*-doped side across the buffer and window layers to be collected at the front contact. Holes move in the opposite direction towards the back contact. Under low injection conditions, whereby CIGS doping density vastly exceeds the density of generated charge carriers, minority carriers limit the current collected. This is in turn limited by recombination processes occurring in the bulk of the absorber, the SCR, or at the heterointerfaces. Electron and hole current densities $\vec{j}_e$ and $\vec{j}_h$ are expressed as a sum of the diffusion and drift terms:

$$\vec{j}_e = \vec{j}_{diffusion,e} + \vec{j}_{drift,e} = -eD_e \nabla n + \sigma_e \vec{E} \tag{2.14}$$

$$\vec{j}_h = \vec{j}_{diffusion,h} + \vec{j}_{drift,h} = -eD_h \nabla p + \sigma_h \vec{E} \tag{2.15}$$

The continuity equation $\frac{\partial \rho}{\partial t} + \nabla \vec{j} = 0$ forms the basic equation for charge carrier transport. This can be expressed for electron and hole concentrations $n(\vec{x})$ and $p(\vec{x})$ with equation 2.16.

$$\begin{gathered} D_h \Delta p(\vec{x}) - \mu_h \vec{E}(\vec{x}) \nabla p(\vec{x}) - \mu_h p(\vec{x}) \nabla \vec{E}(\vec{x}) - R(\vec{x}) + g(\vec{x}) = 0 \\ D_e \Delta n(\vec{x}) - \mu_e \vec{E}(\vec{x}) \nabla n(\vec{x}) - \mu_e n(\vec{x}) \nabla \vec{E}(\vec{x}) - R(\vec{x}) + g(\vec{x}) = 0 \end{gathered} \tag{2.16}$$

where $\mu_{e,h}$ denotes the electron/hole mobility, $R(\vec{x})$ the recombination rate, and $g(\vec{x})$ the generation rate for charge carriers.

The quasi-neutral region (QNR) of a *p*-type material is considered under low injection, where $\vec{E} = 0$. The density of excess electrons $\delta n(\vec{x})$ from the generation at position $\tilde{\vec{x}}$ obeys the following differential equation derived from the continuity equation [15]:

$$D_e \Delta \delta n(\vec{x}) - \frac{\delta n(\vec{x})}{\tau} = a^* \delta(\vec{x} - \tilde{\vec{x}}) \tag{2.17}$$

Σ_p denotes the edge of the space charge region, Σ_{BC} denotes the plane of the back contact, τ is the electron lifetime, and a^* is 1 s^{-1}. $R(\vec{x}) = \frac{\delta n(\vec{x})}{\tau}$ is also assumed. The appropriate boundary conditions are defined as

$\delta n(\vec{x}) = 0$ if $\vec{x} = \sum_p$

$D_e \nabla \delta n(\vec{x}) \hat{e}_{BC} = S_{BC} \delta n(\vec{x})$ if $\vec{x} \in \sum_{BC}$

with S_{BC} corresponding to the back contact recombination velocity and $\hat{e}_{BC}$ a normal vector to Σ_{BC}. Perfect collection is assumed at the edge of the SCR ($\delta n = 0$). If τ is assumed to be independent of δn, equation 2.18 becomes a linear differential equation. Thereafter, the particle current (in s^{-1}) across the edge of the SCR Σ_p may be expressed as:

$$I(\tilde{\vec{x}}) = \int_{\sum_p} D_e \nabla \delta n \hat{e}_p d\sigma \tag{2.18}$$

where $\hat{e}_p$ is a normal vector to Σ_p. The inhomogeneous differential equation 2.18 $\delta n(\vec{x})$ may be substituted with a homogeneous differential equation for the collection function $f_c(\vec{x})$ according to the reciprocity theorem derived by Donolato [15, 16].

$$D_e \Delta f_c(\vec{x}) - \frac{f_c(x)}{\tau} = 0 \tag{2.19}$$

With the following boundary conditions:

$f_c(\vec{x}) = 1$ if $\vec{x} = \sum_p$

$-D_e \nabla f_c(\vec{x}) \hat{e}_{BC} = S_{BC} f_c(\vec{x})$ if $\vec{x} \in \sum_{BC}$

It is obtained:

$$a^* f_c(\tilde{\vec{x}}) = \int_{\sum_p} D_e \nabla \delta n \hat{e}_p d\sigma = I(\tilde{\vec{x}}) \tag{2.20}$$

The collection function $f_c(\vec{x})$ corresponds to the normalized current response for point-like generation in the QNR, which is equivalent to the probability of collection of an electron generated at $\tilde{\vec{x}}$. At the edge of the SCR, a value of 1 is assumed for the probability of collection.

Moving towards a more general case where the generation profile is extended, the generation volume *V*, described by the superposition of δ-functions, is integrated to obtain the collected current (in amperes)

$$I = e\int_V g(\vec{x})f_c(\vec{x})d\vec{x} \tag{2.21}$$

Hereafter, the electron current across the edge of the SCR Σ_p may be expressed by elaborating $f_c(\vec{x})$ and $g(\vec{x})$. Simplifying equation 2.21 with the consideration of translation invariance parallel to the *p*-*n* junction:

$$I = e\int f_c(x)g(x)dx \tag{2.22}$$

where x is the spatial coordinate perpendicular to the *p*-*n* junction, $f_c(x)$ is the 1D expression of the collection function, and $g(x) = \iint g(\vec{x})dydz$ the 1D expression for the generation profile. If an infinite semiconductor without back contact is assumed, the following 1D solution for $f_c(x)$ is obtained

$$\varphi(x) = \exp\left(-\frac{x}{L_e}\right) \tag{2.23}$$

where $L_e = \sqrt{D_e\tau}$ is the electron diffusion length. Considering a semiconductor that has recombination velocity S_{BC} at the back contact at position $x = x_{BC}$, $f_c(x)$ may be expressed as:

$$f_c(x) = \frac{\frac{1}{L_e}\cosh\left(\frac{x - x_{BC}}{L_e}\right) - \frac{S_{BC}}{D_e}\sinh\left(\frac{x - x_{BC}}{L_e}\right)}{\frac{S_{BC}}{D_e}\sinh\left(\frac{x_{BC} - x_p}{L_e}\right) + \frac{1}{L_e}\cosh\left(\frac{x_{BC} - x_p}{L_e}\right)} \tag{2.24}$$

with x_p representing the position of the SCR edge.

2.3. I-V Curve and Parameters

The dark I-V curve, resembling that of an ideal diode, is expressed from Shockley's derivation of the continuity equation as [1, 5]

$$J_{dark}(V) = J_0\left[\exp\frac{eV}{kT} - 1\right] \text{with } J_0 = e\left(p_{n_0}\frac{D_h}{L_h} + n_{p_0}\frac{D_e}{L_e}\right) \tag{2.25}$$

Where J_0 is the saturation current density, V is the applied voltage, n_{p0} the p-side equilibrium electron density, p_{n0} the n-side equilibrium hole density, and L_h the hole diffusion length. This simplification is treated based on the following assumptions: considering the Boltzmann approximation for charge carrier densities, low injection, abrupt depletion layers, and no recombination and generation currents (drift or diffusion) within the depletion layer [5].

For a real diode, the following expression holds:

$$J_{dark}(V) = J_0\left[\exp\frac{eV}{n_{id}kT} - 1\right] \text{with } J_0 = J_{00}\exp\left(-\frac{E_a}{n_{id}kT}\right) \tag{2.26}$$

where n_{id} denotes the diode quality factor, E_a is the activation energy of the current density, J_{00} is the reference current density. n_{id} and E_a are dependent on the dominant recombination processes in the solar cell as well as temperature. J_{00} is, on the other hand, only slightly dependent on the temperature.

Under illumination, the solar cell generates a photocurrent $J_{ph}(V)$ and the I-V curve is illustrated as

$$J_{illum}(V) = J_0\left[\exp\frac{eV}{n_{id}kT} - 1\right] - J_{ph}(V) \tag{2.27}$$

The superposition principle may be applied if the diode current is the only one flowing under illumination. Under this assumption, the diode current under illumination is obtained by subtracting $J_{ph}(V)$ from $J_{illum}(V)$. The short circuit current (J_{SC}) may be derived from

$$J_{SC}(V) = J_{illum}(V) - J_{dark}(V) \tag{2.28}$$

Subtracting the dark current from $J_{illum}(V)$ leads to the J_{SC}.

A standard I-V measurement for CIGS solar cells is illustrated in Figure 2.3. Standard parameters from which the cell efficiency may be calculated from are the open circuit voltage (V_{OC}), short circuit current density (J_{SC}), and the fill factor (FF), which may be expressed as a product of the following

$$FF = \frac{V_{mpp}J_{mpp}}{V_{OC}J_{SC}} \tag{2.29}$$

where *mpp* is the maximum power point of the solar cell output and V_{mpp} and J_{mpp} are voltage and current density values at the maximum power point, respectively. The conversion efficiency for a solar cell is thus expressed as

$$\eta = \frac{V_{OC}J_{SC}FF}{\phi} \tag{2.30}$$

where ϕ represents the energy from the external source, which under standard solar spectra is defined as AM1.5G conditions (1000 W/m^2) [17].

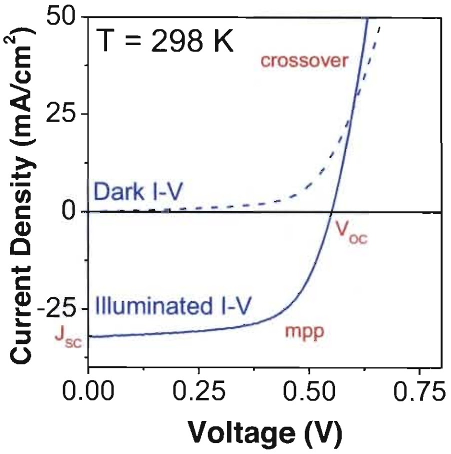

Figure 2.3 I-V curve under dark and illuminated conditions for a CIGSSe solar cell with Zn(O,S) buffer, measured at 298 K. A crossover is observed between the dark and illuminated I-V curves.

One effect often observed in the I-V characteristics in CIGS solar cells is the crossover between the dark and illuminated I-V curves, implying an imperfect charge separation. This effect will be further discussed in Section 2.5., alongside the rollover and kink in the illuminated I-V curve that occurs when there is a problem with charge collection.

2.4. Recombination

In a CIGSSe solar cell, different recombination paths, depicted in Figure 2.4, exist for the diode current. As the *p*-*n* junction exists at the CIGSSe/buffer interface, the most critical pathways impeding charge transport are (1) interface recombination (IF), a feature of heterojunctions, and (2) space charge region (SCR) recombination, which extends into the more lightly-doped *p*-type $Cu(In,Ga)(S,Se)_2$. Other recombination pathways are possible in this configuration. At the heterojunction interface, defects occur due to lattice mismatch or segregation of impurities, and recombination is inevitable. However, one clear advantage of this structure is that (5) bulk recombination in the buffer and/or window for electrons flowing to the *n*-side of the device is suppressed due to the large band gaps of the buffer and window. Hence, it is possible to neglect the recombination pathway (5) in the diode current calculations. Deeper in the absorber bulk, (3) quasi-neutral region (QNR) recombination, and (4) recombination at the interface with the Mo back contact (BC), are also possible for the majority carriers flowing in this direction.

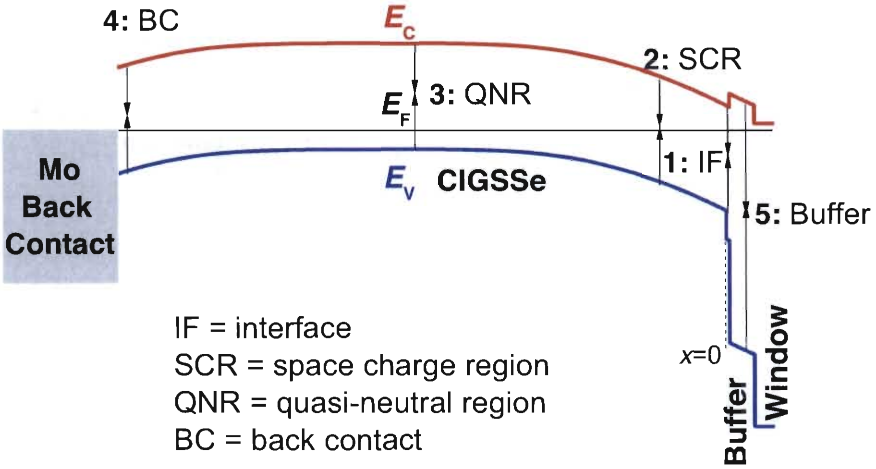

Figure 2.4 Band Diagram of a CIGSSe device at 0 V with (1) Interface Recombination (2) Space Charge Region Recombination (3) Quasi Neutral Region Recombination (4) Back Contact Recombination (5) Buffer Recombination.

2.4.1. Generation and Recombination Processes

Free electron and hole densities obey the equation $np=n_i^2$ at thermal equilibrium. At this state, the carrier generation and recombination rates cancel out and net rate of recombination is zero. However, perturbation of this equilibrium by an external stimulus (e.g. light, electrical bias) leads to a change in generation and/or recombination rate. When excess carriers are generated, it follows that $np>n_i^2$ and results in a net recombination of carriers. On the contrary, when excess carriers are less than zero, $np<n_i^2$ and recombination rate will be suppressed in favor of generation of carriers.

The generation process starts upon irradiation of photons of light with energy $>h\nu$ (the band gap of the material) on the semiconductor. Once absorbed, an electron is promoted from the valence band to the conduction band (Figure 2.5 (a)). The rest of the processes following generation, described in Figure 2.5, are discussed in the following section.

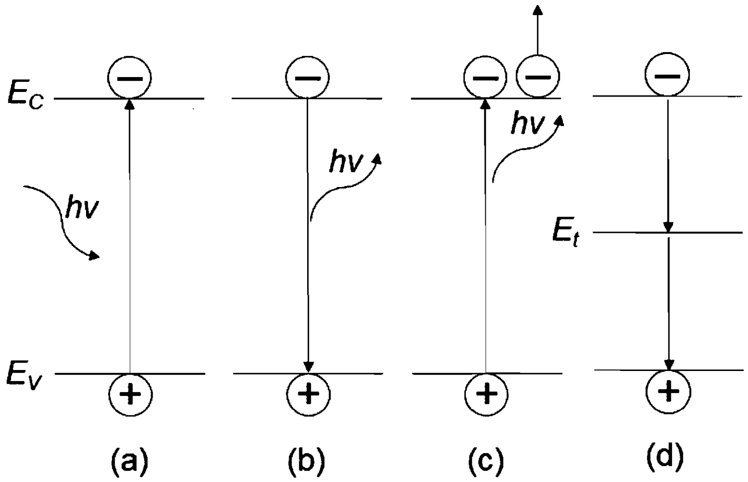

Figure 2.5 (a) Generation of charges upon irradiation of light of $>h\nu$ energy (b) Radiative recombination, with emission of light of $h\nu$ energy (c) Auger recombination (d) Shockley-Read-Hall recombination with defect level at E_t.

(a) Radiative (band-to-band) Recombination

Radiative recombination takes place when an electron transits from the conduction band to the valence band, with the emission of a photon with energy equivalent to the band gap of the material [5]. As it is dependent on the density of electrons promoted to the conduction band and holes to the valence band during generation, the recombination process $R=B(np-n_i^2)$ is proportional to the product of the holes and electrons, and B is the constant of the material property.

(b) Auger Recombination

Auger recombination takes place when an electron and a hole recombine, but the photon energy is not emitted like the case of radiative recombination, but is instead transferred to another electron in the conduction band [5]. This process is important when considering a device under a high injection level, and also when the semiconductor has a high carrier concentration.

(c) Shockley-Read-Hall (SRH) Recombination

When discussing the trap-assisted non-radiative recombination process, termed as Shockley-Read-Hall (SRH) recombination, one has to consider four possibilities involved in the process: the captures of holes and electrons, and the emissions of holes and electrons, with the transition through a trap state E_t typically located near the mid-gap of the material [5].

When the $Cu(In,Ga)(S,Se)_2$/buffer/window heterojunction is illuminated at steady state, hole and electron Fermi levels (E_{fn} and E_{fp} respectively) split up, expressed in the following

$$E_C - E_{fn} = kT\ln\left(\frac{N_C}{n}\right) \tag{2.31}$$

$$E_V - E_{fp} = kT\ln\left(\frac{N_V}{p}\right) \tag{2.32}$$

Electron and hole densities at this state of perturbation are described by the total sum of electrons/holes in equilibrium and electrons/holes additionally generated during perturbation, i.e. $n = n_0 + \delta n$ and $p = p_0 + \delta p$ respectively. Occupation of states at the steady state quasi Fermi levels for electrons and holes is governed by thermal exchange with the relevant band and not by recombination [18].

An example of a defect state acting as a recombination center for electrons (minority carriers) in a p-type semiconductor is illustrated by considering the following definition. If the probability of re-emission of a trapped electron to the valence band is higher than to the conduction band, then it is a recombination center. Otherwise, it is an electron trap. When the probabilities of re-emission to the conduction band and emission to valence band are the same, then the energetic level is designated as demarcation level $\bar{E}_n$. For a defect state defined as a recombination center, it should be energetically located at $E_{fp}<E_t<\bar{E}_n$. $\bar{E}_n$ is further described as [18]

$$E_C - \overline{E}_n = E_{fp} + kT\ln\left(\frac{\sigma_e m_e^*}{\sigma_h m_h^*}\right) \tag{2.33}$$

where $m_{e,h}^*$ are the effective masses of electrons or holes. One might illustrate the effective region where defect states participate as efficient recombination centers in a band diagram such as Figure 2.6. One has to consider the energetic position of defect levels during voltage bias and charge distribution within the device, which influences the band bending of the p-side, in order to determine the impact of these defects in non-radiative recombination.

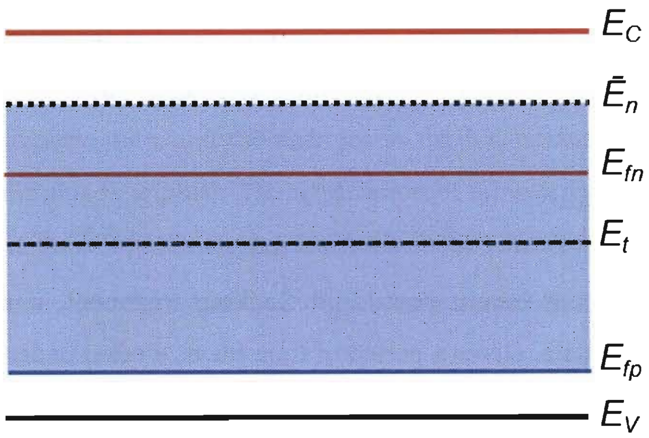

Figure 2.6 Band diagram of a *p*-type semiconductor with demarcation energy $\bar{E}_n$. The shaded region indicates the area where E_t will exist as an effective recombination center. Else, it will exist as a trap where the captured electron is re-emitted to the conduction band.

The SRH statistics describe the net recombination rate [5] as

$$U_{SRH} = N_t \frac{\sigma_n \sigma_p v_{th}(np - n_i^2)}{\sigma_n(n + n^*) + \sigma_p(p + p^*)} \tag{2.34}$$

where v_{th} is the thermal velocity, and σ_n and σ_p denote the capture cross section for electrons and holes, respectively.

$$n^* = N_C \exp\left(-\frac{E_C - E_t}{k_B T}\right) \tag{2.35}$$

$$p^* = N_V \exp\left(-\frac{E_t - E_V}{k_B T}\right) \tag{2.36}$$

Where $n^*p^*=n_i^2$, $N_{C,V}$ are the effective density of states in the $E_{C,V}$, and is temperature-dependent. When lifetimes for electrons and holes are introduced as $\tau_n=(N_t v_{th}\sigma_n)^{-1}$ and $\tau_p=(N_t v_{th}\sigma_p)^{-1}$ respectively, one can rewrite equation (2.34) as the following

$$U_{SRH} = N_t \frac{np - n_i^2}{\tau_p(n + n^*) + \tau_n(p + p^*)} \tag{2.37}$$

As the effectiveness of this recombination process occurs where the energy barrier is located at approximately half of the band gap energy, deep defects are more efficient recombination centers. Shallow defects, on the other hand, occur near E_V or E_C and the transition process in this capture/emission process for holes/electrons requires a larger amount of energy. Hence, these are less favorable compared to transitions to and from deep defects.

2.5. Metastability

At its maximum output post-Light Soaking treatment, a CIGS solar cell attains its "metastable" state. Given a period of time (days, weeks) under dark storage, a reduction of efficiency is observed, and this is termed as the solar cell's "relaxed" state (Figure 2.7). This transient change is different from permanent degradation in that a subsequent light soaking from the relaxed state recovers the high efficiency attained at the point of post-fabrication hot light soaking (HLS). Although studied for many years [19-22], the origin(s) and mechanism(s) of this transient, recoverable loss of cell efficiency are still under debate.

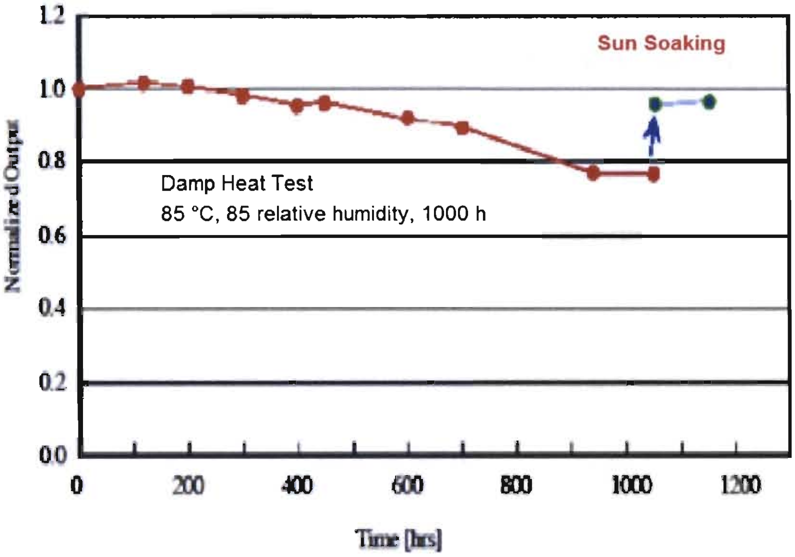

Figure 2.7 Typical result of Damp heat on CIGS-based thin-film PV modules which were stored in the dark for 1000 hours at 85 °C temperature and 85% relative humidity. Reproduced with permission from [23].

2.5.1. External Stimuli

Metastability is typically quantified by determining the I-V curve under illumination during its relaxed, low-efficiency state, and the changes to the I-V parameters after an external electrical or light stimulus is applied. The application of an external stimulus reveals the temporary changes to the I-V parameter(s), from which the cause of metastability might be identified.

(a) Red Light Soaking

Long-wavelength (red) light does not get absorbed by the wide band gap window and buffer (ZnO and CdS/Zn(O,S)) but instead passes through the window and buffer (emitter) to get absorbed in the first few hundred nanometers of the absorber (Figure 2.8). Upon illumination for a few hours [24], the lateral conductivity of the $Cu(In,Ga)Se_2$ film increases, resulting in increased junction capacitance as defects at the absorber close to the interface gets converted to *p*-type, and net acceptor density in the absorber, $N_{A,abs}$ is increased. It is noted that conductivity also increases at this point in time. Switching off the illumination leads to a decline of the heightened conductivity to its initial value after a large time constant [25]. Due to a small quantity of donor-type V_{Cu} defects, the red light effect does not impact the space charge capacitance of Cu-rich $Cu(In,Ga)Se_2$ samples significantly [26]. However, considering Cu-poor CIGS samples have more V_{Cu} defects and a smaller quantity of V_{Se} defects, then its impact on the V_{OC} will be more significant [27].

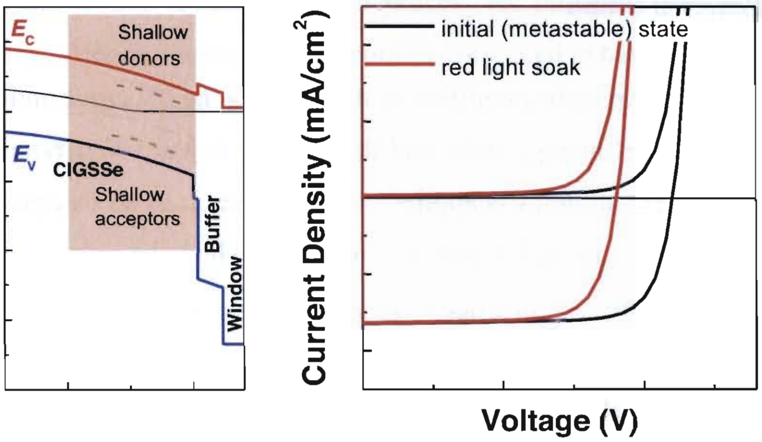

Figure 2.8 Band diagram and corresponding dark and illuminated I-V curve at its initial metastable state and after red light soak.

In the critical regions of the absorber where charge transport occurs, one might consider the impact on the red light on recombination and how it limits V_{OC}. V_{OC} would be severely limited if the majority of the recombination occurred at the SCR. While an increase in $N_{A,abs}$ during Red Light Soaking (RLS) narrows the SCR, reducing the recombination zone and improving the V_{OC}, the converse occurs when RLS is removed, widening the region of recombination and limiting V_{OC}. In the QNR, the same argument would also be valid for any increase/decrease of absorber doping. Concerning IF recombination, one would need to consider whether Fermi-level pinning (FLP) occurs at the absorber/buffer interface. When FLP does not exist at the heterojunction interface, then V_{OC} decreases with increasing $N_{A,abs}$ due to a reduction of potential drop across the *p-n* junction. On the other hand, when FLP occurs at the interface, then IF recombination is independent of doping of $N_{A,abs}$ and V_{OC}. In the case tunneling is a mechanism for the IF recombination, then V_{OC} will drop with increasing $N_{A,abs}$. Early studies of CIGS devices under RLS reported a decrease of V_{OC} with a small change in *FF* [26, 28], and this was linked to a decrease in bulk recombination [29].

(b) Blue Light Soaking

Blue light of $h\nu > E_g^{buffer}$ is predominantly absorbed in the larger band gap buffer and window layers [30]. Consequently, *FF* increases and the red kink in the illuminated I-V curve is passivated alongside a reduction of crossover between dark and illuminated I-V curves (Figure 2.9). The junction capacitance also decreases due to a back conversion of *p*-type acceptors to *n*-type donors at the interface [31]. Eisgruber *et al.* concluded from the $h\nu$ dependency of the E_g^{buffer} that the buffer participates in the mechanism for *FF* gains during Blue Light Soaking (BLS) [32].

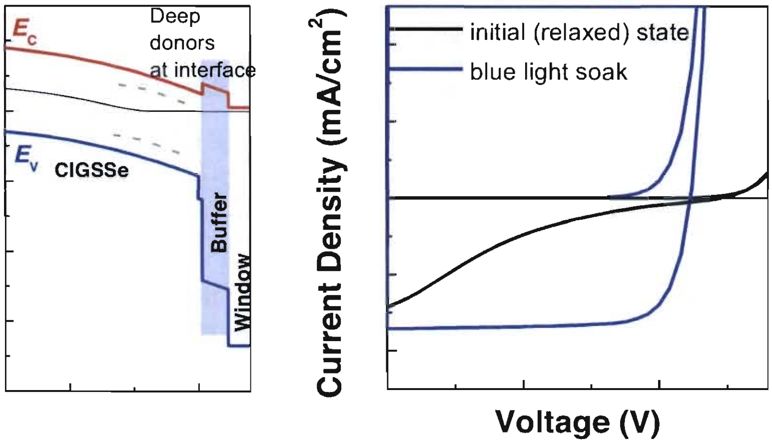

Figure 2.9 Band diagram and corresponding dark and illuminated I-V curve at its initial relaxed state and after blue light soak.

BLS predominantly produces electrons at the interface regions. This was quantified by electron beam induced current (EBIC) experiments performed by Kniese *et al*., who observed a passivation of the EBIC barrier upon irradiation of the heterojunction with electrons [33].

(c) White Light Soaking

White Light Soaking (WLS) with an AM1.5G spectrum is a standard light soaking procedure performed in many labs, as it simulates the working condition of modules deployed in the field. Taking note that white light encompasses both the blue and red spectrum discussed in the previous sections, both the effects of RLS and BLS have to be considered to describe the final metastable state of the device after light soaking. WLS leads to the concurrent increase of both V_{OC} and *FF* of the device, and persistent photoconductivity is observed for the CIGS absorber film (Figure 2.910). It is notable that RLS effect plays a larger role in that there is an overall increase in the device capacitance. For devices with alternative buffer layers, WLS has a more pronounced effect compared to CdS devices, although the exact reason is still under debate [19]. At this metastable state, barriers for photo or diode currents are passivated by white light.

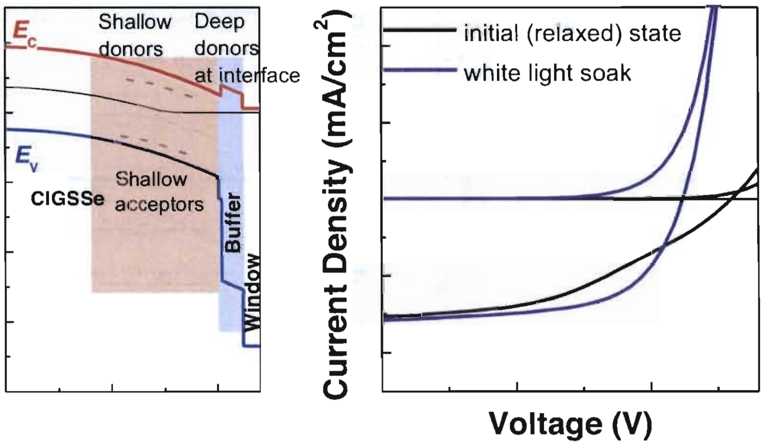

Figure 2.10 Band diagram and corresponding dark and illuminated I-V curve at its initial relaxed state and after white light soak.

(d) Forward Bias

The application of a forward bias to the CIGS solar cell in the dark resembles the effects of RLS in certain aspects. An increase of electrical capacitance, and $N_{A,abs}$ of one order of magnitude, can be quantified from capacitance-voltage (C-V) profiles [34, 35] which results in the improvement of the V_{OC} [28, 36].

The effect of forward bias in the dark could be similar to light illumination under open circuit condition. In the application of either RLS or forward bias, an increase in the minority carrier concentration is seen in the absorber bulk. This transient effect can be reversed by dark annealing at 340–360 K.

(e) Reverse Bias

When a reverse bias is applied under standard conditions of –1 V for 1 h at 300K, the junction capacitance is increased and the *FF* reduced [37]. C-V profiling reveals spatially inhomogeneous increase in space charge density at intermediate distance from the junction [26, 35, 38]. As such, the red kink becomes more pronounced. From the higher capacitance value, one might conclude that the application of the reverse bias does not bring the device back to its relaxed state, but produces an alternative metastable state [26]. Deep level transient spectroscopy (DLTS) experiments reveal a defect level of 0.35 eV after reverse bias, and annealing the sample at 340–360 K can reverse this effect back to the cell's relaxed state. The effect of reverse bias, observed for shaded cells in deployed solar modules, is seen to have more adverse effects on chemical bath deposited (CBD) buffer layers [19], and even more so for alternative buffers [39]. This effect can be reduced by annealing [19].

2.5.2. Changes of I-V parameters due to metastabilities

So far, the discussions of external stimuli induce metastable changes in two quantifiable I-V parameters, the V_{OC} and *FF*, illustrated in the I-V graphs in Figure 2.11. The mechanisms related to transient V_{OC} and *FF* losses can be associated in different components in the CIGS device stack, hence they have to be explained separately.

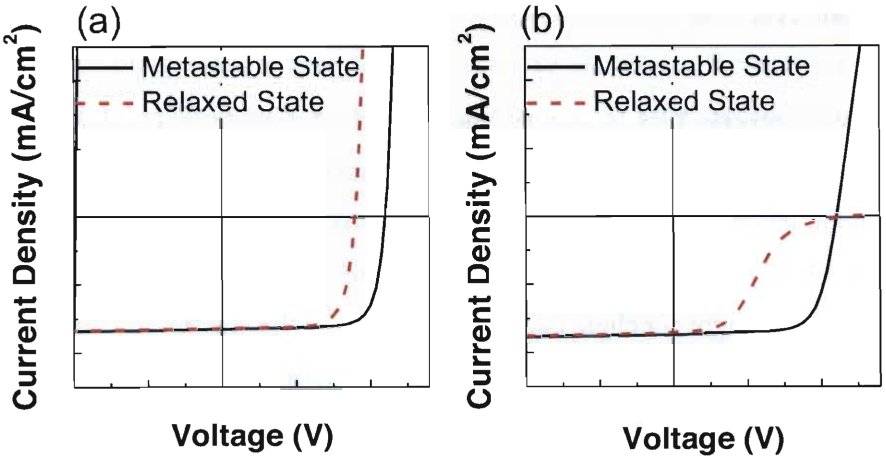

Figure 2.11 I-V curves depicting metastability from (a) Open circuit voltage loss and (b) Fill factor loss.

It is possible to discuss contributing factors that lead to losses in the V_{OC} and *FF* when one breaks down the layers of a CIGS stack into three separate components for discussion. As illustrated in Figure 2.12, V_{OC} losses have been associated to (a) back contact barrier, and more commonly (b) the recombination in the CIGSSe bulk, as it is seen to be limited mainly by the absorber. *FF* losses are more interface-related, hence changes in (c) the CIGSSe/buffer interface, are more relevant to explain the appearance of the 'red kink', or electronic barrier in Figure 2.11 (b).

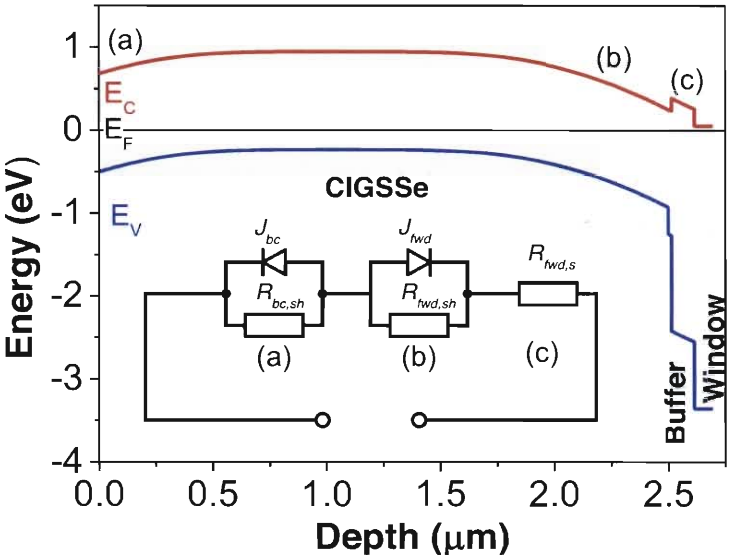

Figure 2.12 Band diagram of a CIGSSe device at 0 V with (a) back contact/CIGSSe interface, (b) CIGSSe bulk, and (c) CIGSSe/buffer interface translated into an electrical circuit with components (a) Back current, J_{bc} and parallel resistance, $R_{bc,sh}$, (b) Forward current, J_{fwd} and parallel resistance, $R_{fwd,sh}$, and (c) series resistance in the direction of the front current $R_{fwd,s}$.

2.5.3. Open-circuit Voltage related Metastabilities

The CIGS bulk has been widely discussed as the key limitation for improvement of efficiencies [40-42]. Furthermore, V_{OC} changes by external stimulus have been attributed to metastable point defects or elemental diffusion, which affects the band alignment and electric field [43, 44].

When one considers the basic stoichiometry of the chalcopyrite $Cu(In,Ga)(S,Se)_2$ absorber, it is likely that vacancies or interstitials might form when there is a deficit or surplus of the elements: copper, indium, gallium, selenium, and sulfur. From DFT calculations [45-47], it has been demonstrated that certain shallow or deep trap states are likely to form from varying the composition in the CIGS absorber. They are verified experimentally by techniques like admittance spectroscopy, which can obtain defect activation energies especially of shallow interface defects with designated N1 signature when applied at 0 V bias. Deep defects, termed as the N2 bulk defect, can be determined with the application of a dc bias, but only if they can cross the E_F when bias is applied to change the electric field [48, 49].

At lower temperatures of 77–150 K, contribution from the back contact barrier plays a part in limiting the saturation current of the back contact diode on the forward current of the main diode, resulting in a lowered V_{OC} value [50].

(a) V_{Cu}-V_{Se} divacancy

Pertaining to the origin of metastability from the transient reduction and recovery of the V_{OC}, one of the most cited theories proposed by Lany and Zunger is the V_{Cu}-V_{Se} divacancy [51] defect complex, which has the ability to convert between detrimental V_{OC} limiting shallow level donor in the device's relaxed state to a shallow level acceptor in its light soaked state, indicated by a rise of $N_{a,abs}$ by C-V profiling. This mechanism has been shown to occur under reverse bias or red/white light soaking, reducing the inversion between the *p-n* junction and increasing the overall capacitance.

(b) In_{Cu} antisites

The second possibility is In_{Cu} antisites [21, 41] that undergo shallow-to-deep transition after electron capture by the same electrical or light induced external stimulus. As such, the compensation level is reduced and $N_{a,abs}$ is increased [37]. Consequently, SCR is shortened, which implies reduction of SRH recombination which mainly occurs in the SCR, and V_{OC} increases.

As both V_{Cu}-V_{Se} and In_{Cu} are shallow defects and have low defect E_a, the interpretation of the E_a derived from the admittance data cannot be standalone and needs to be substantiated by an understanding of the stoichiometry of the elements present.

(c) Mobile Cu^+ ion migration

The third possibility is a consequence of migration of mobile copper ions (diffusion constant = 10^{-13}–10^{-10} cm^2/s) across the SCR [52, 53], which has been experimentally proven to occur in a few minutes to several days. An out-diffusion of Cu into the CdS layer leads to a change in the distribution across the electric field of the SCR. A secondary effect of this out-diffusion process is the creation of V_{Cu} that contributes to electrical metastabilities discussed in the case of the amphoteric V_{Cu}-V_{Se} divacancy above.

For CdS-buffered CIGS devices made during the pioneering years of CIGS research, metastability was mainly attributed to V_{OC} effects, and this has been implicitly linked to the absorber fabrication method [36]. Over time, as incremental progress was made for the fabrication step, this effect has been reduced [23, 54-56] particularly in sputter-prepared absorbers, and admittance steps attributed to defects do not always show up in these devices [57].

From admittance spectroscopy results, an N1 defect, attributed to a shallow defect, exists in PVD-In_2S_3 and is speculated to occur at the same level as a CdS-buffered reference cell [58, 59]. Even though the CdS device studied displayed significant changes to its I-V parameter indicative of metastability, the same N1 signature did not change in the physical vapor deposited (PVD) In_2S_3 device, where the E_F stayed constant [60]. This led to the conclusion that the same defect signature might not apply to alternative buffer systems.

(d) Back Contact

Back contact issues related to metastabilities are typically described as interface issues for minority carrier recombination at the back contact. When the voltage crosses the V_{OC}, it is expected that a voltage drop at the back contact results in a blocking behavior at the reverse diode illustrated in Figure 2.11(a). As a result, the total current saturates and leads to a kink in the I-V curve. A decrease in the back contact barrier, quantified by the E_a of the N1 admittance signature, results in the disappearance of the roll-over. This effect is temperature-dependent and is not visible at room temperature. Besides majority carriers saturating at the back contact, there is a possibility that light of long wavelengths will penetrate far into the absorber, resulting in generation of electrons far away from the SCR [50, 61]. Electrons produced by light of long wavelength generate a photocurrent opposing the direction of the photocurrent of the main diode. Under forward bias, there is a reduced SCR at the *p*-*n* junction. This indirectly influences the back contact and increases its barrier height, resulting in the so-called red-kink, or rollover, in the I-V curve.

2.5.4. Fill Factor related Metastabilities

As it is an interface-related issue that mainly affects R_s, transient losses related to *FF* with a characteristic rollover in the illuminated I-V curve often accompanied with a crossover of the illuminated and dark I-V curve. This implies that one of the interfaces, typically the absorber/buffer/window conduction band discontinuities illustrated in Figure 2.12(c), is creating an electron barrier that leads to a large voltage drop across the buffer in the dark relaxed state of the device. Light irradiation passivates these states and brings the conduction band alignment to a more optimal condition.

(a) p+ layer at absorber/buffer interface

From within the SCR close to the absorber/buffer interface, an N1 signature has been identified as a shallow donor defect ($E_a \approx 120$ meV) [62] for co-evaporated CIGS samples. Aside from contributions to V_{OC} losses, this defect level has been postulated to pin the Fermi-level at the heterointerface, which prohibits a change in effective conduction band barrier during the application of a voltage bias when CdS doping increases. This can be imagined as a highly *p*-type region at the absorber side of the absorber/buffer interface which results in band bending, creating a photocurrent barrier [9, 37]. Blue light stimulus generates holes within the CdS layer, which are trapped in the p+ layer, resulting in the reduction of the space charge density, band bending, and photocurrent barrier. Applying a negative bias reverses this effect, increasing the p+ layer and the photocurrent barrier, and reducing the *FF* with a characteristic red kink in the illuminated I-V curve.

(b) Conduction band offset at absorber/buffer interface

When discussing discontinuity of bands at the *p-n* junction, one has to consider the offset between the conduction bands of the absorber and buffer as a barrier for electron collection at the *n*-side of the device. Eisgruber *et al.* showed that introducing a spike at the conduction band of the CIGS/CdS interface ($+\Delta E_C^{CIGSe/CdS}$) resulted in a barrier of a few hundred meV for separated electrons originating from the absorber [32]. The consequence of a larger barrier during red light illumination compared to white light illumination is an impeded electron collection.

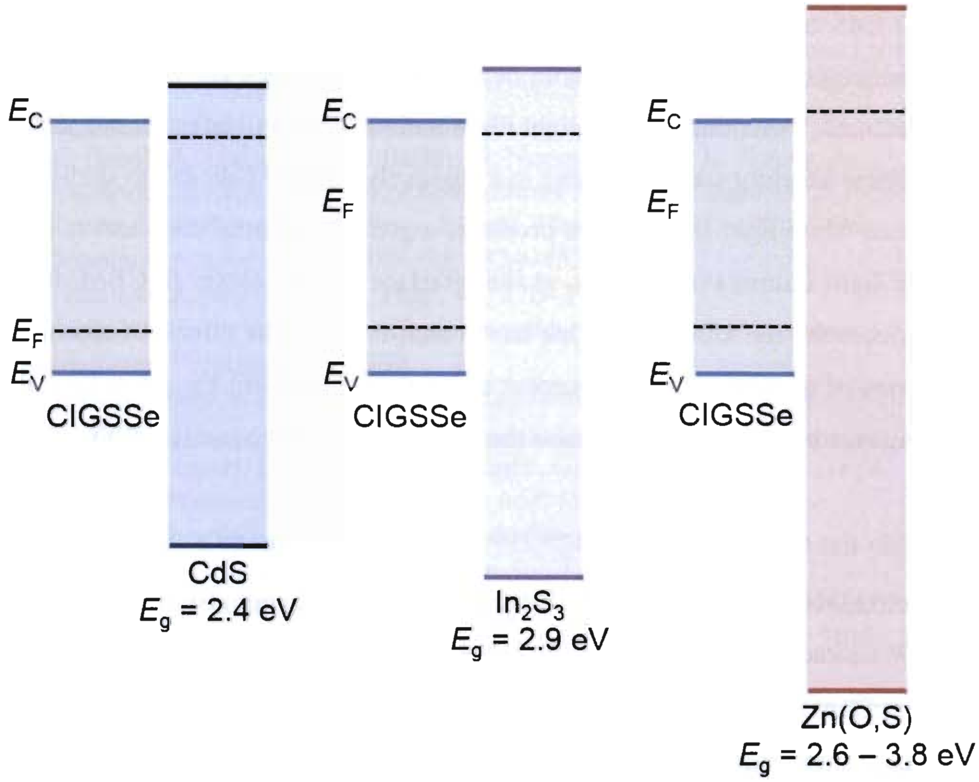

Figure 2.13 Band alignment of *p*-CIGSSe (E_g = 1.1 eV) with *n*-CdS (E_g = 2.4 eV), *n*-In_2S_3 (E_g = 2.9 eV), and *n*-Zn(O,S) (E_g = 2.6–3.8 eV).

When replacing CdS with indium sulfide ($E_g^{In_2S_3}$ = 2.9 eV, indirect band gap) or zinc (oxy)sulfide ($E_g^{ZnO_xS_y}$ = 2.6–3.8 eV, direct band gap) buffers [63-65], one has to consider that the band alignment changes with respect to the absorber (Figure 2.13). It is expected that the ZnO$_x$S$_y$ will have a larger $+\Delta E_C^{CIGSe/ZnO_xS_y}$ than CdS or In$_2$S$_3$, and this has been shown to further limit the electron collection even during white light illumination unless the band gap can be lowered by considering the bowing parameter of the $E_g^{ZnO_xS_y}$ with respect to the oxygen to sulfur composition [66, 67].

(c) Deep acceptor states in buffer

An additional factor influencing the charge separation is the presence of defect states within the buffer bulk. In addition to shallow *n*-type doping, deep acceptor states also exist within the CdS bulk, resulting in compensation of the *n*-type buffer [32, 68]. Under red light illumination, the negligible hole density results in occupation of the acceptor states by electrons. Switching to white light illumination, holes will be generated instead and trapped at these acceptor states, resulting in a positively charged CdS due to shallow *n*-type doping. Since white light illumination produces a greater potential drop across the absorber than red light illumination, the E_{fn} at the interface will be closer to CBM during WLS. This reduces the red kink effect. One has to then consider the effects of changing the buffer in terms of quantity of deep acceptor states that come with the alternative material, which might either increase or decrease the barrier between the *p*-*n* junction.

With the consideration of $\Delta E_C^{CIGSe/Buffer}$, Pudov *et al*. made a study comparing CdS, ZnO, InS(O,OH) buffers and their responses to red or white light illumination [30]. Based on the I-V characteristics with ZnO and InS(O,OH) systems, red kinks are found to exist even at room temperature. This was postulated to be dependent on the $\Delta E_C^{CIGSe/Buffer}$value. The CBO theory [69, 70], together with deep compensating acceptor states in the buffer bulk [71], were proposed to be applicable for alternative buffer layers.

References

[1] W. Shockley, *Bell System Technical Journal* **1949**, *28*, 435–489.
[2] W. Shockley, *Electrons and holes in semiconductors: with applications to transistor electronics*, Van Nostrand, **1950**.
[3] S. Chih-Tang, R. N. Noyce, W. Shockley, *Proceedings of the IRE* **1957**, *45*, 1228–1243.
[4] J. L. Moll, *Proceedings of the IRE* **1958**, *46*, 1076–1082.
[5] S. M. Sze, K. K. Ng, *Physics of Semiconductor Devices*, Wiley, **2006**.
[6] R. L. Anderson, *IBM J. Res. Dev.* **1960**, *4*, 283–287.
[7] S. H. Wei, A. Zunger, *Appl. Phys. Lett.* **1993**, *63*, 2549–2551.
[8] S. H. Wei, A. Zunger, *J. Appl. Phys.* **1995**, *78*, 3846–3856.
[9] A. Niemegeers, M. Burgelman, R. Herberholz, U. Rau, D. Hariskos, H. W. Schock, *Prog. Photovoltaics Res. Appl.* **1998**, *6*, 407–421.
[10] T. Löher, W. Jaegermann, C. Pettenkofer, *J. Appl. Phys.* **1995**, *77*, 731–738.
[11] S.-H. Wei, S. B. Zhang, A. Zunger, *Appl. Phys. Lett.* **1998**, *72*, 3199–3201.
[12] T. Walter, A. Content, K. O. Velthaus, H. W. Schock, *Sol. Energy Mater. Sol. Cells* **1992**, *26*, 357–368.
[13] B. M. Başol, A. Halani, C. Leidholm, G. Norsworthy, V. K. Kapur, A. Swartzlander, R. Matson, *Prog. Photovoltaics Res. Appl.* **2000**, *8*, 227–235.
[14] M. Turcu, I. M. Kötschau, U. Rau, *J. Appl. Phys.* **2002**, *91*, 1391–1399.
[15] C. Donolato, *J. Appl. Phys.* **1989**, *66*, 4524–4525.
[16] C. Donolato, *Appl. Phys. Lett.* **1985**, *46*, 270–272.
[17] M. A. Green, *Solar cells: operating principles, technology, and system applications*, Prentice-Hall, **1982**.
[18] R. H. Bube, *Photoelectronic Properties of Semiconductors*, Cambridge University Press, **1992**.
[19] U. Rau, K. Weinert, Q. Nguyen, M. Mamor, G. Hanna, A. Jasenek, H. W. Schock, *MRS Online Proceedings Library* **2001**, *668*, H9.1.
[20] A. Zunger, *Thin Solid Films* **2007**, *515*, 6160–6162.
[21] M. Igalson, A. Urbaniak, M. Edoff, *Thin Solid Films* **2009**, *517*, 2153–2157.
[22] J. Serhan, Z. Djebbour, W. Favre, A. Migan-Dubois, A. Darga, D. Mencaraglia, N. Naghavi, G. Renou, J. F. Guillemoles, D. Lincot, *Thin Solid Films* **2011**, *519*, 7606–7610.
[23] K. Kushiya, S. Kuriyagawa, K. Tazawa, T. Okazawa, M. Tsunoda, in *Conference Record of the 2006 IEEE 4th World Conference on Photovoltaic Energy Conversion, Vol. 1*, **2006**, pp. 348–351.
[24] T. Meyer, F. Engelhardt, J. Parisi, U. Rau, *J. Appl. Phys.* **2002**, *91*, 5093–5099.
[25] F. Engelhardt, M. Schmidt, T. Meyer, O. Seifert, J. Parisi, U. Rau, *Phys. Lett. A* **1998**, *245*, 489–493.
[26] U. Rau, A. Jasenek, R. Herberholz, H. W. Schock, J. F. Guillemoles, D. Lincot, L. Kronik, *Proc. 2nd World Conf. On Photovolt. Energy Conv* **1998**, 428.
[27] Y.-J. Zhao, C. Persson, S. Lany, A. Zunger, *Appl. Phys. Lett.* **2004**, *85*, 5860–5862.
[28] M. Igalson, A. Kubiaczyk, P. Zabierowski, *MRS Online Proceedings Library* **2001**, *668*, H9.2.

[29] T. Meyer, M. Schmidt, F. Engelhardt. J. Parisi, U. Rau, *Eur. Phys. J. - Appl. Phys.* **1999**, *8*, 43–52.
[30] A. O. Pudov, J. R. Sites, M. A. Contreras, T. Nakada, H. W. Schock, *Thin Solid Films* **2005**, *480–481*, 273–278.
[31] P. Zabierowski, U. Rau, M. Igalson, *Thin Solid Films* **2001**, *387*, 147–150.
[32] I. L. Eisgruber, J. E. Granata, J. R. Sites, J. Hou, J. Kessler, *Sol. Energy Mater. Sol. Cells* **1998**, *53*, 367–377.
[33] R. Kniese, M. Powalla, U. Rau, *Thin Solid Films* **2007**, *515*, 6163–6167.
[34] R. Herberholz, U. Rau, H. W. Schock, T. Haalboom, T. Gödecke, F. Ernst, C. Beilharz, K. W. Benz, D. Cahen, *Eur. Phys. J. Appl.* **1999**, *6*, 131–139.
[35] M. Igalson, M. Cwil, M. Edoff, *Thin Solid Films* **2007**, *515*, 6142–6146.
[36] M. N. Ruberto, A. Rothwarf, *J. Appl. Phys.* **1987**, *61*, 4662–4669.
[37] M. Igalson, M. Bodegård, L. Stolt, A. Jasenek, *Thin Solid Films* **2003**, *431–432*, 153–157.
[38] M. Igalson, M. Cwil, M. Edoff, *Proceedings of the 20th European Photovoltaic Solar Energy Conference, Barcelona (ed. W.Palz, H. Ossenbrink, P. Helm)* **2005**, 1800.
[39] M. Igalson, C. Platzer-Björkman, *Sol. Energy Mater. Sol. Cells* **2004**, *84*, 93–103.
[40] M. Igalson, P. Zabierowski, D. Prządo, A. Urbaniak, M. Edoff, W. N. Shafarman, *Sol. Energy Mater. Sol. Cells* **2009**, *93*, 1290–1295.
[41] S. Siebentritt, M. Igalson, C. Persson, S. Lany, *Prog. Photovoltaics Res. Appl.* **2010**, *18*, 390–410.
[42] Q. Cao, O. Gunawan, M. Copel, K. B. Reuter, S. J. Chey, V. R. Deline, D. B. Mitzi, *Adv. Energy Mater.* **2011**, *1*, 845–853.
[43] D. Schmid, M. Ruckh, F. Grunwald, H. W. Schock, *J. Appl. Phys.* **1993**, *73*, 2902–2909.
[44] M. Igalson, H. W. Schock, *J. Appl. Phys.* **1996**, *80*, 5765–5769.
[45] S. Niki, R. Suzuki, S. Ishibashi, T. Ohdaira, P. J. Fons, A. Yamada, H. Oyanagi, T. Wada, R. Kimura, T. Nakada, *Thin Solid Films* **2001**, *387*, 129–134.
[46] T. Maeda, T. Wada, *J. Phys. Chem. Solids* **2005**, *66*, 1924–1927.
[47] T. Maeda, T. Wada, *Phys. Status Solidi C* **2009**, *6*, 1312–1316.
[48] T. Walter, R. Herberholz, C. Müller, H. W. Schock, *J. Appl. Phys.* **1996**, *80*, 4411–4420.
[49] T. Eisenbarth, T. Unold, R. Caballero, C. A. Kaufmann, D. Abou-Ras, H. W. Schock, *Thin Solid Films* **2009**, *517*, 2244–2247.
[50] A. Niemegeers, M. Burgelman, *J. Appl. Phys.* **1997**, *81*, 2881–2886.
[51] S. Lany, A. Zunger, *J. Appl. Phys.* **2006**, *100*, 113725.
[52] J. F. Guillemoles, *Thin Solid Films* **2002**, *403–404*, 405–409.
[53] J. F. Guillemoles, *Thin Solid Films* **2000**, *361–362*, 338–345.
[54] J. A. del Cueto, S. Rummel, B. Kroposki, C. Osterwald, A. Anderberg, in *Photovoltaic Specialists Conference, 2008. PVSC '08. 33rd IEEE*, **2008**, pp. 1–6.
[55] S. Spiering, D. Hariskos, S. Schröder, M. Powalla, *Thin Solid Films* **2005**, *480–481*, 195–198.
[56] D. J. Coyle, H. A. Blaydes, R. S. Northey, J. E. Pickett, K. R. Nagarkar, R.-A. Zhao, J. O. Gardner, *Prog. Photovoltaics Res. Appl.* **2013**, *21*, 173–186.
[57] W. Witte, D. Hariskos, M. Powalla, *Thin Solid Films* **2011**, *519*, 7549–7552.

[58] Z. Djebbour, A. Darga, A. Migan Dubois, D. Mencaraglia, N. Naghavi, J. F. Guillemoles, D. Lincot, *Thin Solid Films* **2006**, *511–512*, 320–324.
[59] A. Darga, D. Mencaraglia, Z. Djebbour, A. M. Dubois, R. Chouffot, J. Serhan, F. Couzinié-Devy, N. Barreau, J. Kessler, *Thin Solid Films* **2009**, *517*, 2423–2426.
[60] K. Macielak, M. Igalson, S. Spiering, in *2011 37th IEEE Photovoltaic Specialists Conference (PVSC)*, **2011**, pp. 002763–002767.
[61] T. Eisenbarth, T. Unold, R. Caballero, C. A. Kaufmann, H.-W. Schock, *J. Appl. Phys.* **2010**, *107*, 034509.
[62] R. Herberholz, M. Igalson, H. W. Schock, *J. Appl. Phys.* **1998**, *83*, 318–325.
[63] D. Hariskos, S. Spiering, M. Powalla, *Thin Solid Films* **2005**, *480–481*, 99–109.
[64] N. Naghavi, G. Renou, V. Bockelee, F. Donsanti, P. Genevee, M. Jubault, J. F. Guillemoles, D. Lincot, *Thin Solid Films* **2011**, *519*, 7600–7605.
[65] W. Witte, S. Spiering, D. Hariskos, *Vakuum in Forschung und Praxis* **2014**, *26*, 23–27.
[66] C. Platzer-Björkman, T. Törndahl, D. Abou-Ras, J. Malmström, J. Kessler, L. Stolt, *J. Appl. Phys.* **2006**, *100*, 044506.
[67] S. Merdes, V. Malinen, F. Ziem, I. Lauermann, M. Schüle, F. Stober, F. Hergert, N. Papathanasiou, R. Schlatmann, *Sol. Energy Mater. Sol. Cells* **2014**, *126*, 120–124.
[68] H. Jingya, S. J. Fonash, J. Kessler, in *Photovoltaic Specialists Conference, 1996., Conference Record of the Twenty Fifth IEEE*, **1996**, pp. 961–964.
[69] T. Nakada, M. Hongo, E. Hayashi, *Thin Solid Films* **2003**, *431–432*, 242–248.
[70] H. Hori, T. Minemoto, H. Takakura, *Curr. Appl Phys.* **2010**, *10*, S150–S153.
[71] M. Igalson, A. Urbaniak, P. Zabierowski, H. A. Maksoud, M. Buffiere, N. Barreau, S. Spiering, *Thin Solid Films* **2013**, *535*, 302–306.

Chapter 3

Fabrication and Characterization of Cadmium-free $Cu(In,Ga)(S,Se)_2$ Solar Cells

In this chapter, the fabrication steps of a typical $Cu(In,Ga)(S,Se)_2$ *solar cell is described. In particular, the fabrication step of the buffer is described in detail since the different deposition techniques are compared in this PhD thesis in subsequent chapters. This is followed by the description of standard electrical characterization techniques of the I-V parameters, external quantum efficiency, and temperature dependent I-V, C-V and C-f measurements. Next, the standard materials characterization methods employed in the thesis are described, namely X-ray photoemission spectroscopy and time-of-flight secondary ion mass spectrometry. Finally, the SCAPS-1D simulation tool* [1], *which is used throughout this PhD work in understanding the mechanism(s) of metastability, is introduced at the end of this chapter.*

3.1. Fabrication of $Cu(In,Ga)(S,Se)_2$ Solar Cells

The growth process for CIGSSe thin-film solar cells used in this study is depicted schematically in Figure 3.1. A standard deposition process is carried out in the following order: sputtering deposition of 1–3 μm molybdenum onto soda-lime glass, followed by deposition of 1–2 μm CIGSSe either by a one-stage or three-stage co-evaporation process or sputtering [2]. This work uses two-stage sputtered CIGSSe absorbers made by Bosch Solar CISTech GmbH [3]. A buffer of 20–50 nm is applied on the finished absorber by chemical bath deposition (CBD). Other methods of buffer deposition for alternative buffer layers are discussed in detail in Section 3.1.1. Finally, sputtering deposition of intrinsic zinc oxide (*i*-ZnO) and aluminum-doped zinc oxide (AZO) completes the cell. Typically, an aluminum/nickel grid is added to improve charge collection of electrons.

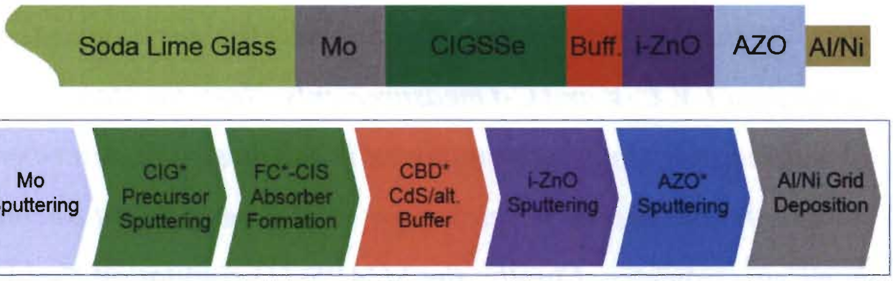

Figure 3.1 Fabrication steps of CIGSSe devices from 1) Mo sputtering, 2) CIG precursor sputtering, 3) CIS Absorber Formation by Forced Convection, 4) Chemical Bath Deposition of CdS or Alternative buffers, 5) intrinsic ZnO sputtering, 6) Al-doped ZnO sputtering, and 7) Al/Ni Grid Deposition [3].

3.1.1. Buffer Layer and Deposition Techniques

Modifications to the buffer layer are the centerpiece of the PhD work, hence they will be addressed in greater detail. The *n*-type buffer layer has several functions in the CIGSSe solar cell. First, it is placed next to the *p*-type absorber to form a heterojunction (discussed in greater detail in Section 2.1) while allowing the maximum amount of light to pass through to the absorber [4]. Additionally, the buffer protects the absorber from sputter damage during subsequent *i*-ZnO/AZO deposition [5]. Since the buffer is necessary to bridge the misalignment between CIGSSe and the *i*-ZnO/AZO window [6], the criteria for a good buffer is its compatibility when aligning the interfaces of CIGSSe/buffer and buffer/window.

The current world record CIGS solar cell, at 22.3% cell efficiency, is achieved with CBD-Zn(O,S) [7]. Conventional CBD-CdS buffered solar cells closely follows this record at 21.7% [8]. There is a great interest in replacing CdS for several reasons. As the toxicity of the material poses a major threat to the environment and cause health problems in humans when ingested in small quantities, a wide-scale industrial ban was imposed in the European Union for usage of CdS in production [9]. Besides, the relatively small E_g^{CdS} of 2.4 eV limits the amount of light of 350–550 nm passing through to the absorber, resulting in a smaller current generation and potentially limiting the efficiency of the solar cell. Also, it is more attractive to complete all the layers of the CIGSSe solar cell without breaking vacuum, as oxygen and other atmospheric gases might introduce undesired side products at the surface of the absorber [10, 11].

These criteria have prompted many groups to search for an optimal Cd-free buffer over the past 25 years, with the aim to achieve equal or better records than that have been set by the CdS buffer. Table 3.1 summarizes the current records for promising alternative buffers with the CdS buffer as a benchmark, with their corresponding deposition methods and achieved efficiencies on $Cu(In,Ga)Se_2$ and $Cu(In,Ga)(S,Se)_2$ absorbers [12, 13].

Table 3.1 World-record efficiencies for thin film solar cells of 0.5 cm^2 comprising of CdS, alternative Zn(O,S) and In_2S_3 buffers with $Cu(In,Ga)Se_2$ and $Cu(In,Ga)(S,Se)_2$ absorber.

Buffer	**Deposition**	**Efficiency (%)**	
		$Cu(In,Ga)Se_2$	$Cu(In,Ga)(S,Se)_2$
CdS	CBD	21.7 [8]	
Zn(O,S)	CBD		22.3 [7]
	ALD	18.7 [14]	16.1 [15]
	Sputtered	18.3 [16]	16.4 [17]
In_2S_3	CBD	15.7 [18]	
	ALD	16.4 [19]	
	PVD		17.1 [17]

The standard deposition techniques for buffers utilized in CIGS solar cells fabrication are illustrated in Figure 3.2. They are namely (a) Chemical Bath Deposition (CBD), (b) Atomic Layer Deposition (ALD), (c) Thermal Evaporation, and (d) Sputtering. The CBD and ALD techniques utilized in this study will be discussed further in the following subsection.

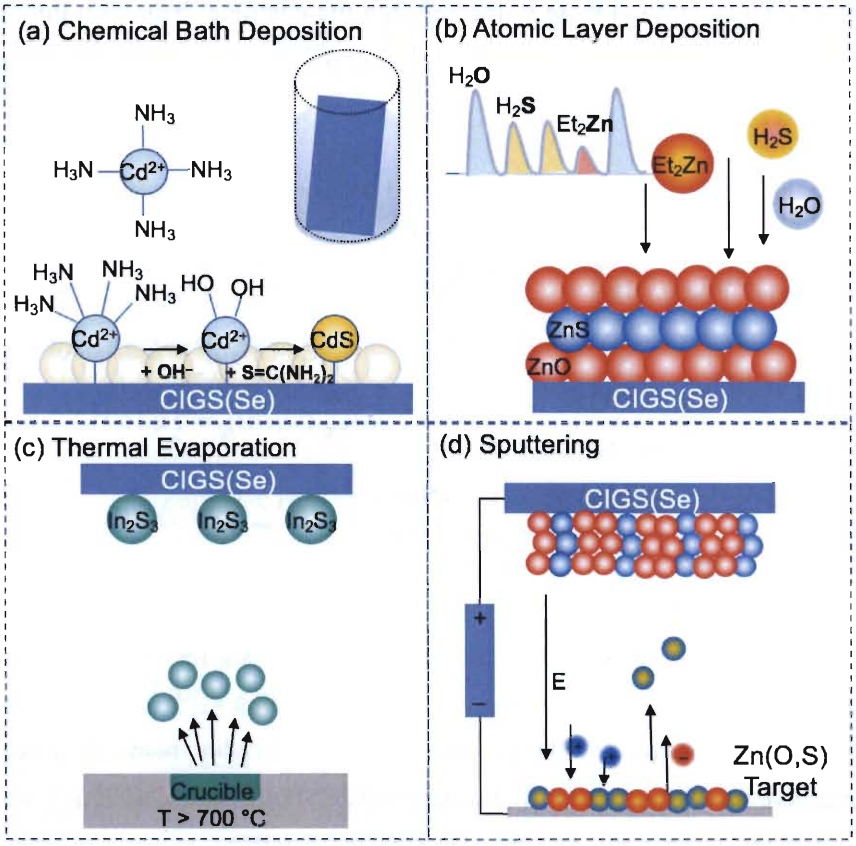

Figure 3.2 Deposition Techniques for buffers (a) Chemical Bath Deposition, (b) Atomic Layer Deposition, (c) Thermal Evaporation, and (d) Sputtering.

(a) Chemical Bath Deposition (CBD)

The most standard way to deposit the buffer layer is CBD. This process has often yielded champion/high efficiency CdS-buffered solar cells of up to 21.7% [20]. CBD-Zn(O,S) have also seen remarkable success in implementation, reaching up to 22.3% [7].

The mechanism in the standard CBD process involves a chemical precipitation of CdS or ZnS from the starting material of the cadmium or zinc salt, a sulfur precursor, and ammonium hydroxide. The standard reagents were cadmium or zinc acetate ($Cd(CH_3COO)_2$) or ($Zn(CH_3COO)_2$) and thiourea ($SC(NH_2)_2$) and NH_3 dissolved in deionized water and heated to a temperature of 70 °C. At this temperature, the CIGSSe absorbers (substrates) were immersed into the chemical bath with the dissolved precursor solution. After 15 min immersion, a 50 nm thin buffer layer (CdS or ZnS) was deposited onto the substrate.

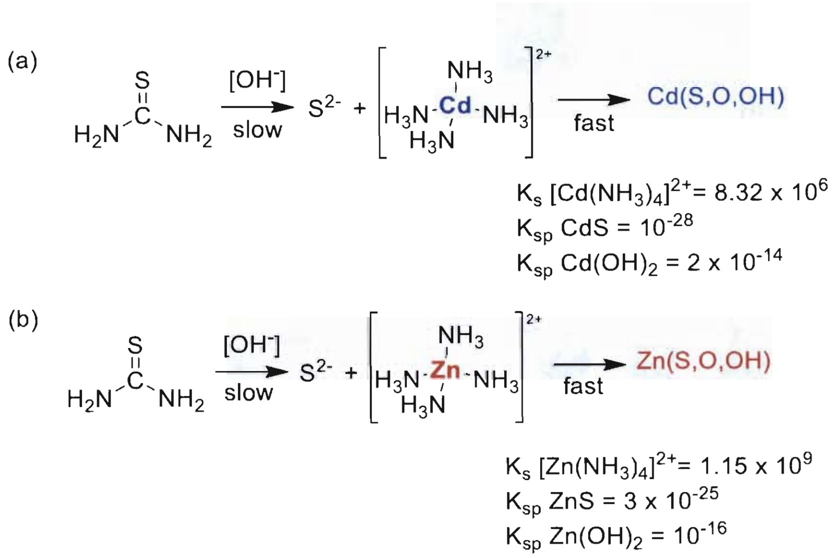

Figure 3.3 Key steps in CBD processes involving (a) cadmium and (b) zinc precursors, with the respective solubility constant (K_s) values of $[Cd(NH_3)_4]^{2+}$ and $Zn(NH_3)_4]^{2+}$ and solubility product constant (K_{sp}) values of CdS, $Cd(OH)_2$, ZnS, and $Zn(OH)_2$.

Inclusion of additives or changing the pH of the solution [21] may accelerate or inhibit the growth process of the buffer, and the control of thickness of the material can be achieved to a great effect. A positive side effect of immersing the absorber into the solution involves ammonia etching, which removes undesired oxidized materials on the absorber surface [22].

(b) Atomic Layer Deposition (ALD)

The ALD process has been successfully demonstrated with Zn(O,S) [14, 15, 23, 24] and In_2S_3 [25-27] buffers. A modification of the chemical vapor deposition (CVD) process, the ALD method introduces reactants in sequential pulses in gaseous phases to the absorber placed in the reactor, growing the buffer in monolayers as a function of time [27]. The ALD method demonstrates its superiority over other methods in control of the buffer stoichiometry and thickness. One key limitation of the ALD process is its long deposition time compared to the other methods discussed.

The ALD Zn(O,S) films were deposited by a Cambridge Nanotec Fiji 200 system using diethylzinc ($Zn(C_2H_5)_2$, DEZ, purchased from Aldrich, >99%), H_2O (18 MΩ/cm) and H_2S (2.5 % balanced in Ar) as the zinc, oxygen and sulfur sources, respectively. The chemical reactions occurring in the reaction chamber is described as follows:

$$Zn(CH_3CH_2)_2 + H_2S \rightarrow ZnS + 2CH_3CH_3 \tag{3.1}$$

$$Zn(CH_3CH_2)_2 + H_2O \rightarrow ZnO + 2CH_3CH_3 \tag{3.2}$$

The pulsing sequence for DEZ:Ar:H_2O or H_2S:Ar cycles had pulse lengths of 0.08 s: 10 s : 0.08 s for H_2O or 0.1 s for H_2S : 10 s. The precursor temperature, reaction chamber and the precursor delivery line were maintained at 120 °C throughout the experiments. During the deposition process, a 40 sccm high purity argon gas was used as the process and purging gas, and the chamber pressure was maintained at 106 Pa. The [O]:[S] content of the film was controlled by varying the S and O precursor pulse ratio in the ALD cycle. A pulse ratio using an average of six DEZ:Ar:H_2O:Ar cycles for every DEZ:Ar:H_2S:Ar cycle resulted in a Zn(O,S) layer with $[O]:[S] \approx 6:1$.

3.2 Standard Electrical and Optical Characterizations

There are a few methods to characterize the fundamental properties of CIGSSe devices by means of extracting their I-V parameters, which will be introduced in this section. Data collection and interpretation of the specific technique follows in the subsections.

The standard room temperature I-V test setup is illustrated in Figure 3.4. A Xenon Lamp was calibrated to AM1.5G condition in order to evaluate the performance of CIGSSe devices under standardized testing conditions. For the exclusion of metastability effects during the illuminated I-V testing of a batch of 10 solar cells adjacent to each other, a black piece of paper was used to cover adjacent 9 cells with a cut out of size 0.5 cm^2 to perform the I-V characterization for the 1 device-under-test. The derivation of the I-V curve from its parameters has been discussed in Section 2.3.

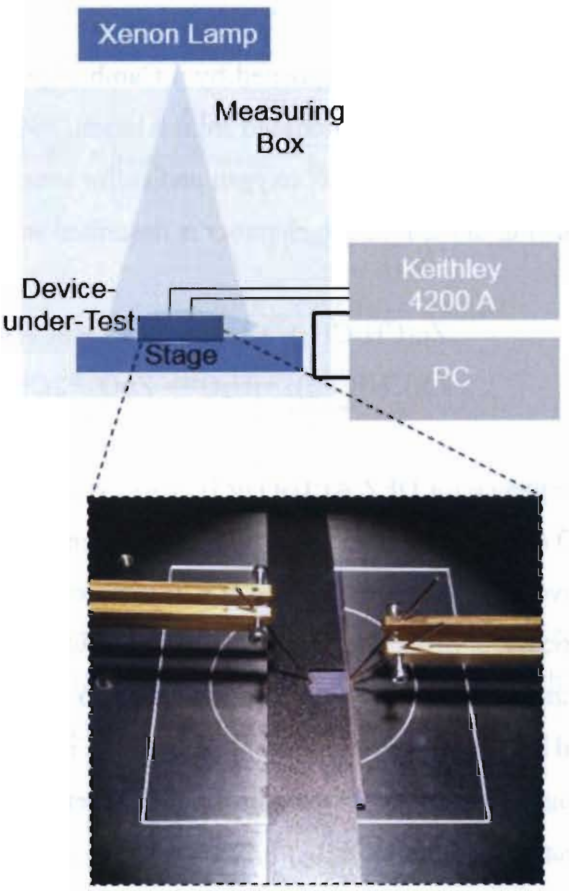

Figure 3.4 Standard Dark and Illuminated I-V measurement set up at 298 K.

The test setup for low-temperature electrical measurements for the current-voltage (I-V), capacitance-voltage (C-V), and capacitance-frequency (C-f) test setup is illustrated in Figure 3.5. A 50W Osram Halogen lamp was calibrated to AM1.5G condition to evaluate the performance of CIGSSe devices under standardized testing conditions. The device-under-test was mounted on a test stage perpendicular to the light source, and placed in an Oxford Optistat DN-V Cryostat and cooled under nitrogen to 77 K. Between 90–360 K, I-V, C-V, and C-f measurements were performed by switching between the Agilent 4155C (I-V) and the HP 4192A LCR analyzer (C-V, C-f). I-V measurements were performed with the calibrated AM1.5G lamp intensity, and additionally with filters reducing the lamp intensity to 50%, 10%, and 1%. Dark I-V measurements were also performed at each temperature step. The capacitance measurements (C-V and C-f) were performed under the frequency test range of 100–1,000,000 Hz. The lamp intensity of the Osram lamp and the measurement settings are controlled from the LabView software in the PC, which is connected to the HP 4192A and Agilent 4155C via GPIB cables.

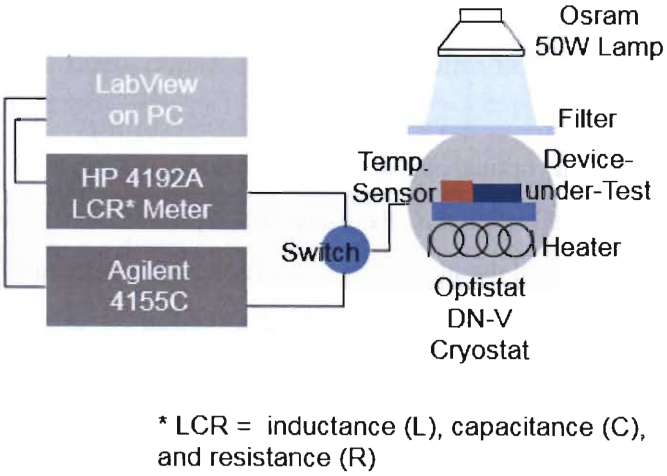

Figure 3.5 Temperature-Dependent Measurement of 1) Current-Voltage on Agilent 4155C and 2) Capacitance-Voltage and Capacitance-Frequency on HP 4192A.

3.2.1. Quantum Efficiency Measurements

While the I-V measurement yields the absolute value of J_{SC} in the solar cell, it does not give insight about the loss mechanism responsible for limitations in the CIGSSe solar cell. In an ideal CIGSSe solar cell within the Shockley-Queisser limit, every photon with $E > E_g^{CIGSSe}$ is expected to translate into one electron-hole pair generated and collected at the front and back electrodes. In reality, losses occur within the solar cell. Spectral resolution of the J_{SC} by means of varying the wavelength of light injected leads to the expression of the external quantum efficiency (EQE) as the number of electrons collected for each photon reaching the solar cell with

$$EQE(\lambda) = \frac{1}{e}\frac{dJ_{SC}(\lambda)}{d\Phi(\lambda)} \tag{3.5}$$

where $d\Phi(\lambda)$ (units: Φ=cm^{-2}s^{-1}) is the incident photon flux in the photon energy interval $d\lambda$ leading to dJ_{SC}.

Under realistic operating conditions of a CIGSSe solar cell, the quantum yield is < 1, even if the $E > E_g^{CIGSSe}$. The reasons for a lower than expected EQE yield come from optical (parasitic absorption or reflection) or recombination losses.

Reflection-related optical losses can be evaluated with a spectrometer capable of determining the reflectance R. An integrating sphere is built into the spectrometer for this function. The internal quantum efficiency (IQE) is then defined by the number of collected electrons for a given number of photons absorbed in the solar cell

$$IQE(\lambda) = \frac{EQE(\lambda)}{1 - R(\lambda)} \tag{3.6}$$

From the plot of the EQE measurement (Figure 3.6), it is possible to determine E_g^{CIGSSe} as the optical response of the absorber typically tails off at around 1100–1400 nm, hence yielding charge collection properties at this layer [28, 29]. At the high energy region of 300–500 nm, it is possible to distinguish the differences of charge collection of different buffer layers by the level of response at these wavelengths [30].

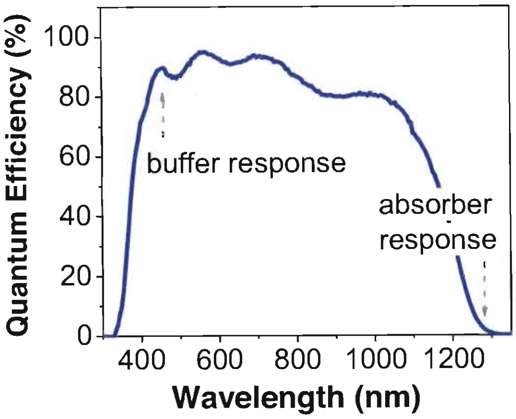

Figure 3.6 Typical EQE measurement of a Zn(O,S)/CIGSSe Solar Cell.

3.2.2. Temperature-Dependent Current/Voltage Measurements

The temperature dependence of equilibrium concentration of electrons and/or holes affects the rate of recombination and thus is linked to the V_{OC}. By considering this relationship of the V_{OC} with temperature, the intensity of light was fixed at each temperature step to keep the J_{SC} constant, and extend equation 2.28 to express J_{SC} as [31]:

$$J_{SC} = J_0\left[\exp\left(\frac{eV_{OC}}{n_{id}kT}\right)-1\right] = J_{00}\exp\left(\frac{-E_a}{n_{id}kT}\right)\left[\exp\left(\frac{eV_{OC}}{n_{id}kT}\right)-1\right] \qquad (3.3)$$

Where J_{00} is the weakly temperature-dependent pre-factor of the saturation current density J_0. From there, we derive a direct correlation between the V_{OC} and the E_a.

$$eV_{OC} = E_a - n_{id}kT\ln\left(\frac{J_{00}}{J_{SC}}\right) \qquad (3.4)$$

As long as the presumption that J_{00} and J_{SC} are relatively independent of temperature holds, equation 3.2 at 0 K will be independent of the ideality factor term. V_{OC} (0 K) may be extrapolated by plotting the high temperature V_{OC} to derive the E_a, equivalent to the band gap value at 0 K (Figure 3.7). From this, bulk and interface recombination may be distinguished by comparing the V_{OC} (0 K) with the band gap energy determined by the stoichiometry of the CIGSSe or optical methods. If the eV_{OC} (0 K) is equivalent to the E_g^{CIGSSe}, a dominant bulk recombination path is present in the device. Otherwise, if the eV_{OC} (0 K) is lower than E_g^{CIGSSe}, then it implies that V_{OC} is limited by interface recombination, hence, the E_a corresponds to a contact barrier Φ_b in the device [32, 33].

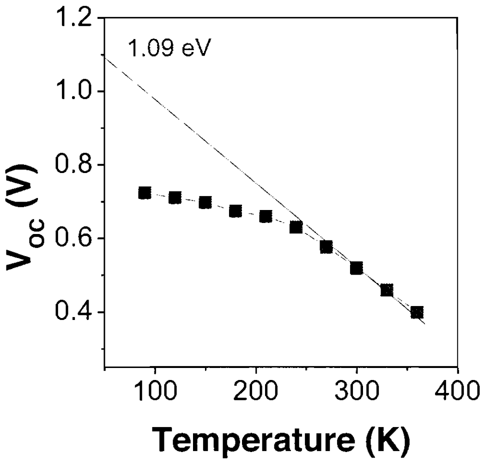

Figure 3.7 Typical plot of V_{OC} vs Temperature for a Zn(O,S)/CIGSSe device where bulk recombination predominates.

3.2.3. Capacitance-Voltage

Capacitance-Voltage (C-V) profiling is used for the investigation of traps/defects in the *p-n* heterojunction of CIGSSe solar cells. With the assumption that the depletion region ends abruptly and is totally depleted of free carriers, the more lightly doped *p*-side (i.e. the CIGSSe) where the space charge region (SCR) predominantly occurs is profiled. A change in the applied bias leads to a widening or shortening of the depletion width (w_{SCR}), while charge density $\rho(x)$ in this region stays constant, considering A is the area of the device-under-test. By ensuring an alternating current (ac) frequency longer than the free carrier relaxation time, the capacitance response will come from the depletion edge [34, 35].

$$C = \frac{\varepsilon\varepsilon_0 A}{w} \tag{3.7}$$

Expanding on the equation 2.5 where assuming a one-sided p^+-n junction allows for the calculation of the w_{SCR}, the capacitance-voltage is now included and derived as

$$w_{SCR} = \sqrt{\frac{2\varepsilon\varepsilon_0 (V_{bi} - V_{dc})}{eN_{CV}}} \tag{3.8}$$

where V_{dc} is the applied direct current (dc) bias in each step of the capacitance-voltage profiling and N_{CV} is the doping profile in the depleted region. This is illustrated in Figure 3.8.

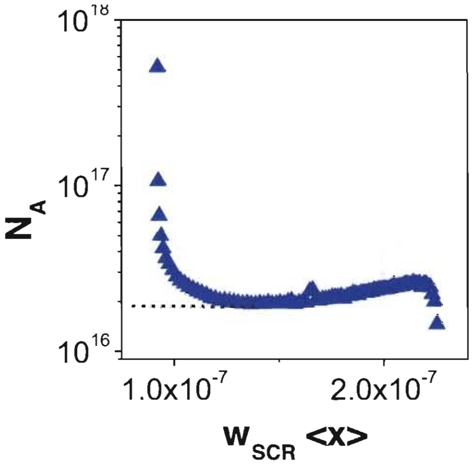

Figure 3.8 Typical Doping profile of a Zn(O,S)/CIGSSe device derived from C-V measurement with equation 3.8.

Thereafter, the Mott-Schottky plot can be derived by the following

$$\frac{1}{C^2} = \frac{2(V_{bi} - V_{dc})}{e\varepsilon\varepsilon_0 A^2 N_{CV}} \tag{3.9}$$

from which the intercept will yield the built-in potential, V_{bi}, and the slope corresponds to doping profile in the depleted region, N_{CV}. N_{CV} can then be expressed as

$$N_{CV} = -\frac{2}{e\varepsilon\varepsilon_0 A^2}\left[\frac{d(V_{dc})}{d(1/C^2)}\right] = -\frac{C^3}{e\varepsilon\varepsilon_0 A^2}\left(\frac{dV_{dc}}{dC}\right) \tag{3.10}$$

The capacitance response in the depletion approximation originates singularly from the depletion region edge, and as such, this is true when N_{CV} varies with the distance from the junction with equation 3.7.

3.2.4. Time Resolved Photoluminescence

In a typical time resolved photoluminescence (TRPL) experiment, photoexcitation of a device with a 650 nm laser generated by a quartz laser system at room temperature, illustrated in Figure 3.9. The laser pulse width is 200 ns, with a pulse rate of 5 MHz, and a beam diameter of 1 μm. Photoluminescence decay curves were measured at ~1200–1300 nm by a Germanium detector with time-correlated single-photon counting [36]. The injection level was fixed at ~5 x 10^{12} photons/cm^2 per pulse (low injection, negligible amount of electrons in the absorber compared to holes) on full devices.

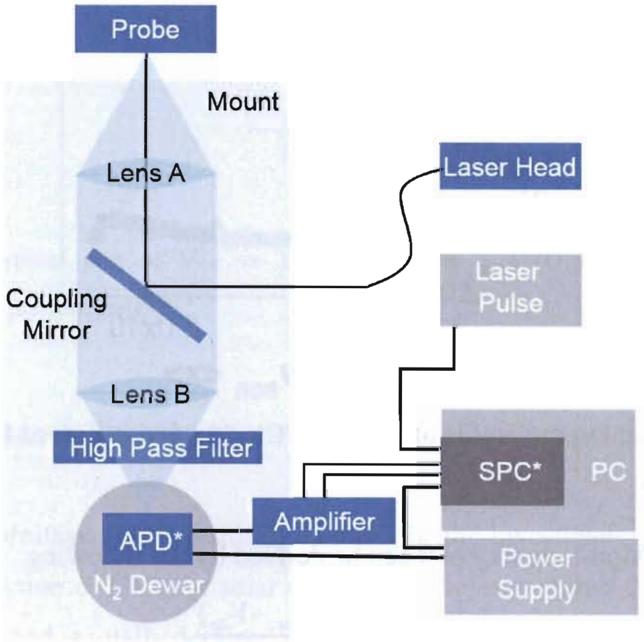

* APD = Avalanche Photo Diode
SPC = Simple Photon Counting Module

Figure 3.9 Setup for Time-Resolved Photoluminescence Experiment.

Considering that CIGS devices undergo one (or two) exponential decay lifetimes, the equation for fitting the minority carrier lifetimes of III-V compound semiconductors with TRPL derived by Ahrenkiel [37] was modified to the following

$$I_{PL}(t) = A_1 e^{(\frac{-t}{\tau_1})} + A_2 e^{(\frac{-t}{\tau_2})} \qquad (3.14)$$

When interpreting the TRPL decay lifetimes, the conditions at which the experiment are made must be considered in order to understand the possible mechanisms contributing to decay(s). From fitted lifetime values, the causes of charge separation and recombination were analyzed on the basis of results of one-dimensional simulations performed with Synopsys TCAD® by Scheer *et al.*[38, 39].

3.2.5.1. Low Injection

During low injection, a full device is irradiated with a laser pulse under open circuit conditions, assuming a 0 V bias. Two effects, namely the screening effect of the SCR, and radiative recombination, have to be considered under this condition.

A. Screening effect of Space Charge Region

Under low injection, there is a pronounced increase in drift effects, and this results in a fast decay time due to charge separation. The separated electrons and holes accumulate at the edge of the SCR as majority carriers. The charge carriers that move to the QNR recombine, but the majority carriers at the edge of the SCR remain since the density of their recombination partners, the minority carriers at each edge, remain low. As a result, a large V_{OC} build up occurs due to a charge storage. While the recombination is limited by a small diffusion current of the majority carriers across the SCR, a large decay time occurs after the period of time when the V_{OC} is increased.

However, in real experiments, only drift, diffusion, and bulk recombination are the major routes for separated charges, hence charge storage effects can be excluded. One advantage of selecting a low injection multi-pulse experiments is to minimize this photovoltage bias that cannot be avoided under high injection experiments, since it will reduce the background luminescence intensity.

B. Recombination

Under low injection, only radiative recombination needs to be considered as the rest of the recombination mechanism only takes place when sufficient minority carriers/energy are available for these mechanisms to occur. They are discussed in Section 3.2.5.2. for high injection recombination.

Radiative recombination:

$$R_r = Bpn \tag{3.15}$$

Under this condition, the diffusion does not affect decay due to a low photogenerated carrier density. Assuming a bi-exponential decay pathway under low injection as a function of time t and distance x, the net-radiative recombination becomes

$$R_{rad}(t,x) = B_1 p_0 \Delta n(t,x) + B_2 p_0 \Delta n(t,x) \tag{3.16}$$

for a low photogenerated carrier density. B_1 *and* B_2 are constants and p_0 is the equilibrium hole density. By integrating the amount of excess electrons Δn generated over the distance d, the intensity I relative to time is obtained by

$$I(t) = \int_0^d R_{rad}(t,x)dx = B_1 p_0 \int_0^d \Delta n(x)dx + B_2 p_0 \int_0^d \Delta n(x)dx \tag{3.17}$$

By considering that diffusion (τ_1) and SRH recombination (τ_2) contribute separately to the total number of generated carriers, the total PL intensity generated might be derived by summing up the two component as equation 3.14. Due to a homogeneous hole density at low injection level ($p(x) \approx p_0$), recombination probability for electrons is equally distributed and independent of the whole electron population.

3.2.5.2. High Injection

A. Screening effect of Space Charge Region

Under high injection, charge separation occurs and carriers accumulate at the edge of the SCR. This results in screening of the electric field, and consequentially, no drift effects can be observed.

Additionally, considering that multi-pulse excitation at high injection leads to incomplete voltage decay after each pulse, over time, more charge carriers are generated and screening takes place eventually. This creates luminescence that adds to background and shifts intensity higher. This hinders interpretation of decay time due to recombination.

B. Recombination

Aside from radiative recombination, Shockley-Read-Hall (SRH) recombination and Auger recombination have to be considered during high injection experiments since they come to predominate under this condition.

Auger recombination:

$$R_e = Bpn^2 \tag{3.18}$$

$$R_h = Bp^2n \tag{3.19}$$

SRH recombination:

$$R_{SRH} = \frac{\sigma_p \sigma_n v_{th} N_t [p_n - n_i^2]}{\sigma_n [n + n_i \exp(E_t - E_i / kT)] + \sigma_p [p + n_i \exp(E_i - E_t / kT)]} \tag{3.20}$$

At low defect densities, SRH recombination is predominant, as excess minority carriers will recombine with defects near the midgap, with

$$R_{SRH} = \sigma v_{th} N_t = \frac{1}{\tau_{SRH}} \tag{3.21}$$

assuming a value of σ, when capture cross-section $\sigma_n = \sigma_p$ and N_t is the volume density of defect centers.

Typically, the minority carrier decay rate will be governed by the following in cases of high injection:

$$\frac{-d\Delta n}{dt} = A\Delta n + B\Delta n^2 + C\Delta n^3 \tag{3.22}$$

where A, B, and C describe the strengths of the SRH recombination, radiative recombination, and Auger recombination, respectively. One must consider two scenarios when analyzing recombination mechanisms under high injection levels: low defect density and high defect density.

Increment of the injection level renders the defect recombination inefficient only when defect densities are low, since SRH lifetime $\tau = \tau_{n0} + \tau_{p0}$ with $\tau_{p0} = 1/\sigma_p v_d N_d$ since $\tau_{n0} + \tau_{p0} >>$

$1/B_{p0} = \tau_{rad}$, radiative recombination starts to dominate, increasing the transient decay time. Even higher injection leads to bi-exponential decay that comes as a consequence of diffusion effect and bimolecular recombination.

For high defect densities, the increment of injection leads to increment of the SRH lifetime, since $\tau = \tau_{n0} + \tau_{p0} << \tau_{rad}$. This results in a larger lifetime. However, non-radiative SRH recombination still predominates.

3.3. Standard Materials Characterizations

Besides understanding the electrical parameters of devices, the material properties (i.e. chemical composition, oxidation states of elements, grain size) allows for the assessment of fundamental characteristics of these devices and enable a link of electrical characterizations to material changes (if any). In this subsection, material characterization techniques common to the field and utilized in this PhD study are introduced.

3.3.1. X-ray Photoemission Spectroscopy

The principles of X-ray Photoemission Spectroscopy (XPS) is based on the photoelectron effect. An X-ray photon of energy $h\upsilon$ exceeding the sum of the binding energies of the electron E_{BE} and work function Φ impacts a surface which emits a photoelectron with kinetic energy of E_{KE}. This phenomenon was first described by Einstein with the following equation [40]

$$E_{KE} = h\upsilon - E_{BE} - \Phi \tag{3.23}$$

As depicted in Figure 3.10(a), expulsion of an electron from the atom leaves an electron vacancy at its original energy level. Two mechanisms can result from an electron, which then moves from level E2 to E1 to repopulate the vacancy left by the first core electron that was lost to the X-ray photon. The first is Auger emission ((b) in Figure 3.10), in which the energy is transferred from E2 to E3 resulting in expulsion of an Auger electron with an emission signal. The second is an X-ray emission ((c) in Figure 3.10) when the electron transits from E2 to E1. These processes can be utilized in Auger electron spectroscopy (AES) or X-ray fluorescence (XRF) to characterize chemical compositions.

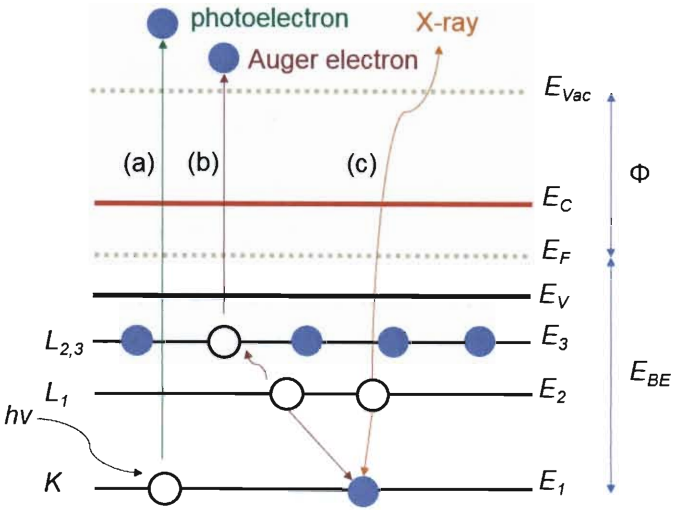

Figure 3.10 Irradiation of material surface by $h\upsilon > \Phi + E_{BE}$ resulting in (a) the expulsion of a photoelectron, and subsequent filling of vacancy by (b) Auger process or (c) X-ray fluorescence process.

Photoelectrons are detected in XPS experiments, from which elemental composition and the chemical environment of these elements can be understood. From the characteristic binding energies of each element, it is possible to determine the chemical state and binding to other elements by considering chemical shifts in the peak positions [41, 42].

Line intensity allows us to determine the peak area, which corresponds to the atomic ratio of each element detected at the surface. The correlation of the intensity is described in the following

$$I \propto \sigma(h\upsilon)\times JL_A(\gamma)\times T(E_{KE})\times c_A \times \lambda_A(E_{KE})\cos\theta \tag{3.24}$$

$\sigma(h\upsilon)$ depicts the photoionization cross section for the emission line, which depends on the element's core level and excitation energy, J is the X-ray flux, $L_A(\lambda)$ is the angular asymmetry parameter of the photoelectron line, λ is the angle between the incident X-ray photons and outgoing photoelectrons, c_A is the elemental concentration, $\lambda_A(E_{KE})$ is the inelastic mean free path of electrons, and θ is the angle between the emission of photoelectrons and the normal relative to the sample. The analysis transmission function $T(E_{\mathrm{KE}})$ follows the approximation $T \approx E_{KE}^{-1/2}$ [43, 44]. Presetting the axis at 55° between the X-ray tube and spectrometer axis [45], the angular asymmetry parameter can be assumed to be negligible in the calculation. The elemental ratio may then be determined by the comparison of the intensity of the emission lines from two elements

$$\frac{C_A}{C_B} = \frac{I_A\sqrt{E_{KE,A}}\,\sigma_B\lambda_B}{I_B\sqrt{E_{KE,B}}\,\sigma_A\lambda_A} \tag{3.25}$$

Further simplification can be made if the two elements have similar E_{KE} values for their selected lines

$$\frac{C_A}{C_B} = \frac{I_A\sigma_B\lambda_B}{I_B\sigma_A\lambda_A} \tag{3.26}$$

3.3.2. Electron Microscopy

Electron microscopy is a technique that utilizes a highly energized electron beam to bombard a sample specimen in order to produce images down to the angstrom range. It becomes possible to analyze the respective layers and interfaces of CIGSSe devices and thin-films completed up to a certain layer in the device stack. Additionally, it is also possible to sample the local elemental composition at an area of interest by an energy-dispersive X-ray (EDX) detector that often comes along with the microscope. Two techniques are employed to give images of different magnification.

Scanning electron microscopy (SEM) is useful for the study of materials down to 1 nm. It is extremely useful to get an overview of the cross-section of the thin film and the chemical composition, and makes use of secondary and backscattered electrons to image samples. The morphology and surface topography of samples show up under secondary electron bombardment, whilst the compositional contrasts in the different layers of the thin film are imaged by backscattered electrons.

Transmission electron microscopy (TEM) is performed by first preparing an ultrathin specimen by focus ion beam (FIB), then placing the specimen on a holder. Electrons from the beam transmits through the specimen elastically and inelastically and produce an image that distinguishes denser regions by dark shades and thinner regions by lighter shades.

3.3.3. Time of Flight Secondary Ion Mass Spectrometry

Time of Flight Secondary Ion Mass Spectroscopy (TOF-SIMS) is a technique utilized in characterization of impurities, doping profiles, intermixing of elements at the CIGSSe/buffer/window heterojunction, and composition of elements in CIGSSe thin film solar cells. It is one of the most sensitive techniques (range: ppm) for profiling the distribution of elements relative to its depth in the material [46, 47]. In addition, sputtered crater depth measurements can determine the actual depth of the material to great accuracy. High end instruments also incorporate a micron-scale mapping function of individual atom's positions on the probed surface.

The operating principle of TOF-SIMS is as follows: sputtering of the sample surface by a beam composing of ionized species in the gas phase which are electropositive (Cs^+), electronegative (O_2^+), or inert (Ar^+). This step removes species from the surface which are then passed through an aperture and deflected by an applied electric field, which allows the different kinetic energies of each species to be distinguished from one another. The kinetic energy follows $E=1/2\ mv^2$, where m is the ion mass and v is the velocity of the ion. The term E may be calculated from the secondary ion accelerating field. The time taken for the ion to travel to the detector can be used to calculate its mass.

In order to make the most reliable quantitative analyses of the SIMS data to compare different CIGSSe samples, it is necessary to standardize the operating conditions (i.e. sputtering speed, power of the beam) for each measurement. Even so, it is usually not likely to attain quantitative compositions within a factor of two, hence other complementing methods like XPS and SEM-EDX are necessary to cross-reference the distribution of elements in the material. The different material hardness's have to be accounted for when sputtering across heterojunctions, as the sputtering is relative to time and requires an additional crater depth profiling to adjust the depth profile to a correct scale relevant to the CIGSSe device thickness.

3.4. SCAPS-1D Simulation

As discussed in Section 2.2, the continuity equations describe the basis of the behavior of electrons and holes in semiconductor devices like the CIGSSe solar cells. The SCAPS-1D simulation tool [1] operates on Poisson's equation and steady-state continuity equations

$$\nabla(\varepsilon\nabla\Psi) = q(p - n + N_D^+ - N_A^-) \tag{3.27}$$

$$\nabla J_h = q(G - R_h) \tag{3.28}$$

$$\nabla J_e = -q(G - R_e) \tag{3.29}$$

Ψ in equation 2.14 describes the electric potential, p and n are hole and electron carrier densities, ε is the electric permittivity of the semiconductor, N_D^+ and N_A^- are the ionized donor and acceptor densities, J_h and J_e are the hole and electron current densities, G is the carrier generation, and R_h and R_e are the recombination rates of holes and electrons.

The continuity equations 2.15 and 2.16 describe charge conservation, whereby net current flow from a small volume equals net generation of charge carriers. The appropriate boundary equations should be considered when solving these equations.

In addition to the fundamental semiconductor equations, the transport equations describing the drift and diffusion terms in current flow are also important. They are described in the following for holes and electrons, where the first term constitutes the drift in the electric field and the second term, the diffusion driven by carrier concentration gradients

$$J_h = q\mu_h p\nabla\Psi - qD_h\nabla p \tag{3.30}$$

$$J_e = q\mu_e n\nabla\Psi + qD_e\nabla n \tag{3.31}$$

μ_h and μ_e are the hole and electron mobilities, and D_h and D_e are the diffusion coefficients of holes and electrons. Other factors beyond these fundamental properties should be considered. Their contributions to current transport, including tunneling, compositional gradients lead to different doping levels, temperature dependency of transport, band gap, density of states, resistivity of materials, and electron affinity, and have to be evaluated when appropriate [48].

Beyond these fundamental equations that are the basis of SCAPS, the program is able to solve elaborate variations of these equations in one dimension. Maxwell-Boltzmann statistics is applied to determine band and defect state occupations. Approximation of Fermi-Dirac statistics applies for semiconductors that do not have extremely high doping, when the Fermi level lies within the band gap. Current transport also considers tunneling effects [49, 50]. With these properties accounted for, the I-V, C-V, EQE, and C-f measurements discussed in 3.2 can all be simulated by SCAPS and compared against actual data.

It is possible to describe the grading of the CISSe layer with different stoichiometries of indium to gallium, and correspondingly decrease or increase the band gap of the absorber layer at different positions. Defects of neutral, acceptor, donor, or amphoteric types may be defined at the bulk of a specific layer or at an interface. In order to further customize the properties of front and back contacts specific to the user's devices, their absorption coefficients and reflections may be pre-defined by the user and imported as text files. Furthermore, the absorption coefficients of each layer are available from the preset compositions available that can be flexibly tuned to the composition of one's devices by changing the grading parameter [49].

Table 3.2 describes the standard parameters that are utilized in this PhD thesis to simulate different variations of the buffer properties that possibly contribute to *FF* losses in CIGSSe/Zn(O,S) devices. Baseline parameters are determined from literature [51].

No modifications were made to the back contact, which was assumed to be ohmic since the thin $MoSe_2$ formed between the Mo and CIGSSe layer is thin and does not show up at low temperatures [52-54]. The CIGSSe absorber composition was determined by SIMS and XPS, and approximated by linear and parabolic functions to achieve band gap grading in the layer at different positions. At its sulfur-rich surface close to the buffer, a thin ordered vacancy compound (OVC) layer was assumed due to the low copper, intermediate indium, and high sulfur content that makes the formation of $CuIn_5S_8$ thermodynamically feasible [55]. The Zn(O,S) buffer was considered to have a band gap between 2.6 and 3.8 eV [56, 57], and in a standard simulation, conduction band offset was assumed to be absent. The net doping was assumed to be 1 x 10^{18} cm^{-3} donors. For the intrinsic ZnO and Al-doped ZnO layers, literature values were used for the values assuming electron mobilities and net doping densities are similar as the literature [58].

Table 3.2 Parameters of a standard CIGSSe/Zn(O,S) device in this PhD thesis utilized in SCAPS-1D simulations. $S_{e,h}$: recombination velocity of electrons or holes; Φ_b: contact barrier; d: thickness; E_g: band gap of material; χ_e: electron affinity; ε: dielectric permittivity; $\mu_{e,h}$: electron or hole mobility; $v_{th,e,h}$: thermal velocity of electrons or holes; $N_{C,V}$: effective density of states in conduction or valence band; N_d: shallow *n*-type doping density; N_a: shallow *p*-type doping density; N_t: defect density; E_t: defect energy; $\sigma_{e,h}$: capture cross section for electrons or holes; $\tau_{e,h}$: lifetime of electrons and holes; $L_{e,h}$: diffusion length of electrons or holes.

		Contacts		
	Front	Back		
S_e (cm/s)	1×10^7	1×10^7		
S_h (cm/s)	1×10^7	1×10^7		
Φ_b (eV)	0	0		
		Layers		
	CIGSSe	OVC	Zn(O,S)	*i*-ZnO
d (μm)	1.6	0.015	0.05	0.08
E_g (eV)	1.03	1.5	3.6	3.4
χ_e (eV)	4.5	4.5	4.5*	4.55
ε	10	10	10	10
μ_e (cm^2/Vs)	100	1	50*	50
μ_h (cm^2/Vs)	20	1	20	20
$v_{th,e}$ (cm/s)	1×10^7	1×10^7	1×10^7	1×10^7
$v_{th,h}$ (cm/s)	1×10^7	1×10^7	1×10^7	1×10^7
N_C (cm^{-3})	2×10^{18}	2×10^{18}	2×10^{18}	4×10^{18}
N_V(cm^{-3})	2×10^{18}	2×10^{18}	1.5×10^{19}	9×10^{18}
N_d (cm^{-3})		1×10^{13}	1×10^{18}	5×10^{17}
N_a (cm^{-3})	1×10^{16}			

References

[1] M. Burgelman, P. Nollet, S. Degrave, *Thin Solid Films* **2000**, *361–362*, 527–532.

[2] S. Niki, M. Contreras, I. Repins, M. Powalla, K. Kushiya, S. Ishizuka, K. Matsubara, *Prog. Photovoltaics Res. Appl.* **2010**, *18*, 453–466.

[3] V. Probst, I. Koetschau, E. Novak, A. Jasenek, H. Eschrich, F. Hergert, T. Hahn, J. Feichtinger, M. Maier, B. Walther, V. Nadenau, *IEEE J. Photovoltaics* **2014**, *4*, 687-692.

[4] A. Niemegeers, M. Burgelman, R. Herberholz, U. Rau, D. Hariskos, H. W. Schock, *Prog. Photovoltaics Res. Appl.* **1998**, *6*, 407–421.

[5] N. F. Cooray, K. Kushiya, A. Fujimaki, I. Sugiyama, T. Miura, D. Okumura, M. Sato, M. Ooshita, O. Yamase, *Sol. Energy Mater. Sol. Cells* **1997**, *49*, 291–297.

[6] A. E. Delahoy, A. Ruppert, M. Contreras, *Thin Solid Films* **2000**, *361–362*, 140–144.

[7] http://www.solar-frontier.com/eng/news/2015/C051171.html, **2015**.

[8] M. A. Green, K. Emery, Y. Hishikawa, W. Warta, E. D. Dunlop, *Prog. Photovoltaics Res. Appl.* **2016**, *24*, 3–11.

[9] http://echa.europa.eu/documents/10162/7d11129c-0343-41fa-97c7-50228401ee66, **2013**.

[10] D. Hariskos, S. Spiering, M. Powalla, *Thin Solid Films* **2005**, *480–481*, 99–109.

[11] T. Sakurai, N. Ishida, S. Ishizuka, M. M. Islam, A. Kasai, K. Matsubara, K. Sakurai, A. Yamada, K. Akimoto, S. Niki, *Thin Solid Films* **2008**, *516*, 7036–7040.

[12] N. Naghavi, D. Abou-Ras, N. Allsop, N. Barreau, S. Bücheler, A. Ennaoui, C. H. Fischer, C. Guillen, D. Hariskos, J. Herrero, R. Klenk, K. Kushiya, D. Lincot, R. Menner, T. Nakada, C. Platzer-Björkman, S. Spiering, A. N. Tiwari, T. Törndahl, *Prog. Photovoltaics Res. Appl.* **2010**, *18*, 411–433.

[13] W. Witte, S. Spiering, D. Hariskos, *Vakuum in Forschung und Praxis* **2014**, *26*, 23–27.

[14] T. Kobayashi, Z. Jehl, L. Kao, T. Nakada, *28th European Photovoltaic Solar Energy Conference and Exhibition* **2013**, 2199–2202.

[15] S. Merdes, F. Ziem, T. Lavrenko, T. Walter, I. Lauermann, M. Klingsporn, S. Schmidt, F. Hergert, R. Schlatmann, *Prog. Photovoltaics Res. Appl.* **2015**, *23*, 1493–1500.

[16] R. Klenk, A. Steigert, T. Rissom, D. Greiner, C. A. Kaufmann, T. Unold, M. C. Lux-Steiner, *Prog. Photovoltaics Res. Appl.* **2014**, *22*, 161–165.

[17] M. Powalla, W. Witte, P. Jackson, S. Paetel, E. Lotter, R. Wuerz, F. Kessler, C. Tschamber, W. Hempel, D. Hariskos, R. Menner, A. Bauer, S. Spiering, E. Ahlswede, T. M. Friedlmeier, D. Blazquez-Sanchez, I. Klugius, W. Wischmann, *IEEE J. Photovoltaics* **2014**, *4*, 440–446.

[18] D. Hariskos, M. Ruckh, U. Rühle, T. Walter, H. W. Schock, J. Hedström, L. Stolt, *Sol. Energy Mater. Sol. Cells* **1996**, *41–42*, 345–353.

[19] N. Naghavi, S. Spiering, M. Powalla, B. Cavana, D. Lincot, *Prog. Photovoltaics Res. Appl.* **2003**, *11*, 437–443.

[20] http://www.zsw-bw.de/uploads/media/pr12-2014-ZSW-WorldrecordCIGS.pdf.

[21] A. Ennaoui, M. Bär, J. Klaer, T. Kropp, R. Sáez-Araoz, M. C. Lux-Steiner, *Prog. Photovoltaics Res. Appl.* **2006**, *14*, 499–511.

[22] J. Kessler, K. O. Velthaus, M. Ruckh, R. Laichinger, H. W. Schock, D. Lincot, *6th International Photovoltaic Science and Engineering Conference: Proceedings* **1992**.

[23] J. R. Bakke, J. S. King, H. J. Jung, R. Sinclair, S. F. Bent, *Thin Solid Films* **2010**, *518*, 5400–5408.

[24] T. Kobayashi, T. Kumazawa, L. Kao, T. Nakada, *Sol. Energy Mater. Sol. Cells* **2013**, *119*, 129–133.

[25] J. Sterner, J. Malmström, L. Stolt, *Prog. Photovoltaics Res. Appl.* **2005**, *13*, 179–193.

[26] S. Spiering, D. Hariskos, S. Schröder, M. Powalla, *Thin Solid Films* **2005**, *480–481*, 195–198.

[27] E. B. Yousfi, B. Weinberger, F. Donsanti, P. Cowache, D. Lincot, *Thin Solid Films* **2001**, *387*, 29–32.

[28] J. Parisi, D. Hilburger, M. Schmitt, U. Rau, *Sol. Energy Mater. Sol. Cells* **1998**, *50*, 79–85.

[29] R. Kniese, M. Lammer, U. Rau, M. Powalla, *Thin Solid Films* **2004**, *451–452*, 430–433.

[30] F. Engelhardt, L. Bornemann, M. Köntges, T. Meyer, J. Parisi, E. Pschorr-Schoberer, B. Hahn, W. Gebhardt, W. Riedl, U. Rau, *Prog. Photovoltaics Res. Appl.* **1999**, *7*, 423–436.

[31] U. Rau, H. W. Schock, *Appl. Phys. A* **1999**, *69*, 131–147.

[32] M. Turcu, I. M. Kötschau, U. Rau, *J. Appl. Phys.* **2002**, *91*, 1391–1399.

[33] S. S. Hegedus, W. N. Shafarman, *Prog. Photovoltaics Res. Appl.* **2004**, *12*, 155–176.

[34] L. C. Kimerling, *J. Appl. Phys.* **1974**, *45*, 1839–1845.

[35] J. T. Heath, J. D. Cohen, W. N. Shafarman, *J. Appl. Phys.* **2004**, *95*, 1000–1010.

[36] D. V. O'Connor, D. Phillips, *Time-correlated single photon counting*, Academic Press, London; Orlando, **1984**.

[37] R. K. Ahrenkiel, *Solid-State Electron.* **1992**, *35*, 239–250.

[38] M. Maiberg, R. Scheer, *J. Appl. Phys.* **2014**, *116*, 123710.

[39] M. Maiberg, R. Scheer, *J. Appl. Phys.* **2014**, *116*, 123711.

[40] R. Scheer, H. W. Schock, *Chalcogenide Photovoltaics: Physics, Technologies, and Thin Film Devices*, Wiley, **2011**.

[41] C. D. Wagner, G. E. Muilenberg, *Handbook of x-ray photoelectron spectroscopy: a reference book of standard data for use in x-ray photoelectron spectroscopy*, Physical Electronics Division, Perkin-Elmer Corp., **1979**.

[42] P. YU, M. Cardona, *Fundamentals of Semiconductors: Physics and Materials Properties*, Springer Berlin Heidelberg, **2013**.

[43] L. Weinhardt, *Elektronische und chemische Eigenschaften von Grenzflächen und Oberflächen in optimierten Cu(In,Ga)(S,Se) 2 Dünnschichtsolarzellen*, **2005**.

[44] D. Briggs, P. Seah, *Practical Surface Analysis: Auger and X-ray photoelectron spectroscopy*, Wiley, **1990**.

[45] G. C. Smith, *Surface Analysis by Electron Spectroscopy: Measurement and Interpretation*, Springer US, **2013**.

[46] A. Benninghoven, F. G. Rüdenauer, H. W. Werner, *Secondary Ion Mass Spectrometry: Basic Concepts, Instrumental Aspects, Applications, and Trends*, J. Wiley, **1987**.

[47] R. G. Wilson, F. A. Stevie, C. W. Magee, *Secondary ion mass spectrometry: a practical handbook for depth profiling and bulk impurity analysis*, Wiley, **1989**.

[48] S. J. Fonash, *Solar cell device physics*, Academic Press, **1981**.

[49] M. Burgelman, J. Marlein, *Proceedings of the 23rd European Photovoltaic Solar Energy Conference* **2008**, 2151.

[50] J. Verschraegen, M. Burgelman, *Thin Solid Films* **2007**, *515*, 6276–6279.

[51] J. Pettersson, C. Platzer-Björkman, U. Zimmermann, M. Edoff, *Thin Solid Films* **2011**, *519*, 7476–7480.

[52] L. Assmann, J. C. Bernède, A. Drici, C. Amory, E. Halgand, M. Morsli, *Appl. Surf. Sci.* **2005**, *246*, 159–166.

[53] N. Kohara, S. Nishiwaki, Y. Hashimoto, T. Negami, T. Wada, *Sol. Energy Mater. Sol. Cells* **2001**, *67*, 209–215.

[54] R. Würz, D. Fuertes Marrón, A. Meeder, A. Rumberg, S. M. Babu, T. Schedel-Niedrig, U. Bloeck, P. Schubert-Bischoff, M. C. Lux-Steiner, *Thin Solid Films* **2003**, *431–432*, 398–402.

[55] Y. Cho, D.-W. Kim, S. Ahn, D. Nam, H. Cheong, G. Y. Jeong, J. Gwak, J. H. Yun, *Thin Solid Films* **2013**, *546*, 358–361.

[56] B. K. Meyer, A. Polity, B. Farangis, Y. He, D. Hasselkamp, T. Krämer, C. Wang, *Appl. Phys. Lett.* **2004**, *85*, 4929–4931.

[57] C. Platzer-Björkman, T. Törndahl, D. Abou-Ras, J. Malmström, J. Kessler, L. Stolt, *J. Appl. Phys.* **2006**, *100*, 044506.

[58] J. Pettersson, T. Torndahl, C. Platzer-Bjorkman, A. Hultqvist, M. Edoff, *IEEE J. Photovoltaics* **2013**, *3*, 1376–1382.

Chapter 4

Thermal Stability of CIGSSe with CdS and Zn(O,S) buffer layers

Cadmium sulfide (CdS) and Zinc oxysulfide (Zn(O,S)) are buffers that can be applied on $Cu(In,Ga)(S,Se)_2$ *(CIGSSe) absorbers to reach high efficiency thin film solar cells. In this chapter, the thermal stability of standard devices buffered by these materials were evaluated through a 1000 h 60 °C/105 °C thermal annealing. It was concluded that although no stability issues exist for all devices, Zn(O,S) buffered devices showed a transient relaxation of the I-V performance with a characteristic crossover effect and fill factor loss, which is recoverable by light soaking. A comparison of the rate of relaxation of the two temperatures leads to the conclusion that the relaxation effect is temperature driven, since the relaxation was slower at a lower temperature of 60 °C. As a further consequence of permanent chemical diffusion of elements, an accelerated relaxation of cell efficiency was observed post-thermal annealing (<1 day in dark storage). The* [S]/([S]+[O]) *ratio was speculated to contribute to this increased rate of cell efficiency relaxation.*

4.1. Introduction

Amongst the thin film solar cell technologies, the chalcopyrite family (CIS and CIGS) holds the current world record at 22.3% [1], and has a huge potential in replacing conventional first-generation silicon photovoltaic solar cells in renewable energies.

When well-encapsulated, CIGS systems with CdS buffer have shown resilience in outdoor stability studies that were conducted for a maximum of 20 years [2]. It is important to note that CIGS modules that experience dark storage at high temperatures consequentially face a drop of up to 20% efficiency, but this can be rectified by light soaking the module. These so-called metastable effects, i.e. reversible photovoltaic characteristic change, result in the requirement of an impractical pre-conditioning [3]. Since the effects of long term storage and its mechanisms in alternative buffer layers have not been as thoroughly evaluated, an initial thermal stability test was performed on unencapsulated CIGSSe devices prepared with standard CBD-CdS buffer and alternative CBD-Zn(O,S) buffer layers. The results are summarized in this chapter.

Before the commencement of the long-term elevated dark thermal test, the material properties of the CIGSSe/buffer interface were evaluated by preparing FIB cuts and examining the cross-section images of the devices under HR-TEM, as shown in Figure 4.1. The devices' chemical composition was acquired by EDX scans at the buffer and the CIGSSe interface and summarized in Table 4.1.

From the TEM images taken with a 200 nm scale, it was observed that distinct buffer layers separating the absorber and window for the CBD technique. At the spot where the buffer was surveyed, there was a notable out-diffusion of copper for all buffers. There was also some degree of oxygen incorporation in the buffer layer, for the CBD processes due to the abundance of oxygen and hydroxide species during the deposition.

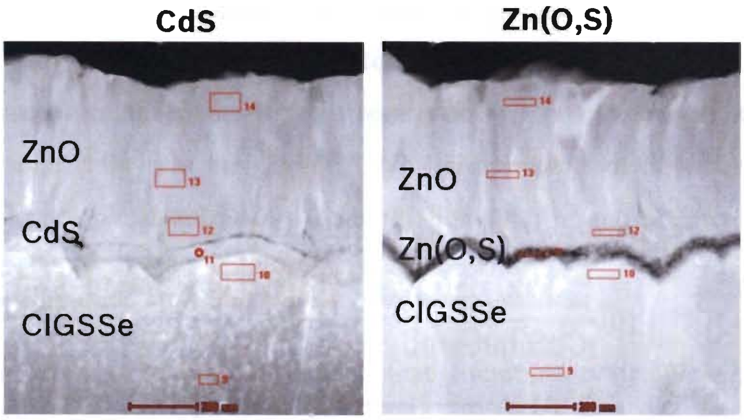

Figure 4.1 FIB-TEM of $Cu(In,Ga)(S,Se)_2$ devices with CdS and alternative Zn(O,S) buffers as determined by TEM-EDX.

Table 4.1 Chemical composition of $Cu(In,Ga)(S,Se)_2$ devices with CdS and alternative Zn(O,S) buffers as determined by TEM-EDX.

			Atomic Ratio by EDX (%)						
	Layer	Area	Cu	Ga	In	S	Se	Zn	O
CBD-CdS	CIGSSe	10	23.7		20.4	11.8	44.0		
	Buffer	11	3.6			52.4		14.5	29.5
CBD-Zn(O,S)	CIGSSe	10	28.1	0.8	18.8		52.3		
	Buffer	11	2.2		2.5	9.4	2.8	39.3	43.8

Considering the EDX technique's accuracy limit of ±5%, the amount of gallium, determined to be in the range of 2-5 atomic % by XRF [4], might not be accounted for accurately in Table 4.1. Therefore, the accuracy of the chemical composition was verified by performing TOF-SIMS on the same devices in positive mode, as shown in Figure 4.2. In contrast to the localized spots surveyed by TEM-EDX, a profile of the device from the window through the buffer and absorber was obtained and plotted. Clearly, the distribution and relative ratios of key elements in the absorber (copper, indium, and gallium), the buffer (cadmium or zinc), and the window (aluminum and zinc) did not vary significantly for the two devices. This indicates that any modification mainly came from the different buffer deposited. With this understanding of the materials properties, the 1000 h thermal ageing tests were performed. The results of these thermal ageing tests and consequences are discussed in the next sections.

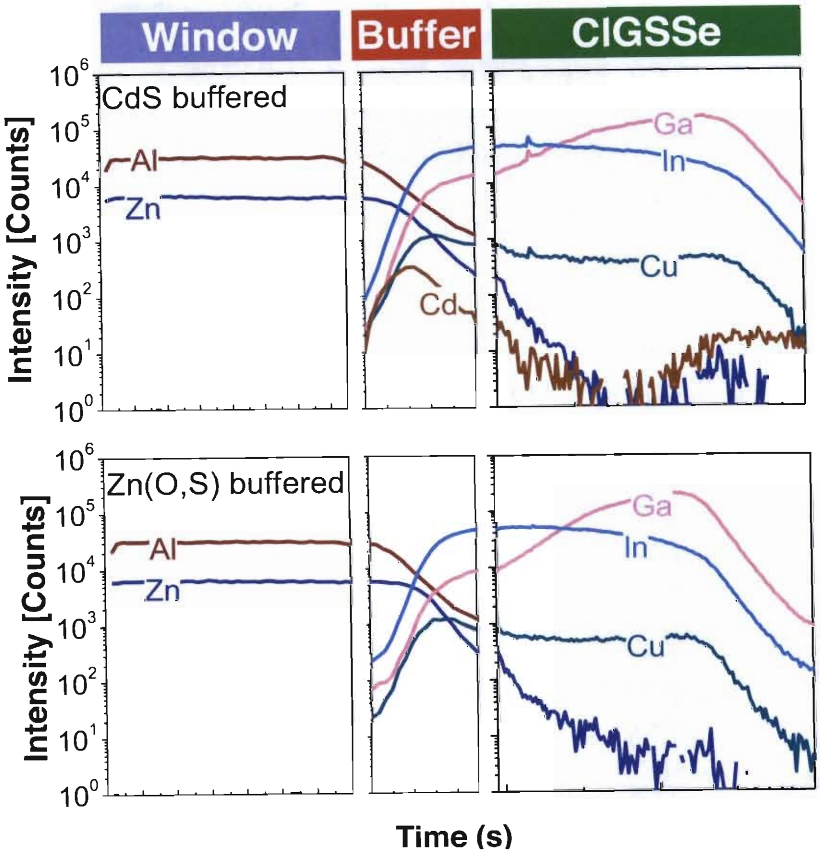

Figure 4.2 Chemical composition of Cu(In,Ga)(S,Se)$_2$ devices with CdS and Zn(O,S) buffers as determined by TOF-SIMS.

4.2. Dry heat (DrH) test at 60 °C/105 °C Dark Thermal Storage, 1000 h

As with conventional CIGS solar cells in the field, it was necessary to establish a benchmark of the performance of the sputtered CIGSSe solar cells with conventional and alternative buffer layers. An accelerated lifetime test at elevated temperature was necessary to establish an understanding of fluctuation and/or degradation in cell efficiencies over time.

In this PhD thesis, a standard testing protocol was developed by documenting the I-V parameters of solar cells a) at their initial, 24 h light soaked state, b) after heating solar cells on covered hot plates set at 60 °C/105 °C for 1000 h, and c) after a second light soaking for 24 h. This was to

(1) Simulate a dark storage environment that literature typically claimed induced metastability [5]
(2) Establish a link between temperature and rate of cell efficiency loss, if any.

Samples fabricated on the same absorber with standard CBD-CdS [6] or CBD-Zn(O,S) [7] buffer layers were selected for the dry heat (DrH) test. In Figure 4.3, the average and standard deviation derived from 4–5 cells were plotted at 1) start of the experiment, 0 h, 2) after 1000 h of DrH at 60 °C/105 °C, and 3) after a subsequent light soaking (LS) recovery of 24 h.

For all CdS-buffered devices, regardless of temperature applied, cell efficiencies remained approximately constant throughout the three points where I-V parameter was recorded. On the other hand, Zn(O,S)-buffered devices showed a drop of cell efficiencies of –29% (1000 h DrH at 60 °C) and –57% (1000 h DrH at 105 °C), which were recoverable after 24 h LS.

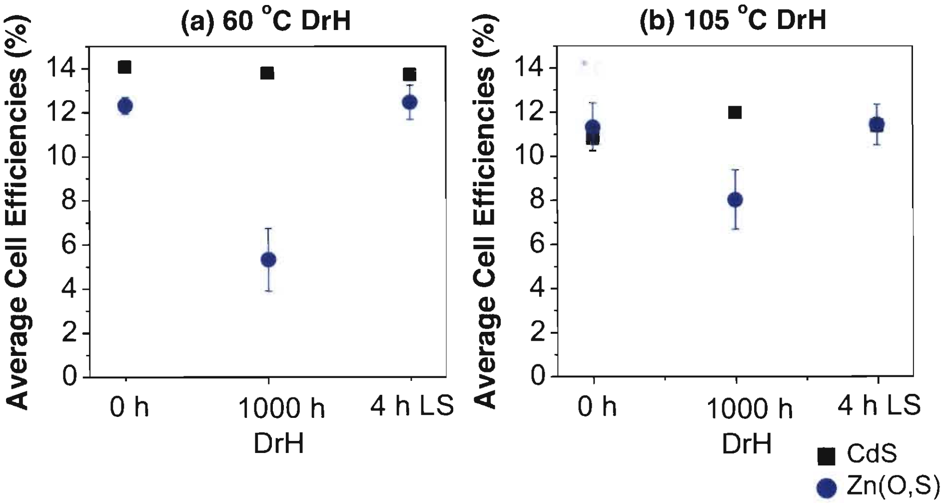

Figure 4.3 Average cell efficiencies (1) 0 h, (2) 1000 h DrH Test at 60 °C/105 °C, and (c) 24 h LS for CIGSSe solar cells buffered with (a) CdS and Zn(O,S) at 60 °C, and (b) CdS and Zn(O,S) at 105 °C.

The corresponding I-V curves for Figure 4.3 were plotted with a selected CdS/Zn(O,S) device heated at 60 °C/105 °C in Figure 4.4. V_{OC}, J_{SC}, FF, and cell efficiency values for each I-V curve were tabulated in Table 4.2. A representation of average cell efficiency values, these values were plotted at 1) start of the experiment, 0 h, 2) after 1000 h of DrH at 60 °C/105 °C, and 3) after a subsequent light soaking (LS) recovery of 24 h.

Once again, the I-V plots in Figure 4.4. (a) and (c) proved minimum changes occurred in the CdS devices during the dry heat test at 60 °C/105 °C and subsequent LS. On the other hand, the plots for the Zn(O,S) devices in Figure 4.4 (b) and (d) showed different extents of formation of a barrier at the 4th quadrant of the I-V curve post 1000 h DrH test, with the condition of 105 °C showing a larger barrier than 60 °C. It was observed for both cases that there was almost full recovery from the relaxed state after 1000 h dark storage at 60 °C to its original efficiency after 24 h LS.

From the shape of the I-V plots for the Zn(O,S) devices, it is possible to conclude that *FF* and R_S are the main factors influenced during these dark storage tests at elevated temperatures. The different extents of *FF* loss in the device heated at 60 °C versus the one heated at 105 °C are further evidences that this transient loss of efficiency is temperature dependent. On the other hand, V_{OC}, another parameter which has metastable effects reported elsewhere [5], was observed to be generally stable in the devices tested. These two evidences allowed one to speculate that the mechanism for barrier formation was interface-related, rather than absorber-dependent.

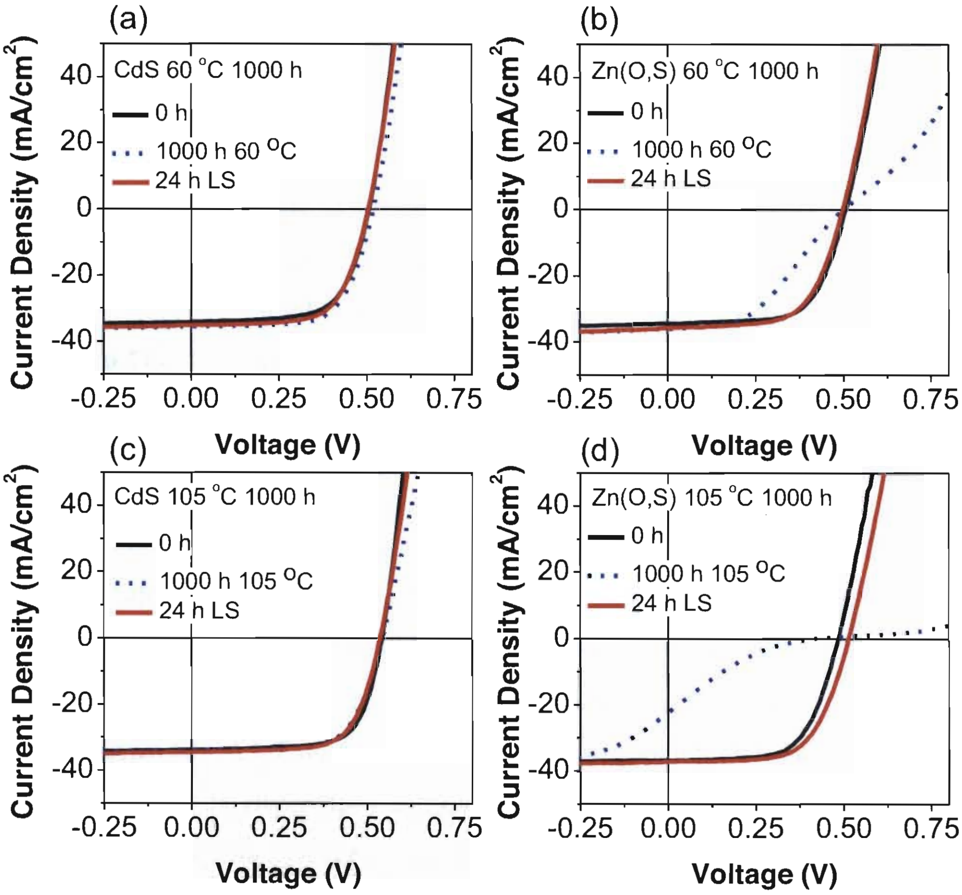

Figure 4.4 I-V curves at (1) 0 h, (2) 1000 h DrH Test at 60 °C/105 °C, and (3) 24 h LS for (a) CdS at 60 °C, (b) alternative Zn(O,S) buffer at 60 °C, (c) CdS at 105 °C, and (d) Zn(O,S) at 105 °C.

Table 4.2 Summary of I-V parameters at (1) 0 h, (2) 1000 h DrH Test at 60 °C or 105 °C, and (c) 4 h LS, for CdS and Zn(O,S) buffers with CIGSSe absorber.

	Time (h)	V_{OC} **(V)**	J_{SC} **(mA/cm^2)**	***FF*** **(%)**	**η (%)**
CBD-CdS	0	0.51	**32.1**	70.6	11.5
	1000 (60 °C)	0.52	**35.4**	67.2	12.4
	24 (LS)	0.51	**35.2**	65.7	11.8
CBD-Zn(O,S)	0	0.51	**34.4**	65.3	11.4
	1000 (60 °C)	0.50	**36.0**	43.2	7.8
	24 (LS)	0.50	**35.8**	62.6	11.2
CBD-CdS	0	0.54	**35.7**	70.1	13.6
	1000 (105 °C)	0.55	**36.8**	66.7	13.4
	4 (LS)	0.54	**36.9**	68.8	13.7
CBD-Zn(O,S)	0	0.50	**37.9**	65.4	**12.0**
	1000 (105 °C)	0.20	**12.6**	20.8	**0.5**
	4 (LS)	0.54	**38.6**	53.4	**11.0**

In order to quantify the electrical behavior of devices, the C-V profiles of the devices were measured to profile any carrier concentration changes in the SCR at the relaxed and light soaked states of the devices. The devices surveyed in the 105 °C DrH test were selected as their I-V curves showed more visible changes at their relaxed states and after light soaking in Table 4.4. Based on the technique discussed in Section 3.2.3., the carrier concentrations were derived for these devices by performing measurements at 1000 Hz, where carriers and electrically active traps in the SCR respond ($N_{\mathrm{A}}+N_{\mathrm{t}}$), and at 100,000 Hz, after the inflection point where only carriers respond (N_{A}).

The responses of the relaxed devices to light soaking differed. First, there were negligible changes in carrier concentrations for CBD-CdS buffered devices at 1000 Hz and 100,000 Hz. This indicated that the carriers and traps within the SCR of the CdS/CIGSSe device did not change significantly. This was supported by the I-V curves which showed negligible changes as well. The third observation was that the CBD-Zn(O,S) device showed a two-order increase in magnitude at 1000 Hz and 100,000 Hz, which implied that it was not the quantity of traps but carriers in the SCR that contribute to this increase. This indicates that the redistribution of carrier charges in the SCR contributes to the *FF* loss coming from the transport barrier, similar to the p+ model proposed by Igalson [8].

Table 4.3 Summary of Carrier Concentrations at (1) 1000 Hz (N_A+N_t) and (2) 100,000 Hz (N_A) before and after LS for devices made with CdS and Zn(O,S) buffers.

		Carrier Concentration (cm^{-3})	
	ac frequency (Hz)	Relaxed	Light Soaked
CBD-CdS	1000	1.0E17	2.2E17
	100,000	9.2E15	2E16
CBD-Zn(O,S)	1000	2.8E18	5.6E20
	100,000	8.7E15	5.5E17

4.3. Acceleration of Relaxation in Standard CBD-Zn(O,S) Devices

The long-term effect of thermal ageing on metastability was investigated for CIGSSe/Zn(O,S) thin-film solar cells. Unencapsulated devices prepared with Zn(O,S) buffers deposited with the CBD process developed by Ennaoui *et al.* [7] were investigated for device stability by applying external thermal stress of 105 °C over 1000 h on six solar cells on six solar cells from three different batches of absorbers with varying sulfur content at their surfaces. There are no bandgap differences in the absorbers based on EQE measurements. Three control device of the same compositions as the thermally heated devices were stored under N_2 at 25 °C for the same period of time. Cell efficiencies were recorded before the test and at several intervals after the test: (1) after 1000 h, (2) after 4 h light soaking recovery, (3) after 2 days dark storage, (4) after a second light soaking recovery of 4 h. The solar simulator was also calibrated to AM1.5G condition for the light soaking step.

All three batches of Zn(O,S) devices showed the same trend of accelerated relaxation after 1000 h thermal ageing. A representative measurement with control and aged devices was selected for the results presented in the discussion. Figure 4.5(a) shows that the device aged at 105 °C for 1000 h had much lower cell efficiencies and exhibits the characteristic S-shaped kink in its I-V curves (Fig 4.5 (b), red dashed curves). The control device stored at 25 °C N_2 retained almost full efficiency for the same duration. Light soaking recovery to initial post-fabrication efficiencies was possible for both devices, which confirmed that the drop in efficiencies was not permanent degradation.

A second dark storage test at 25 °C in ambient condition was performed immediately after the light soaking recovery. Significantly, the two days' dark storage showed almost 50% cell efficiency relaxation for the thermally aged device, whereas there was negligible change for the recovered control device. It should be mentioned that an additional control device which was stored under 25 °C (atm.) in a separate experiment (i.e. exposed to moisture) for approximately three months also experienced significant relaxation of cell efficiencies (results are not discussed here).

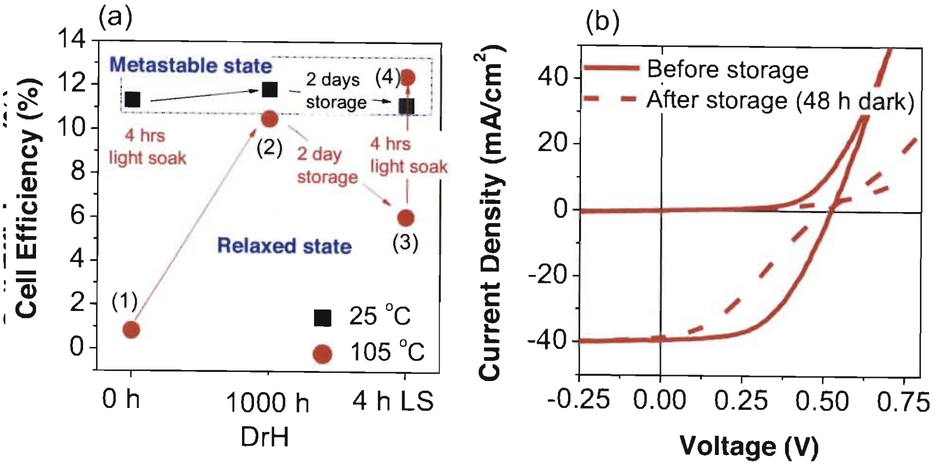

Figure 4.5 (a) Evolution of cell efficiency (1) Post 1000 h thermal ageing (2) subsequent light soaking recovery for 4 hours (3) after 2 days dark storage in ambient condition (4) subsequent light soaking recovery for 4 hours (b) Evolution of I-V curves for aged device (stored at 105 °C for 1000 h) before and after room temperature storage.

The relaxation process for a thermally aged device (Figure 4.5(b), red dashed curves) mainly affected the *FF*. The "S-shaped" kink that was introduced during the 105 °C heating appeared once again during the dark storage at 25 °C ambient post light-soaking recovery. It is conjectured that the root cause that leads to relaxation after the first dark storage (105 °C) and the second dark storage after recovery (25 °C) might be the same due to the nature of the I-V curve shape. However, as the aged device relaxed more quickly than the non-aged device, it suggested a permanent chemical diffusion which accelerated the relaxation phenomenon.

In order to confirm the possibility of chemical diffusion leading to a change in the *p-n* junction, depth-profiling XPS measurements were performed for as-received and aged bilayers of the same CIGSSe/Zn(O,S) compositions, without the window layer and Al/Ni grids. Figure 4.6(a) shows the elemental distribution of the Zn(O,S) layer under as-received condition (thin lines), and after thermal ageing at 105 °C for 20 days (thick lines). XPS profiling showed that zinc and sulfur out-diffusion from the CIGSSe absorber into the bulk of the Zn(O,S) buffer were apparent after long-term heating at elevated temperatures.

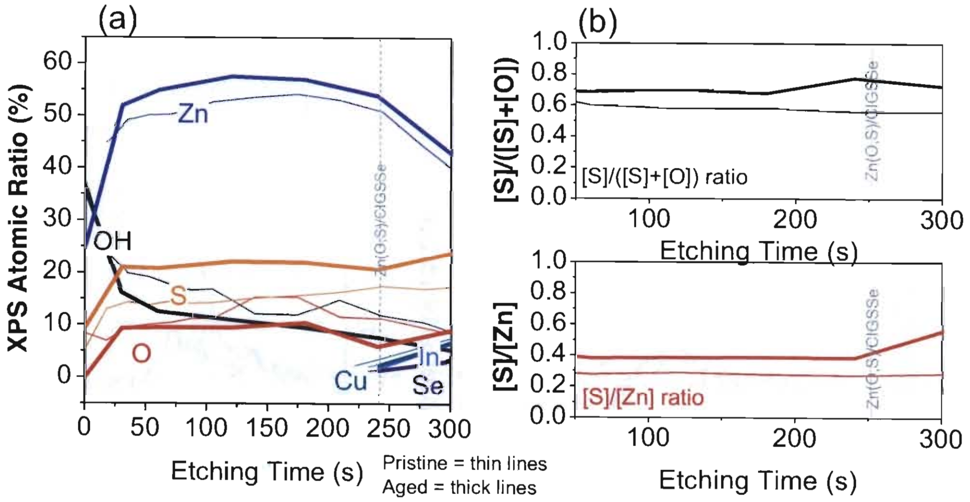

Figure 4.6 (a) Overview of element distribution for the pristine bilayer (thin lines) and the aged bilayer (thick lines) (b) [S]/([S]+[O]) ratios before (solid line) and after thermal ageing (dotted line) and [S]/[Zn] ratios before (solid line) and after thermal ageing (dotted line).

The ratios of [S]/([S]+[O]) and [S]/[Zn] were plotted in Figure 4.6(b) for comparison. The increase in sulfur in the buffer led to a visible increment of [S]/([S]+[O]) and [S]/[Zn] ratios after thermal ageing. This implied that the amount of sulfur available for zinc sulfide formation is increased. As discussed in Section 4.3., these results further validated that $E_g^{Zn(O,S)}$ increase and formation of acceptor states in the buffer could possibly accelerate metastability at room temperature.

In order to understand the electronic band alignment of the CIGSSe/Zn(O,S) bilayer, the valence band maximum (VBM) value at the Zn(O,S) bulk and the CIGSSe bulk were derived from extrapolation of the values at the band edge of the XPS spectra. This was done after alignment of the signals to the Indium 3d peak, which was unchanged before and after the thermal ageing experiment. The changes before and after heating were $E_V^{Zn(O,S)} = -2.00$ eV to -1.85 eV and $E_V^{CIGSSe} = -0.53$ eV to -0.43 eV (Figure 4.10). Since the VBM after thermal ageing remained relatively unchanged as compared to before the initial state, any changes in the chemical composition might then be deemed to affect $E_g^{Zn(O,S)}$ and thus $\Delta E_C^{CIGSSe/Zn(O,S)}$ [9, 10].

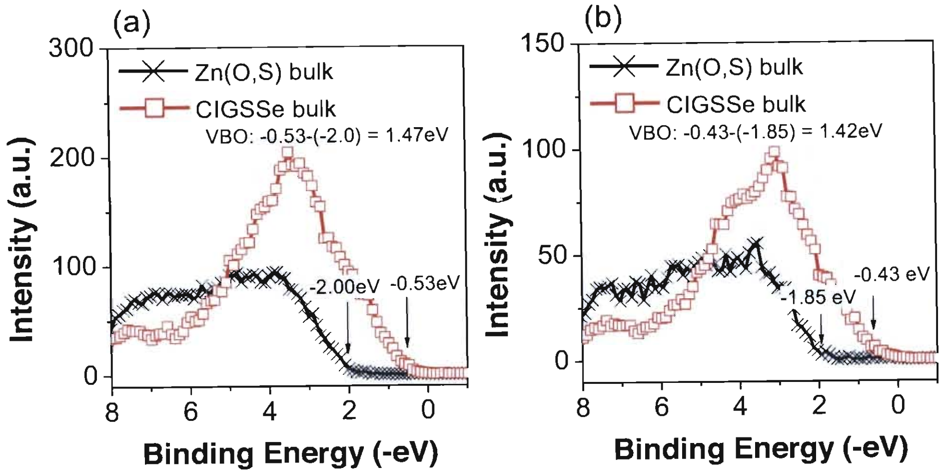

Figure 4.7 Determination of VBM of absorber and buffer and CBO for (a) pristine and (b) thermally aged bilayers.

A band diagram was plotted in Figure 4.8 based on XPS data. The absorber band gap was determined by external quantum efficiency measurements, and found to be approximately 1.0 eV. The buffer bulk band gap was determined from the behavior of Zn(O,S) at different [O]:[S] ratios [11, 12]. Calculated ratios for [S]/([S]+[O]) in Zn(O,S) were 0.6 before ageing and 0.8 after ageing, corresponding to a band gap of 2.6 eV and 2.9 eV, respectively. As a result, the $\Delta E_C^{CIGSSe/Zn(O,S)}$ was expected to be higher during the "relaxed" state (low efficiency), leading to worsening charge transport across the buffer.

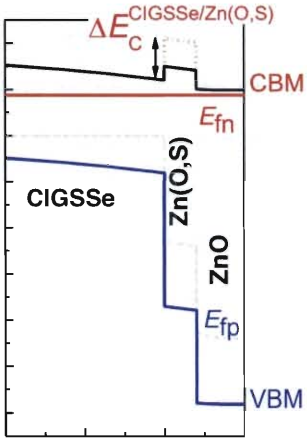

Figure 4.8 Proposed band diagrams of Zn(O,S)-buffered CIGSSe device with and without thermal ageing. $\Delta E_C^{CIGSSe/Zn(O,S)}$ increased after thermal ageing.

During this investigation on the effects of 105 °C thermal ageing over 1000 h on metastability, an acceleration of cell efficiency relaxation was found for CIGSSe/Zn(O,S) thin-film solar cells. XPS analyses revealed that after thermal ageing, the [S]/([S]+[O]) ratio generally increased, implying a widened band gap and increased CBO at the CIGSSe/Zn(O,S) interface. Additionally, the increase of [S]/[Zn] ratio leads to more V_{Zn} or S_i acceptor defects in the buffer bulk. The correlation of the element distribution with the amount of acceptor defects in the buffer, which affect the band alignment between CIGSSe and Zn(O,S) and its implication on accelerated relaxation after thermal ageing was also hypothesized.

4.4. Concluding Remarks from Thermal Ageing Tests

In the dark storage experiments at elevated temperatures, it was verified that there was thermal stability of $Cu(In,Ga)(S,Se)_2$ devices made with CdS and alternative buffer layers. Since CdS and Zn(O,S) buffers yield relatively high efficiencies, and are cheaper from a cost perspective, the Zn(O,S) buffer is a viable alternative for toxic CdS. However, it was observed that there was unstable output in the form of *FF* loss of the Zn(O,S) buffered cell following a period of dark storage that required conditioning (light soaking) before the maximum output of the cells can be reached again. This temporary loss of output is undesirable. An understanding of the responses of different stoichiometries of Zn(O,S) has been established by quantifying the chemical distribution with XPS at each step with depth-profiling. It was observed that higher sulfur contents in the Zn(O,S), formed by applying a different fabrication method during the CBD process, or caused by long-term sulfur out-diffusion from absorber to buffer, led to accelerated relaxation of efficiencies at dark storage at room temperature. In order to address the origin of the *FF* loss and appearance of a kink in the I-V curve during relaxation of cell efficiency, possible reasons suggested in this chapter will be validated by SCAPS-1D simulation, and experiments showing a change in charge separation at the CIGSSe/Zn(O,S) heterojunction will be demonstrated in the following chapter.

References

[1] http://www.solar-frontier.com/eng/news/2015/C051171.html, **2015**.

[2] J. A. del Cueto, S. Rummel, B. Kroposki, C. Osterwald, A. Anderberg, in *Photovoltaic Specialists Conference, 2008. PVSC '08. 33rd IEEE*, **2008**, pp. 1–6.

[3] K. Kushiya, S. Kuriyagawa, K. Tazawa, T. Okazawa, M. Tsunoda, in *Conference Record of the 2006 IEEE 4th World Conference on Photovoltaic Energy Conversion, Vol. 1*, **2006**, pp. 348–351.

[4] V. Probst, I. Koetschau, E. Novak, A. Jasenek, H. Eschrich, F. Hergert, T. Hahn, J. Feichtinger, M. Maier, B. Walther, V. Nadenau, *IEEE J. Photovoltaics* **2014**, *4*, 687-692.

[5] M. N. Ruberto, A. Rothwarf, *J. Appl. Phys.* **1987**, *61*, 4662–4669.

[6] J. Kessler, K. O. Velthaus, M. Ruckh, R. Laichinger, H. W. Schock, D. Lincot, *6th International Photovoltaic Science and Engineering Conference: Proceedings* **1992**.

[7] A. Ennaoui, M. Bär, J. Klaer, T. Kropp, R. Sáez-Araoz, M. C. Lux-Steiner, *Prog. Photovoltaics Res. Appl.* **2006**, *14*, 499–511.

[8] M. Igalson, A. Urbaniak, P. Zabierowski, H. A. Maksoud, M. Buffiere, N. Barreau, S. Spiering, *Thin Solid Films* **2013**, *535*, 302–306.

[9] T. Adler, M. Botros, W. Witte, D. Hariskos, R. Menner, M. Powalla, A. Klein, *Phys. Status Solidi A* **2014**, *211*, 1972–1980.

[10] C. Platzer-Björkman, T. Törndahl, D. Abou-Ras, J. Malmström, J. Kessler, L. Stolt, *J. Appl. Phys.* **2006**, *100*, 044506.

[11] B. K. Meyer, A. Polity, B. Farangis, Y. He, D. Hasselkamp, T. Krämer, C. Wang, *Appl. Phys. Lett.* **2004**, *85*, 4929–4931.

[12] C. Platzer-Björkman, J. Lu, J. Kessler, L. Stolt, *Thin Solid Films* **2003**, *431–432*, 321–325.

Chapter 5

Origin of Metastability in Cu(In,Ga)(S,Se)$_2$/Zn(O,S) Solar Cells

Zinc oxysulfide buffer layers with [O]:[S] of 1:0. 6:1, 4:1, 2:1, and 1:1 ratios were deposited by atomic layer deposition on Cu(In,Ga)(S,Se)2 absorbers and finished to solar cells. We demonstrate using Time-Resolved Photoluminescence that the minority carrier lifetime of Zn(O,S) buffered solar cells is dependent on the sulfur content of the buffer layer. τ_1 *for devices with [O]:[S] of 1:0–4:1 are <10 ns, indicating efficient charge separation in devices with low sulfur content. An additional* τ_2 *was observed for relaxed devices with [O]:[S] of 2:1 and both relaxed and light soaked devices with [O]:[S] of 1:1. Corroborated with one-dimensional electronic band structure simulation results, this additional decay lifetime was attributed to radiative recombination in the absorber due to excessive acceptor-type defects in sulfur-rich Zn(O,S) buffer layer that causes a buildup in interface-barrier for charge transport. A light soaking step shortens the carrier lifetime for the moderately sulfur-rich 2:1 device when excess acceptors are passivated in the buffer, reducing the crossover in the dark and illuminated I-V curves. However, when a high concentration of excess acceptors exists in the buffer and cannot be passivated by light soaking, as with the sulfur-rich 1:1 device, then cell efficiency of the device will remain low.*

5.1. Introduction

Zinc oxysulfide (Zn(O,S), $E_g = 3.0–3.6$ eV) is increasingly replacing cadmium sulfide (CdS, $E_g = 2.4$ eV) as a buffer layer for $Cu(In,Ga)(S,Se)_2$ (CIGSSe) devices, due to environmental concerns with cadmium and potential for higher current density for wider bandgap Zn(O,S) [1]. A metastable solar cell experiences a drop in cell efficiency during dark storage as shown by 1) a crossover of the dark and illuminated I-V curves and 2) fill factor (*FF*) loss accompanied by a kink in the illuminated I-V curve [2-4]. Although charge transport issues arise with Zn(O,S) buffered devices during prolonged dark storage [3, 5-7], this can be mitigated by a light soaking step. This efficiency loss has been suggested to originate from the [O]:[S] ratio of Zn(O,S) which alters the buffer bandgap [8] and conduction band offset (CBO) between the Zn(O,S)/CIGSSe interface [9]. Whereas sulfur-poor Zn(O,S) tends to form oxygen (V_O) or sulfur vacancies (V_S), which are donor states, sulfur-rich Zn(O,S) buffer tends to have a higher concentration of zinc vacancies (V_{Zn}) or sulfur interstitials (S_i), which leads to acceptor states in the bulk of the buffer layer [10]. This increase in acceptors have been modelled by SCAPS-1D [11] simulation to influence the electric field strength of the *p-n* heterojunction. In this chapter, it was demonstrated that atomic layer deposition (ALD) Zn(O,S) buffered solar cells with increasing sulfur content showed increased metastability. This is resulted from the reduction of charge separation strength and increasing recombination in sulfur-rich devices, as supported by an investigation on charge carrier recombination kinetics using Time Resolved Photoluminescence (TRPL). This experimental observation is validated with SCAPS-1D simulation [11], in order to explain a likely mechanism of metastability in CIGSSe devices that is most apparent with sulfur-rich Zn(O,S).

The present chapter is organized as follows. In the subsequent sections, SCAPS-1D simulation is first performed to understand the possible contribution to *FF* loss that manifests in Zn(O,S)-buffered CIGSSe devices when they undergo long term storage tests (Figure 5.1). Different models are proposed to determine which one fits to experimental observations in Zn(O,S) buffered devices in Chapter 4. Subsequently, TRPL is employed to experimentally support the simulation results. This is systematically done on both sulfur-poor and sulfur-rich Zn(O,S) buffers to distinguish the difference of the extents of their metastability. Finally, devices with and without metastabilities are discussed and the best device with low metastability and high cell efficiency is selected.

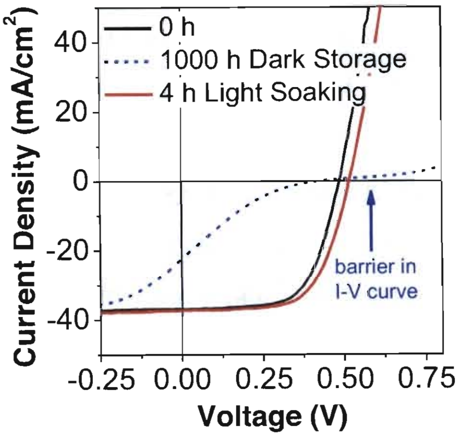

Figure 5.1 Typical Zn(O,S)/CIGSSe Solar Cell that undergoes transient dark storage relaxation.

5.2. SCAPS-1D Simulation Parameters and Proposed Models for *FF* Loss

Experimental data was supported with the one-dimensional simulator SCAPS, developed by Decock *et al.* at the University of Gent [12]. This simulator is based on continuity equations for electrons and holes, and the principles of the Poisson equation. Numerical solutions are solved mathematically based on these algorithms. The basic parameters for a simplified CIGSSe solar cell is listed in Table 5.1. A thin Ordered Vacancy Compound (OVC) of 15 nm is assumed between the absorber and buffer assuming *n*-type inversion at the interface [13]. The absorption parameter of the Zn(O,S) was based on a standard ZnS absorption file. Changing properties in the buffer leading to *FF* loss are discussed in the following models.

Model A: Conduction Band Offset (CBO) between absorber/buffer

Sharbati *et al.* considered band variations of the CIGS and the Zn(O,S) as parameters to create an ideal CBO matching between the absorber and buffer [14]. The band gap of CIGS with respect to the quantity of Ga (with the values of Ga = x and In = $1 - x$) is governed by the following equation

$$E_g(x) = 1.01 + 0.42x + 0.24x^2 \tag{5.1}$$

The range of band gaps vary from $E_g^{CuInSe_2}$ = 1.01 eV to $E_g^{CuGaSe_2}$ = 1.67 eV. Consequentially, the electron affinity decreases from 4.35 to 3.69 eV, following a slight downward bowing in the conduction band [15].

It has been separately evaluated by Meyer, Bär, and Platzer-Björkman that there was a compositional dependence of the oxygen and sulfur of Zn(O,S) on the valence band maximum (VBM), conduction band minimum (CBM), and the band gap of the material [16-18]. For Zn(O,S) the band gap follows the bowing parameter with respect to oxygen (with values of S = x and O = $1 - x$) as

$$E_g(x) = 3.6 - 0.4x - 3x(1 - x) \tag{5.2}$$

where E_g^{ZnS} = 3.6 eV and E_g^{ZnO} = 3.2 eV, with a bowing parameter which levelled out where the sulfur and oxygen are of the same ratio.

With these variations, it is possible for $\Delta E_C^{CIGSSe/Zn(O,S)}$ to range from – 0.7 eV to + 1.3 eV. A large positive CBO results in a spike barrier between absorber and buffer, impeding the current flow in the forward bias and blocking the photocurrent.

From experimental and theoretical calculations, it was suggested that a moderate spike in the $\Delta E_C^{CIGSSe/Zn(O,S)}$ (0.3–0.4 eV) was optimal and does not deteriorate the current collection. However, a $\Delta E_C^{CIGSSe/Zn(O,S)}$ exceeding +0.4 eV leads to an electronic barrier in the illuminated I-V curve and *FF* loss [9].

Model B. Electron mobility in buffer

It is known that the electron Hall mobility of ZnS (140–230 cm^2/Vs) and ZnO (125 cm^2/Vs) measured at 300 K are different [19]. Furthermore, considering that sphalerite and wurtzite ZnS also exhibit vastly different electron/hole effective masses and electron/hole mobilities

(Table 5.1) [20-28], this has to be accounted for when the [O]:[S] ratio in Zn(O,S) is tuned. Since Zn(O,S) is expected to be *n*-type and electrons travel through the Zn(O,S) and ZnO window to be collected at the Al/Ni grid during normal solar cell operation, the impact of changing electron mobility has on the transport of electrons across this interface.

The increase in resistivity of the material leading to reduced electron mobilities is expected to reduce the series resistance of the device. Consequently, the *FF* is reduced as well.

Table 5.1 m_e^*/m_0: Electron effective mass; m_h^*/m_0: hole effective mass; and $\mu_{e,h}$: electron or hole mobility in ZnO, ZnS (Sphalerite), and ZnS (Wurtzite).

	Electron Effective Mass m_e^*/m_0	**Hole Effective Mass m_h^*/m_0**	**Electron Mobility μ_e (cm^2/Vs)**	**Hole Mobility μ_h (cm^2/Vs)**
ZnO	0.27	–	125	–
ZnS (Sphalerite)	0.34–0.39	0.58	160–230	10
ZnS (Wurtzite)	0.27–0.28	Heavy hole: 1–1.4 Light hole: 0.49–0.51	140	5

Model C. Dipole between absorber/buffer

A dipole at the absorber/buffer interface could occur when excess charges accumulate at this interface and disrupt the electric field of the *p*-*n* junction. In order to simulate an interface dipole between the absorber and buffer, a layer of acceptors and a layer of donors are placed in between the absorber and buffer, with the same density of acceptor/donor in the respective layer to create a polarization effect in the electric field. Concurrent increase of acceptor/donor densities at the same magnitude increases the charge accumulation at this interface and produces a spike at the absorber/buffer interface, indirectly altering the CBO. This is expected to reduce *FF* in the solar cell.

Model D. Deep acceptors in the Zn(O,S) layer

Several defects in the ZnS material should be analyzed in their contribution towards recombination and band alignment, as illustrated in Figure 5.2. A Zn-rich stoichiometry creates more Zn^{2+} ions and fewer S^{2-} ions resulting in predominantly sulfur vacancies (V_{S}) and zinc interstitials (Zn_i) which form donor-vacancy complexes termed as “A-centers” [29-33] close to the conduction band. These donors have demonstrated self-compensation in Zn-rich ZnS. When one transits from a Zn-rich to S-rich stoichiometry, the amount of zinc vacancies (V_{Zn}) and sulfur interstitials (S_i) predominates [34], and these defects act as acceptors with defect levels close to the valence band, and the material becomes more *p*-type [10]. Importantly, growth at a large zinc vapor pressure favors the formation of V_{Zn}'' and Zn_i, whereas growth at high sulfur vapor pressure favors V_{Zn}' and $\mathrm{Zn}_i^{\cdot\cdot}$ [35].

One further isoelectronic defect that should be considered is the substitutional oxygen-on-sulfur lattice site (O_S), which is an impurity that inevitably gets formed especially when there is a sulfur deficiency, since both oxygen and sulfur have the same valance. Since it is hard to prevent the formation of electronic defects in the energy band gap of these II-VI semiconductors [36], it is then necessary to consider their interactions with respect to the band alignment with CIGSSe.

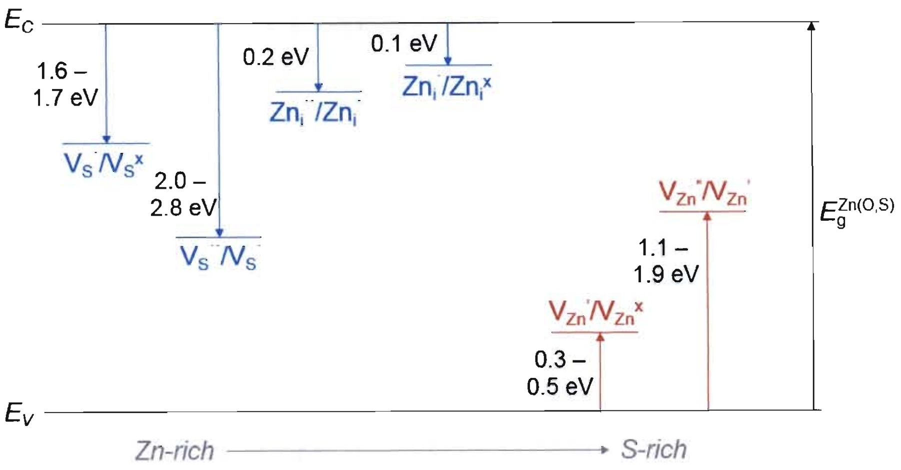

Figure 5.2 Energy levels of deep V_{Zn} acceptors, shallow Zn_i donors, and deep V_S donor states with different charges and energy level.

Extensive modelling studies have been performed to probe the effects of the "red kink" effect, where photocurrent is severely impeded when a red-light (< 2 eV band gap) is illuminated on a device while evaluating its I-V characteristics under forward bias [37]. Under these conditions, the photogenerated current is produced by the absorber as the energy provided by the illumination does not cover the range up to the buffer's band gap. Nichterwitz *et al.* proposed the origin of the red kink as deep acceptors in the buffer at the CdS/ZnO interface with extensive numerical modelling and electron-beam induced current (EBIC) experiments [37]. While the contribution of deep acceptors in the buffer towards the red kink is under debate, it can be ascertained that *n*-type CdS or ZnS buffers forms donor-vacancy complexes whereas sulfur-rich ZnS buffer have the tendency to switch to *p*-type [10] and have a much higher density of V_{Zn} acceptors. With this consideration, a Zn-rich, highly compensated and low acceptor density case and a S-rich, high acceptor density case can be assumed and modelled to understand the extent that these acceptor states contribute to the *FF* loss.

With these four possibilities discussed above, the properties of the Zn(O,S) buffer are modelled separately. The effects of changing CBO, e^- mobility, addition of a dipole, and deep acceptors in the buffer with and without a CBO are summarized in Table 5.2.

Table 5.2 Parameters of a standard CIGSSe/Zn(O,S) device utilized in SCAPS-1D simulations; χ_e: electron affinity; $\mu_{e,h}$: electron or hole mobility; N_d: shallow *n*-type doping density; N_a: shallow *p*-type doping density; N_t: defect density; E_t: defect energy; $\sigma_{e,h}$: capture cross section for electrons or holes; $\tau_{e,h}$: lifetime of electrons and holes.

Varied Parameters in Zn(O,S)	
A: Conduction Band Offset	χ_e = 4.1–4.5 eV, CBO = 0.0–0.4 eV
B: e$^-$ mobility	$\mu_e = 5 \text{ x } 10^{-5} - 5 \text{ x } 10^{-6}$ cm^2/Vs
C: Dipole	$N_d/N_a = 5 \text{ x } 10^{17} - 5 \text{ x } 10^{18}$
D1: Deep Acceptors, CBO	χ_e = 4.375 eV, E_t = 1.0 eV above VB
D2: Deep Acceptors, no CBO	χ_e = 4.5 eV, E_t = 1.0 eV above VB

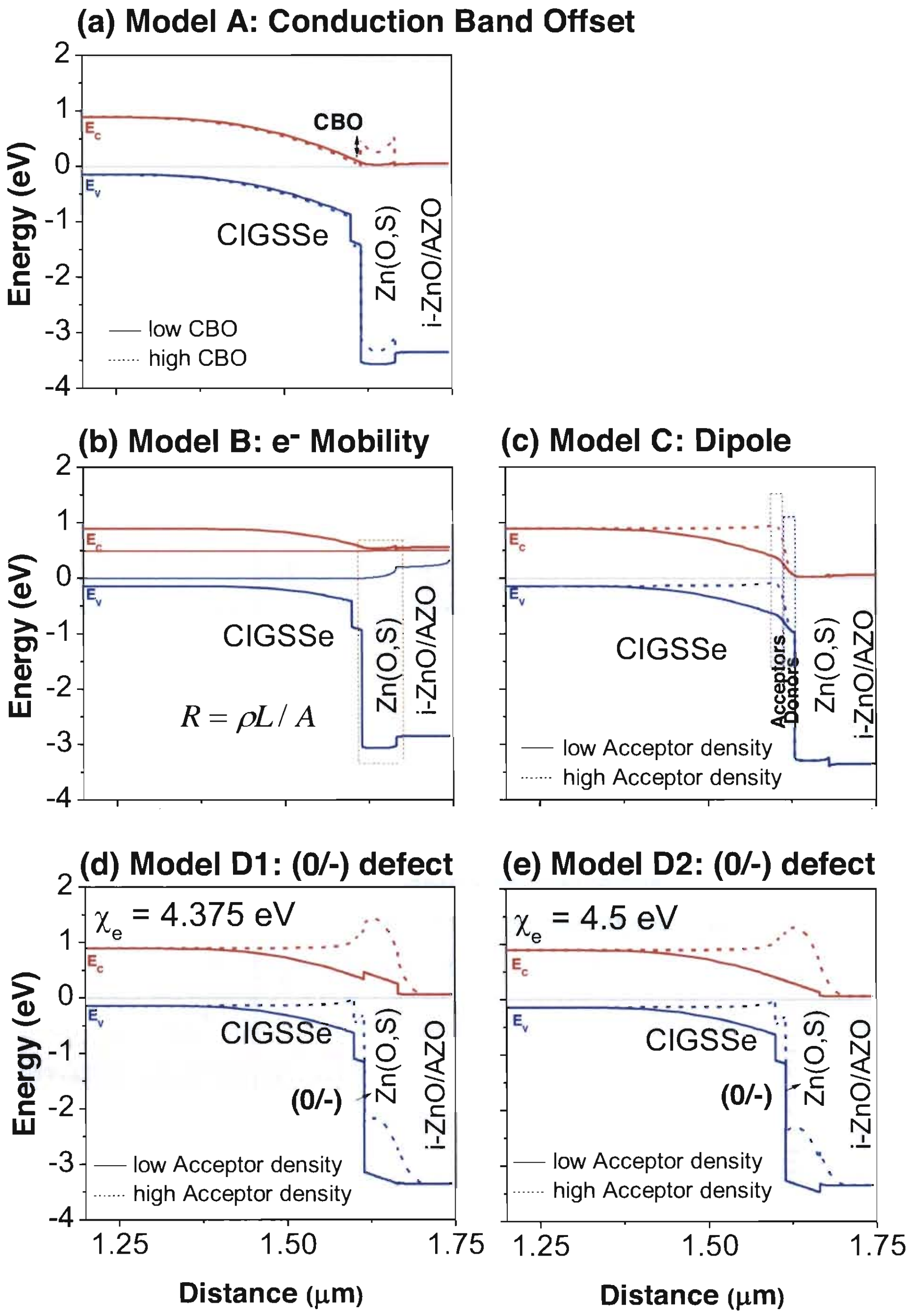

Figure 5.3 Band Diagrams from SCAPS-1D modelling with (a) increasing ΔE_C (CIGSSe/Zn(O,S)), (b) change in electron mobility, (c) dipole, (d) acceptor defect with ΔE_C (CIGSSe/Zn(O,S)) = +0.125 eV, and (e) acceptor defect with ΔE_C (CIGSSe/Zn(O,S)) = 0.0 eV.

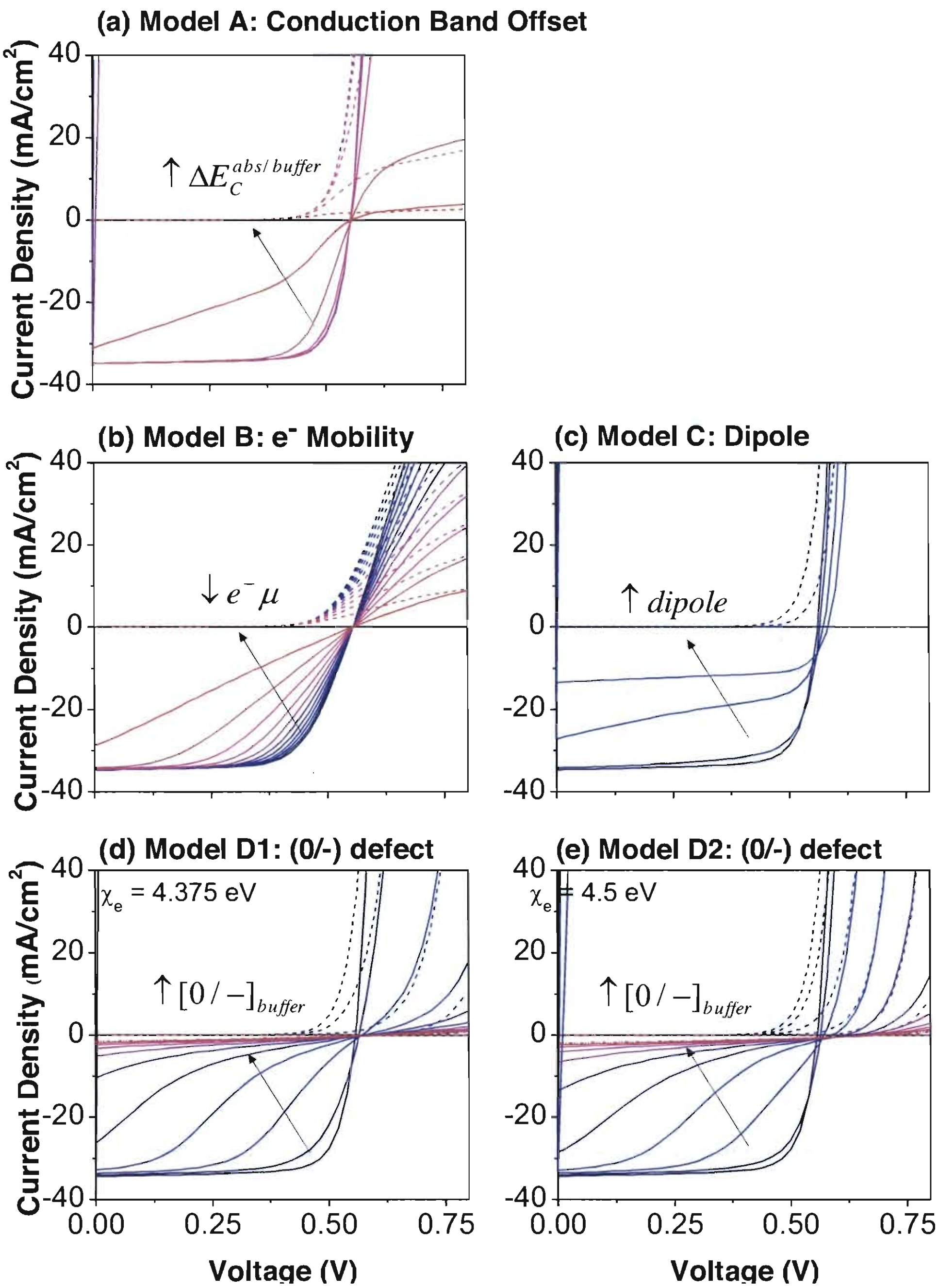

Figure 5.4 I-V curves from SCAPS-1D modelling corresponding to band diagrams with (a) increasing ΔE_C (CIGSSe/Zn(O,S)), (b) change in electron mobility, (c) dipole, (d) acceptor defect with ΔE_C (CIGSSe/Zn(O,S)) = +0.125 eV, and (e) acceptor defect with ΔE_C (CIGSSe/Zn(O,S)) = 0.0 eV.

From the results of the models, all possibilities showed a reduction of *FF* for devices.

Model A: an increase of CBO from 0.0 to 0.4 eV resulted in an increase in the barrier for electron separation. Correspondingly, the I-V curves show a reduction of *FF* and R_{sh}, and increase in R_s are observed, but no further increase was seen in the J_{SC} after the V_{OC} is crossed.

Model B: a change in electron mobility from decreasing resistivity can be expected after thermal annealing. Only at $\mu_e = 5 \times 10^{-5}$–10^{-6} cm^2/Vs can a reduction of *FF* be seen due to overall increase of resistance. This is not realistic as the typical measured values are $\mu_{c,ZnO} = 125$ cm^2/Vs and $\mu_{c,ZnS} = 160$–230 cm^2/Vs. Furthermore, electron mobility reduction does not lead to a change in the band alignment of the *p-n* junction. Neither is a crossover observed in the devices investigated. Therefore, this model is unlikely to apply.

Model C: shows that a disruption of the electric field by introduction of a dipole leads to decrease in R_{sh} but no kink is observed in the I-V curve, hence this model is not applicable to this system as well.

Model D: simulates the transition from an *n*-type ZnO which is heavily compensated, to increasing quantity of acceptor states and increasing *p*-type behavior the more S-rich the buffer. There is a characteristic kink in the devices when the current crosses the V_{OC} and decreased R_{sh} and increased R_s, following closely with the experimental data similar to the real devices at relaxed states, especially for those observed in CBD-Zn(O,S) devices.

However, the model is not complete without considering a slight positive conduction band offset between the absorber and buffer, which will produce a crossover for the illuminated vs. dark I-V curves plotted together. In this case, Model D1 rather than Model D2 has to be considered, since a crossover is also apparent in real devices.

Concluding this section, a plausible mechanism has been found that satisfactorily explain the cause of efficiency loss in Figure 5.1. The combination of a conduction band offset between the absorber/buffer and increasing amounts of acceptor states in the buffer bulk simulating both 1) an increase in bandgap of the buffer material and 2) increasing V_{Zn} states in the buffer bulk, may be used to explain the experimental observation in the next section.

5.3. Experimental

CIGSSe thin films were deposited on molybdenum coated glass substrates by a two-step sputtering with precursor consisting of copper, gallium and indium, and sulfur and selenium as gases as described in the process by Probst et al. [38]. Following a 5 min cleaning process in 2.5% NH_3(aq), Zn(O,S) buffer were deposited on CIGSSe absorbers by ALD [39-41]. During the deposition process, a 40 sccm high purity argon gas was used as the process and purging gas, and the chamber pressure was maintained at 106 Pa. The ALD process contained a DEZ:Ar:H_2O or H_2S:Ar pulse cycle with pulse length of 0.08:10:0.08 s for H_2O or 0.1:10 s for H_2S. The [O]:[S] content of the film was controlled by varying the S and O precursor pulse ratio in the ALD cycle. In order to vary the stoichiometric ratio of O and S with ALD in each device, the quantity of water and hydrogen sulfide in each pulse was tuned to achieve various composition of [O]:[S] = 1:0, 6:1, 4:1, 2:1, and 1:1. Zn(O, S) deposition by ALD method was carried out in a Cambridge Nanotec Fiji 200 system using diethylzinc ($Zn(C_2H_5)_2$, DEZ, purchased from Aldrich, >99%), H_2O (18 MΩ·cm) and H_2S (2.5% balanced in Ar) as the zinc, oxygen and sulfur sources, respectively. The reaction chamber and the precursor delivery line were maintained at 120 °C throughout the experiments. For example, a Zn(O, S) buffer layer using an average of six DEZ:Ar:H_2O:Ar cycles for every DEZ:Ar:H_2S:Ar cycle has a [O]:[S] pulse ratio of 6:1.

The ALD ZnO and ZnS growth rate are calibrated by measuring the film thicknesses on Si substrate using a spectroscopic ellipsometry (α-SE, J.A. Woollam) [42]. The experimental curves are fitted with the theoretically simulated model to derive the film properties. The fitting oscillator modes and the optical constant used for fitting are provided by J.A. Woollam. The growth rates of ALD ZnO and ZnS at 120 °C were 0.18 nm/cycle and 0.13 nm/cycle, respectively, and the buffers prepared on absorbers were ~50 nm thick. Devices with [O]:[S] = 6:1 and 4:1 ratios are hereby labelled as sulfur-poor Zn(O,S) and those with [O]:[S] = 2:1 ratio, sulfur-rich Zn(O,S). The semi-finished layers were completed by the deposition of a transparent *i*-ZnO/ZnO:Al front contact and an Al/Ni contact grid. The full devices produced efficiencies ranging from 10 to 15% as-fabricated. Light soaking on the devices was performed for 4 h with a Xenon lamp as sun simulator with 100 mW/cm .

In a typical TRPL experiment, a solar cell with the layer stack sequence of Mo/CIGSSe/Zn(O,S)/*i*-ZnO/ZnO:Al was excited with 650 nm wavelength generated by a quartz laser system at room temperature. With a pulse rate of 5 MHz, and a beam diameter of 1 μm, the injection level was fixed at $I_0 \sim 5 \times 10^7$ photons·cm^{-2} per pulse. Since the penetration depth into the absorber was calculated to 0.2 μm, this results in a generation density of 3.16×10^7 photons·cm^{-2}·s^{-1} which is much lower than 1 Sun condition ($\sim 10^{17}$ photons·cm^{-2}·s^{-1}), hence I_0 is defined to be low injection. With this condition, open circuit conditions could be assumed with no photo-voltage buildup. PL decay curves were measured in the approximate wavelength range of 1200–1300 nm by a Germanium avalanche photo-diode detector cooled with liquid N_2 with time-correlated single-photon counting [43].

A VG ESCALAB 220i-XL system equipped with a concentric hemispherical energy analyzer was used for X-ray photoelectron spectroscopy (XPS) to determine different Zn(O,S) compositions deposited on the absorber by ALD. The light source consists of a monochromatic Al Kα (1486.6 eV) for XPS characterization. A magnetic immersion lens was used to maximize the signal. Quantitative analysis was performed by first using a Shirley background subtraction before performing a least-square-error fit using a mixture of Gaussian-Lorentzian lineshapes [44]. Care was taken to ensure reasonable values for all the full width at half-maximum (FWHM) of the fitted components. The relative atomic concentrations were then calculated after taking into account the instrument transmission function together with the Scofield photoionization sensitivity factor [45]. All core-level peaks were references by assigning the adventitious carbon peak to 284.6eV.

Electrical measurements were performed at room temperature using a Rotating Parallel Dipole Line AC Hall System [46]. 100 nm thick quartz samples of 0.25 mm^2 were used to determine the electrical properties. Resistivity, carrier concentration, and electron mobility values were the average of three measurements.

I-V characterization was performed for devices after dark storage (i.e. relaxed state) which was subsequently light soaked under 1 Sun condition for 4 hours and measured again. The corresponding dark/illumination curves are plotted in Fig. 5.4(a)–(c) for sulfur-poor ([O]:[S] = 1:0–4:1), moderately sulfur-rich ([O]:[S] = 2:1) and highly sulfur rich ([O]:[S] = 1:1 Zn(O,S) devices, respectively. The moderately sulfur-rich 2:1 device had a crossover feature in its relaxed and light soaked state, suggesting metastability due to charge transport issue, which was not observed for the sulfur-poor devices. The highly sulfur-rich 1:1 device had distorted I-V features at both relaxed and light soaked state.

5.4. Results and Discussion

I-V characterization was performed for devices after dark storage (i.e. relaxed state) which was subsequently light soaked and measured again. The corresponding dark/illumination curves are plotted in Fig. 5.4(a)-(c) for sulfur-poor and sulfur-rich Zn(O,S) devices, respectively. The sulfur-rich 2:1 device had a crossover feature in its relaxed and light soaked state, suggesting metastability due to charge transport issue, which was not observed for the sulfur-poor devices.

The TRPL spectra for sulfur-poor and sulfur-rich Zn(O,S) are plotted in Fig. 5.4(d)-(f), respectively to clearly distinguish the decay lifetime(s). The detected PL intensity is tabulated in Table 5.3. For the sulfur-poor devices and the light soaked moderately sulfur-rich device, the exponential decay was fitted (after having subtracted a constant background intensity) as derived by Ahrenkiel [47] to derive the sweep out time of carriers [48, 49]:

$$I_{PL}(t) = A_1 e^{(\frac{-t}{\tau_1})} \tag{5.3}$$

Where t is time and A_1 is a fitting constant. For the rest of the relaxed and light soaked sulfur-rich devices, a bi-exponential decay was fitted to account for both τ_1 and a longer decay lifetime commonly associated with radiative recombination in the absorber (τ_2).

$$I_{PL}(t) = A_1 e^{(\frac{-t}{\tau_1})} + A_2 e^{(\frac{-t}{\tau_2})} \tag{5.4}$$

Where A_2 is a fitting constant. Since the measurement for all full devices were standardized, and the only variable here is the stoichiometric increase in sulfur in Zn(O,S), the discussion was focused on the PL decay profiles for full devices as a function of sulfur content in the buffer.

In all Zn(O,S) devices in their relaxed and light soaked states with the exception of the [O]:[S] = 1:1 device, τ_1 of <10 ns were observed [48, 49]. The short lifetime τ_1 indicates efficient sweeping out of charges in the space charge region. Corresponding to the short lifetime and low intensity, the I-V curves for all sulfur-poor devices (Figure 5.5(a)) and the light soaked 2:1 device (Figure 5.5(b)) indicated good charge transport. τ_2 was only observed in the relaxed state of the 2:1 Zn(O,S) device and both states of the 1:1 device (Figure 5.5(c)). This was comparable to the profile of long decay lifetime for bare CIGS absorber from etched devices [50, 51]. There is an increase in TRPL intensity from [O]:[S] = 1:0–1:1 for both the relaxed and light soaked states, respectively. Under low injection, the PL intensity follows the product of the equilibrium hole concentration (p_0) and amount of excess electrons injected (Δn), $p_0\Delta n$. When there is low defect density in the buffer, a stronger electric field leads to more efficient charge separation of holes and electrons, hence a short carrier lifetime and a small intensity are expected. Reduced strength of the electric field by a barrier in the *p-n* junction results in a much poorer separation and higher radiative recombination. As inferred from the TRPL data, devices in Table 5.3 mainly showed a small τ_1 and low PL peak intensity.

PL peak intensity were highest in sulfur-rich [O]:[S] = 2:1 device at its relaxed state and [O]:[S] = 1:1 at both relaxed and light soaked states of 3.91×10^4 – 5.52×10^4 (a.u.), indicative of high radiative recombination. Light soaking the relaxed 2:1 device reduces the blocking of the current of the dark I-V profile [Fig. 5.4(b)]. On the corresponding TRPL decay curve, the τ_2 component disappears and the PL intensity is reduced (Figure 5.5(d)). Since the peak intensity reduces to 1.21×10^4 (a.u.), it can be inferred that excess acceptor states are compensated by light soaking that results in photo-doping of the buffer and improvement of charge separation and transportation in the device [3, 4]. On the other hand, light soaking the 1:1 device did not significantly improve the device performance nor passivate its τ_2 component. It might be inferred that a high concentration of V_{Zn} or S_i acceptor states exist at this stoichiometry of sulfur in Zn(O,S) and it is not possible to improve the performance of the device by light soaking. The results here demonstrate a strong correlation of increasing metastability with increased sulfur content in the buffer. This causes an increasing stronger blocking effect under forward bias the higher the sulfur content.

Table 5.3 Decay lifetimes of relaxed and light soaked (LS) devices with Zn(O,S) [O]:[S] = 1:0, 6:1, 4:1, 2:1, and 1:1 determined by the single or bi-exponential decay fitting of the TRPL spectra).

[O]:[S]	**Condition**	**τ_1 (ns)**	**τ_2 (ns)**	**Intensity (10^4) (a.u.)**	**V_{OC} (V)**	**J_{SC} (mA/cm^2)**	***FF***	**Eff (%)**
1:0	Relaxed	5.67	–	0.1	0.31	29.9	56	5.2
	LS	8.45	–	0.09	0.37	32.1	57	6.8
6:1	Relaxed	5.29	–	0.18	0.48	34.9	50	8.4
	LS	4.13	–	0.07	0.48	34.3	51	8.4
4:1	Relaxed	4.82	–	0.27	0.45	37.1	59	9.9
	LS	6.56	–	0.07	0.45	37.6	58	9.8
2:1	Relaxed	9.89	**29.4**	**5.52**	**0.59**	**37.0**	**58**	12.7
	LS	6.36	–	1.21	0.59	36.7	62	13.4
1:1	Relaxed	14.8	46.0	3.91	0.34	3.7	19	0.2
	LS	15.2	45.5	4.82	0.35	4.5	18	0.3

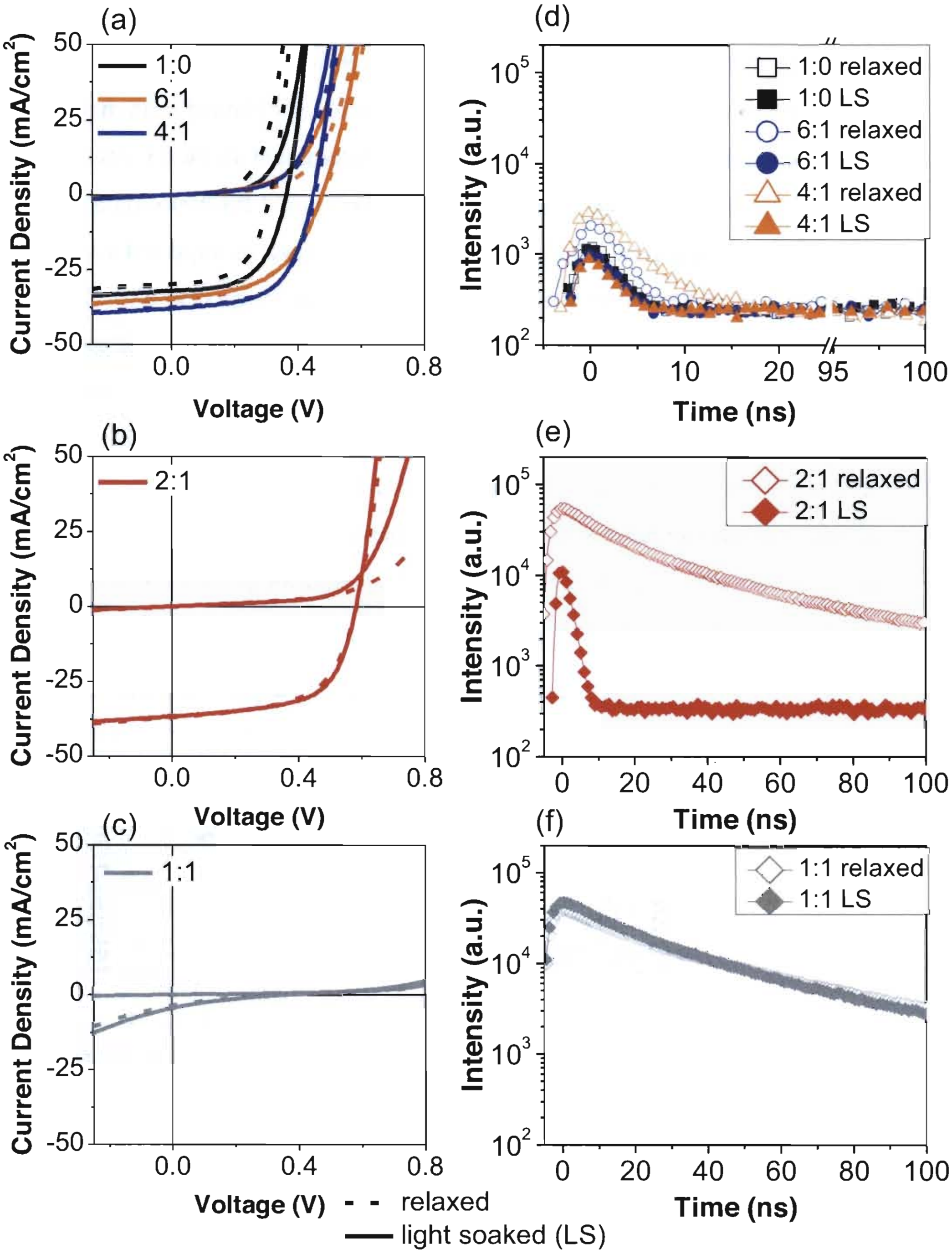

Figure 5.5 I-V curves of relaxed (dashed lines) and light soaked (LS) (solid lines) Zn(O,S) buffered devices with (a) sulfur-poor ([O]:[S] = 1:0, 6:1, 4:1), (b) moderately sulfur-rich ([O]:[S] = 2:1) buffer, (c) highly sulfur-rich ([O]:[S] = 1:1) buffer and their respective lifetimes for (d) sulfur-poor, (e) moderately sulfur-rich, and (f) highly sulfur-rich devices determined by the single or bi-exponential decay fittings of the TRPL spectra, respectively.

In order to validate the experimental observations, SCAPS-1D simulations representing the sulfur-poor, moderately sulfur-rich, and highly sulfur-rich cases were performed. Parameters representative of the real devices were first obtained from materials or electrical measurements. The absorber band gap was determined to be approximately 1.0 eV by external quantum efficiency measurements. Based on XPS measurement of the absorber surface, the sulfur-rich, copper-poor absorber surface is expected to form an Ordered Vacancy Compound (OVC). For this reason, a 15 nm thick OVC was added to reflect type inversion (n-type) between the absorber and buffer [13]. The valence band maximum and conduction band minimum values of different ratios of Zn(O,S) synthesized were estimated using the XPS [S]/([S]+[O]) ratios, which were 0.10–0.22 for [O]:[S] = 1:0–1:1, depicted in Figure 5.6. As a result, except for pure ZnO where [O]:[S] = 1:0, any change in conduction band minimum was small and offset was assumed to be similar for sulfur-poor and sulfur-rich devices defined here [16, 52]. Hence for all cases, CBO was set at +0.2 eV between the CIGSSe and Zn(O,S).

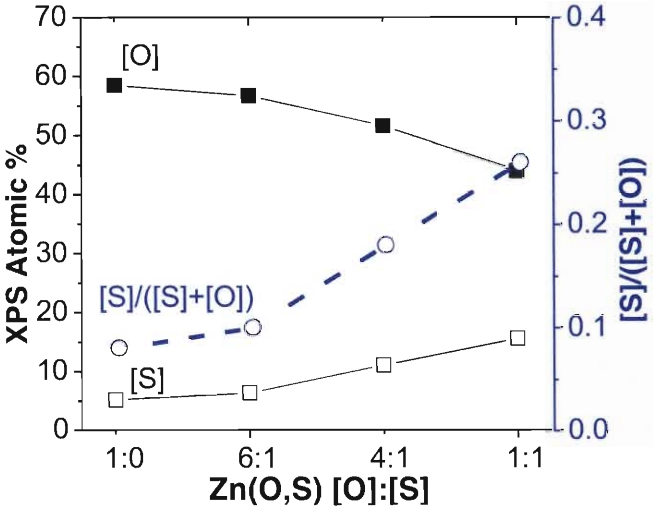

Figure 5.6 XPS Atomic Ratio for ALD prepared Zn(O,S) of [O]:[S] = 1:0, 6:1, 4:1, 1:1 and their respective [S]/([S]+[O]) ratios.

Resistivities of Zn(O,S) were found to be 5.79 x 10^3 Ω/□ for the Zn(O,S) film of [O]:[S] = 4:1, 1.78 x 10^9 Ω/□ for [O]:[S] = 2:1, and 1.84 x 10^{10} Ω/□ for [O]:[S] = 1:1. From AC Hall measurements, electron mobility (8.58 $cm^2 \cdot V^{-1} \cdot s^{-1}$) and carrier concentration (1.65 x 10^{19} cm^{-3}) were determined for the [O]:[S] = 4:1 sample, comparable to values reported in literature [53, 54]. In a compensated semiconductor material such as Zn(O,S), the net charge density ρ is the sum of holes (*p*) and electrons (*n*) as well as ionized acceptor (N_A) and donor atoms (N_D). It is expressed as $\rho = q(p - n + N_D - N_A)$, where q is the electric charge. Ionized acceptor states speculated to influence charge separation form a part of the total carrier concentration. As with other simulation studies [55], the concentrations where ionized acceptor states influence distortion to the I-V curve are between 7.5×10^{17} to 1.3×10^{18} cm^{-3}, and hence input parameters of acceptor density in the buffer in Table 5.4 based were performed at this range. These acceptor states were defined at 1.0 eV above the valence band of the Zn(O,S) [10], with density adjusted to simulate the relaxed and light soaked states for sulfur-poor and sulfur-rich Zn(O,S) devices. The capture cross section of holes for these acceptor states was assumed and set to 10^{-12} cm^2. The optical absorption parameter of the Zn(O,S) was estimated based on standard ZnO/ZnS absorption files [27].

Table 5.4 Input parameters for SCAPS-1D simulation of acceptor densities for sulfur-poor, moderately sulfur-rich and highly sulfur-rich devices at relaxed and light soaked states where NA is the density of (0/-) acceptors in the Zn(O,S) buffer.

State	**Sulfur-poor Zn(O,S) N_A (cm^{-3})**	**Moderately Sulfur-rich Zn(O,S) N_A (cm^{-3})**	**Highly Sulfur-rich Zn(O,S) N_A (cm^{-3})**
Relaxed	9.75×10^{17}	1.03×10^{18}	1.25×10^{18}
Light Soaked	7.50×10^{17}	7.50×10^{17}	1.30×10^{18}

[a] N_t is the density of (0/-) acceptors in the Zn(O,S) buffer

Figure 5.7 depicts I-V curves and electronic band structures constructed from SCAPS-1D simulation. Except for the highly sulfur-rich 1:1 device, light soaked states of the sulfur-poor and sulfur-rich devices were assumed to exhibit the same behavior and only compare their relaxed states. For sulfur-poor Zn(O,S), the acceptor density at the relaxed state could be compensated by V_{Zn} donors hence metastability is impeded. A slight increase of acceptor density from this point by 5% led to a significant crossover for the relaxed, moderately sulfur-rich Zn(O,S) device (cf. I-V curves in Figure 5.7(a) vs. 5.7(b)). At this state, excess acceptor states were occupied by electrons, and the conduction band and valence band of the Zn(O,S) were shifted upwards. This resulted in reduced band bending and reduced potential drop at the absorber/buffer interface at +0.5 V bias (cf. band diagrams in Figure 5.7(c) vs. 5.7(d)]. Backflow of electrons to the absorber in Fig 5.7(d) relaxed and hence recombination was enhanced, which agreed well with the high PL intensity observed in these experiment. The subsequent generation of electron-hole-pairs by light soaking led to compensation of the negatively charged acceptor states in the buffer by holes, resulting in an optimal band alignment at the *p*-*n* junction with less potential drop across the buffer, hence the electron quasi-Fermi level (E_{fn}) at the interface gets closer to the conduction band minimum of Zn(O,S). For the highly sulfur-rich 1:1 device (Figure 5.7(c), 5.7(f)), the concentration of V_{Zn} acceptor states vastly exceeds the other cases. Under the same light soaking conditions, assuming the same extent of passivation of V_{Zn} acceptor states, this will result in a large barrier in the *p*-*n* junction whereby backflow of electrons is preferred. Consequently, recombination is favored for both relaxed and light soaked states of this device.

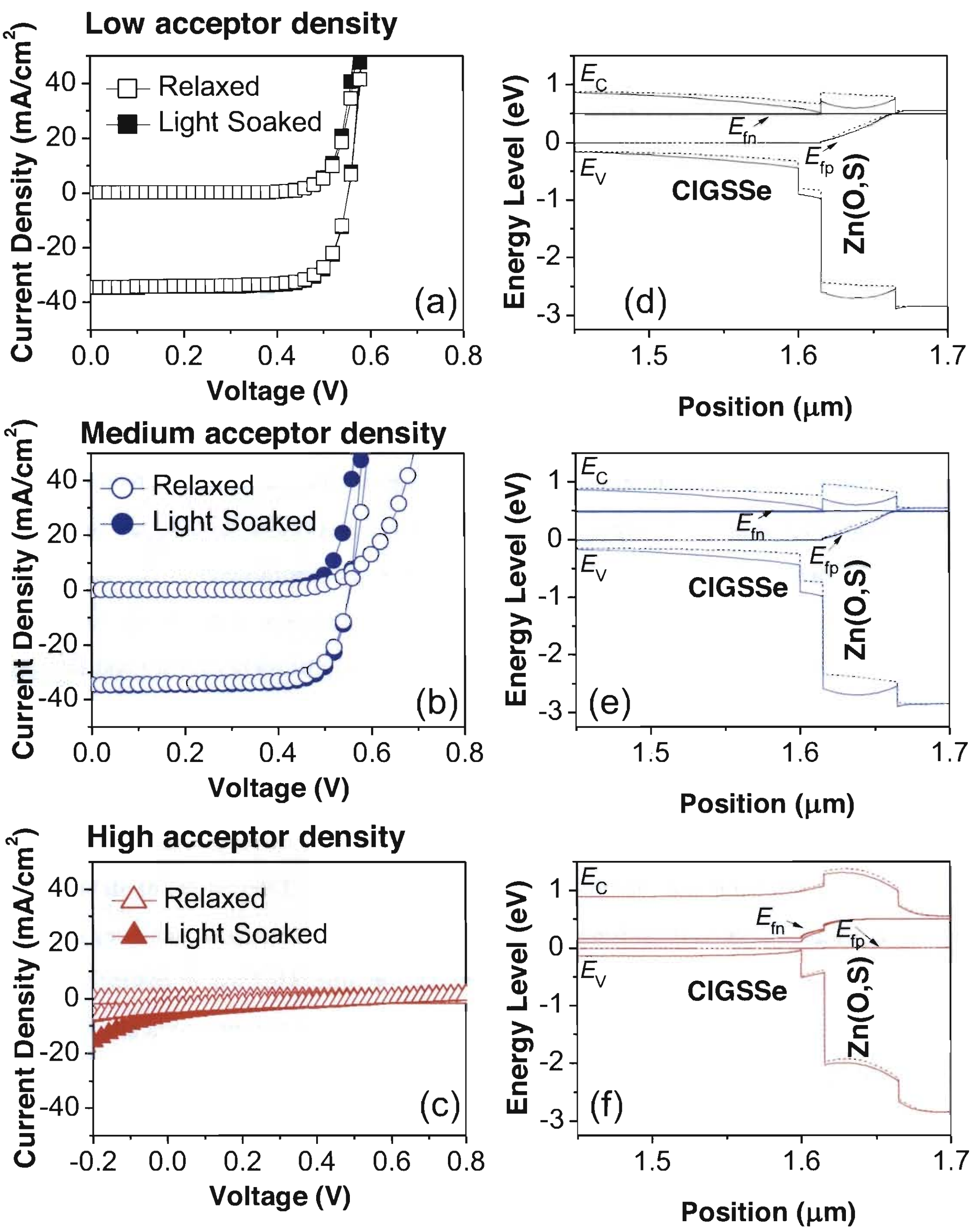

Figure 5.7 Simulated I-V curves at relaxed (dashed lines) and light soaked states (solid lines) Zn(O,S) devices for (a) sulfur-poor Zn(O,S) devices and (b) moderately sulfur-rich Zn(O,S) devices and (c) highly sulfur-rich Zn(O,S) and the corresponding band diagrams at +0.5 V bias for (d) low sulfur content with low acceptor density (e) moderately high sulfur content with moderate acceptor density and (f) high sulfur content with moderate acceptor density.

In this chapter, carrier lifetime τ_1 obtained with TRPL were shown to be in the range of <10 ns for sulfur-poor and moderately sulfur-rich CIGSSe/Zn(O,S) solar cells. For relaxed devices, there is increasing radiative recombination at the surface of the absorber with increasing sulfur content in Zn(O,S) buffer. In addition, metastability in moderately sulfur-rich Zn(O,S) devices prone to relaxation and charge transport issues can be evaluated by the presence of a secondary, greater lifetime component τ_2 in relaxed solar cells. Light soaking generates photons to neutralize excess negative charges in the buffer of the moderately sulfur-rich Zn(O,S) device, reducing radiative recombination by improved charge separation and compensating the secondary lifetime component. On the other hand, highly sulfur-rich Zn(O,S) devices showed no improvement of I-V characteristics before and after light soaking, indicating radiative recombination is still dominant and charge separation in the device is poor. The results here demonstrate good correlation of the increasing sulfur content to the appearance of the secondary lifetime component, implying an increased density of acceptor states leads to worsening I-V characteristics. This leads to a better understanding of metastability and charge transport issues in Zn(O,S) buffered devices.

5.5. Conclusion

When selecting the stoichiometry of the buffer for fabrication of devices, one might consider a relatively sulfur-poor Zn(O,S) of 4:1 ratio device that achieves sufficiently high J_{SC} and V_{OC} and avoid metastability at the same time. This would ensure a stable solar cell output that does not fluctuate due to dark storage. On the extreme ends, a 0:1 ratio (pure ZnO) will lead to low V_{OC} due to band alignment mismatch with the CIGSSe absorber. A sulfur-rich 1:1 ratio favors the formation of excessive acceptor states in the buffer, distorting the I-V curve and resulting in a low J_{SC} and *FF*. With these considerations, the optimal stoichiometry of [O]:[S] in the buffer should be 4:1 ratio to obtain a device of high efficiency and low metastability.

References

[1] D. Hariskos, S. Spiering, M. Powalla, *Thin Solid Films* **2005**, *480–481*, 99–109.

[2] I. L. Eisgruber, J. E. Granata, J. R. Sites, J. Hou, J. Kessler, *Sol. Energy Mater. Sol. Cells* **1998**, *53*, 367–377.

[3] A. O. Pudov, J. R. Sites, M. A. Contreras, T. Nakada, H. W. Schock, *Thin Solid Films* **2005**, *480–481*, 273–278.

[4] M. Igalson, A. Urbaniak, P. Zabierowski, H. A. Maksoud, M. Buffiere, N. Barreau, S. Spiering, *Thin Solid Films* **2013**, *535*, 302–306.

[5] K. Kushiya, S. Kuriyagawa, K. Tazawa, T. Okazawa, M. Tsunoda, in *Conference Record of the 2006 IEEE 4th World Conference on Photovoltaic Energy Conversion, Vol. 1*, **2006**, pp. 348–351.

[6] Y. Okuda, in *2012 IEEE International Reliability Physics Symposium*, **2012**, pp. PV.1.1–PV.1.6.

[7] W. Witte, D. Hariskos, M. Powalla, *Thin Solid Films* **2011**, *519*, 7549–7552.

[8] C. Platzer-Björkman, T. Törndahl, A. Hultqvist, J. Kessler, M. Edoff, *Thin Solid Films* **2007**, *515*, 6024–6027.

[9] S. Tao, J. T. McGoffin, J. R. Sites, *IEEE J. Photovoltaics* **2014**, *4*, 942–947.

[10] J. B. Varley, V. Lordi, *Appl. Phys. Lett.* **2013**, *103*, 102103.

[11] A. Niemegeers, M. Burgelman, *J. Appl. Phys.* **1997**, *81*, 2881–2886.

[12] M. Burgelman, P. Nollet, S. Degrave, *Thin Solid Films* **2000**, *361–362*, 527–532.

[13] D. Schmid, M. Ruckh, F. Grunwald, H. W. Schock, *J. Appl. Phys.* **1993**, *73*, 2902–2909.

[14] S. Sharbati, J. R. Sites, *IEEE J. Photovoltaics* **2014**, *4*, 697–702.

[15] T. Minemoto, T. Matsui, H. Takakura, Y. Hamakawa, T. Negami, Y. Hashimoto, T. Uenoyama, M. Kitagawa, *Sol. Energy Mater. Sol. Cells* **2001**, *67*, 83–88.

[16] B. K. Meyer, A. Polity, B. Farangis, Y. He, D. Hasselkamp, T. Krämer, C. Wang, *Appl. Phys. Lett.* **2004**, *85*, 4929–4931.

[17] M. Bär, J. Reichardt, A. Grimm, I. Kötschau, I. Lauermann, K. Rahne, S. Sokoll, M. C. Lux-Steiner, C.-H. Fischer, L. Weinhardt, E. Umbach, C. Heske, C. Jung, T. P. Niesen, S. Visbeck, *J. Appl. Phys.* **2005**, *98*, 053702.

[18] C. Platzer-Björkman, T. Törndahl, D. Abou-Ras, J. Malmström, J. Kessler, L. Stolt, *J. Appl. Phys.* **2006**, *100*, 044506.

[19] S. Kasap, P. Capper, *Springer Handbook of Electronic and Photonic Materials*, Springer, **2006**.

[20] N. K. Morozova, V. A. Kuznetsov, M. V. Fok, *Moscow: Nauka* **1987**.

[21] P. YU, M. Cardona, *Fundamentals of Semiconductors: Physics and Materials Properties*, Springer Berlin Heidelberg, **2013**.

[22] J. I. Pankove, *Optical Processes in Semiconductors*, Dover, **1971**.

[23] R. C. Weast, C. R. Company, *CRC Handbook of Chemistry and Physics: A Ready-reference Book of Chemical and Physical Data. Editor, Robert C. Weast*, CRC Press, **1975**.

[24] H. Kukimoto, T. Koda, S. Shionoya, *Infrared Absorption Due to Donor States in ZnS Crystals*, Inst. for Solid State Physics, **1967**.

[25] M. Aven, J. S. Prener, *Physics and chemistry of II-VI compounds*, Noord-Hollandsche U.M., **1967**.
[26] H. E. Ruda, B. Lai, *J. Appl. Phys.* **1990**, *68*, 1714–1719.
[27] S. Adachi, *Optical Constants of Crystalline and Amorphous Semiconductors: Numerical Data and Graphical Information*, Springer US, **2013**.
[28] T. S. Moss, M. Balkanski, *Handbook on semiconductors*, North-Holland, **1980**.
[29] U. V. Desnica, *Prog. Cryst. Growth Charact. Mater.* **1998**, *36*, 291–357.
[30] R. N. Bhargava, *J. Cryst. Growth* **1982**, *59*, 15–26.
[31] P. H. Kasai, Y. Otomo, *J. Chem. Phys.* **1962**, *37*, 1263–1275.
[32] J. W. Allen, *Semicond. Sci. Technol.* **1995**, *10*, 1049.
[33] B. K. Meyer, W. Stadler, *J. Cryst. Growth* **1996**, *161*, 119–127.
[34] Z. Wang, L. L. Daemen, Y. Zhao, C. S. Zha, R. T. Downs, X. Wang, Z. L. Wang, R. J. Hemley, *Nat. Mater.* **2005**, *4*, 922–927.
[35] H. Wiedemeier, *Zeitschrift für anorganische und allgemeine Chemie* **2006**, *632*, 1717–1727.
[36] S. Shionoya, W. M. Yen, H. Yamamoto, *Phosphor Handbook*, CRC Press, **2006**.
[37] M. Nichterwitz, R. Caballero, C. A. Kaufmann, H.-W. Schock, T. Unold, *J. Appl. Phys.* **2013**, *113*, 044515.
[38] V. Probst, I. Koetschau, E. Novak, A. Jasenek, H. Eschrich, F. Hergert, T. Hahn, J. Feichtinger, M. Maier, B. Walther, V. Nadenau, *IEEE J. Photovoltaics* **2014**, *4*, 687-692.
[39] A. Shimizu, S. Chaisitsak, T. Sugiyama, A. Yamada, M. Konagai, *Thin Solid Films* **2000**, *361–362*, 193–197.
[40] E. B. Yousfi, B. Weinberger, F. Donsanti, P. Cowache, D. Lincot, *Thin Solid Films* **2001**, *387*, 29–32.
[41] T. Kobayashi, T. Kumazawa, L. Kao, T. Nakada, *Sol. Energy Mater. Sol. Cells* **2013**, *119*, 129–133.
[42] J. A. Woollam, http://www.jawoollam.com/pdf/Alpha_Brochure.pdf.
[43] D. V. O'Connor, D. Phillips, *Time-correlated single photon counting*, Academic Press, London; Orlando, **1984**.
[44] M. P. Seah, I. S. Gilmore, S. J. Spencer, *Surf. Sci.* **2000**, *461*, 1–15.
[45] J. H. Scofield, *J. Electron. Spectrosc. Relat. Phenom.* **1976**, *8*, 129–137.
[46] T. G. O. Gunawan, US Patent 9,041,389 (2015); O. Gunawan, Y. Virgus, K. F. Tai, Appl. Phys. Lett. 106, 062407 (2015). Dev. Team: O. Gunawan, T. Gokmen, K. F. Tai, Y. Virgus, and M. Pereira, IBM Research (2015).
[47] R. K. Ahrenkiel, *Solid-State Electron.* **1992**, *35*, 239–250.
[48] M. Maiberg, R. Scheer, *J. Appl. Phys.* **2014**, *116*, 123710.
[49] M. Maiberg, R. Scheer, *J. Appl. Phys.* **2014**, *116*, 123711.
[50] W. K. Metzger, I. L. Repins, M. A. Contreras, *Appl. Phys. Lett.* **2008**, *93*, 022110.
[51] W. K. Metzger, I. L. Repins, M. Romero, P. Dippo, M. Contreras, R. Noufi, D. Levi, *Thin Solid Films* **2009**, *517*, 2360–2364.
[52] T. Adler, *Ph.D. thesis, Technische Universität Darmstadt* **2013**.
[53] H. H. Park, R. Heasley, R. G. Gordon, *Appl. Phys. Lett.* **2013**, *102*, 132110.
[54] H. H. Park, A. Jayaraman, R. Heasley, C. Yang, L. Hartle, R. Mankad, R. Haight, D. B. Mitzi, O. Gunawan, R. G. Gordon, *Appl. Phys. Lett.* **2014**, *105*, 202101.

[55] N. Naghavi, S. Temgoua, T. Hildebrandt, J. F. Guillemoles, D. Lincot, *Prog. Photovoltaics Res. Appl.* **2015**, *23*, 1820–1827.

Chapter 6

Mitigation of Metastability in Cu(In,Ga)(S,Se)$_2$/Zn(O,S) Devices

This chapter demonstrates low metastabilities in high efficiency Zn(O,S)-buffered CIGSSe solar cells through a careful consideration of $Cu(In_{(1-x)}Ga_x)(S_ySe_{(1-y)})_2$ *and* ZnO_xS_y *stoichiometries. The avoidance of metastable solar cells, i.e. solar cells susceptible to dark storage relaxation, can be achieved by considering a small conduction band offset between the absorber and buffer and keeping the sulfur content in the buffer low (sulfur atomic% = 11% in the buffer). This combination enables cells to reach 16.5% efficiency and at the same time, avoid the hot light soaking step. Temperature-dependent current-voltage measurements performed for full devices with Zn(O,S) [O]:[S] = 6:1 on the four absorbers utilized in this study determined that bulk recombination as the main recombination mechanism of highly efficient solar cells. Long term dark storage tests at 3 months 25 °C ambient showed that the solar cells do not relax, as evidenced by a lack of change in I-V parameters after a subsequent light soaking step.*

6.1. Introduction

Conventional Cu(In,Ga)Se_2 (CIGS) thin film solar cells utilize cadmium sulfide (CdS) as a buffer in their device architecture, but since less toxic materials like zinc oxysulfide (Zn(O,S)) can also be a viable buffer with comparable cell efficiencies, they are gradually replacing CdS in CIGS solar cells. Zn(O,S) having a higher bandgap that is tunable by changing the oxygen-to-sulfur ([O]:[S]) ratio [1, 2] gives much room for interfacial engineering and optimization of the conduction band offset (CBO) between the CIGS absorber and the Zn(O,S) buffer [3-5]. A high cell efficiency of 22.3% has been achieved for chemical bath deposition (CBD) Zn(O,S) buffered Cu(In,Ga)(S,Se)$_2$ (CIGSSe), and this has been scaled up to the module level at Solar Frontier K. K. [6]. The current issue with CBD-Zn(O,S) is its susceptibility towards relaxation of its cell efficiency under dark storage in a matter of days. This is attributed to a loss of fill factor (*FF*) and a kink in the illuminated current-voltage (I-V) curve, termed as metastability [7, 8]. It has been shown that high sulfur content in CBD-Zn(O,S) widens the bandgap of the material and lead to a band mismatch between the conduction bands of CIGSSe and Zn(O,S) and creates a barrier for charge transport [9]. It was also shown in Chapter 5 that a higher sulfur content could be linked to higher acceptor densities that causes charge separation issues in devices.

The hot light soaking steps are (1) annealing and (2) light soaking steps. The annealing step at 200 °C for 10 min after buffer deposition leads to outdiffusion of copper from CIGS in the direction of the buffer, and zinc diffusing in the opposite direction from the buffer into the absorber. The purpose of this step has been suggested to improve the *p-n* heterojunction by encouraging the redistribution of elements, especially in-diffusion of zinc which creates a buried *p-n* junction within the first nanometers of the CIGSSe absorber [10]. It has been further suggested by Bär [11] that the copper out-diffusion during chemical bath deposition (CBD) of Zn(O,S) led to its incorporation as a $(Zn_{(1-z)},Cu_{2z})S$ monolayer as the rest of the buffer was formed. The implication of having this layer is a lower bandgap at this penultimate layer before the ZnS layer since E_g^{ZnS} = 3.68 eV [46] and $E_g^{Cu_2S}$ =1.20 eV [47].With Zn_{Cu}^+ acceptor states present in this intermixed region, it was suggested to enhance downward band bending at the absorber surface next to the buffer leading to a reduction of recombination at this heterojunction.

Besides, the post-deposition annealing step in air had been found to increase V_{OC} by increasing the acceptor density and reducing the space charge width in devices with the $CuInGaSe_2$/Zn(O,S)/ZnMgO configuration [12].

The second step, light soaking, was suggested to improve the *FF* by the following

(1) Removal of $Zn(OH)_2$ in the CBD-Zn(S,O,OH) buffer [13]

(2) Decreasing effective barrier height at buffer/CIGS interface caused by photogenerated electrons [9, 14, 15]

As illustrated in Figure 6.1, the loss of water during photochemical reaction converting zinc hydroxides to oxides [16] was reversible if light soaking was performed at room temperature (Fig. 6.1 (a)), since water was still at close proximity and the reverse reaction could form hydroxides again in dark storage, leading to *FF* reduction [13]. A combined hot light soaking (HLS) step at 130 °C for 40 min had been suggested by Kushiya (Fig. 6.1 (b)). This had been found to not only stabilize the *p-n* heterojunction but also improve the I-V parameters by the permanent removal of water molecules from the surface of the buffer [13]. The same study also found that annealing the full device above 150 °C led to sulfur and copper diffusion into the buffer, destroying the *p-n* junction.

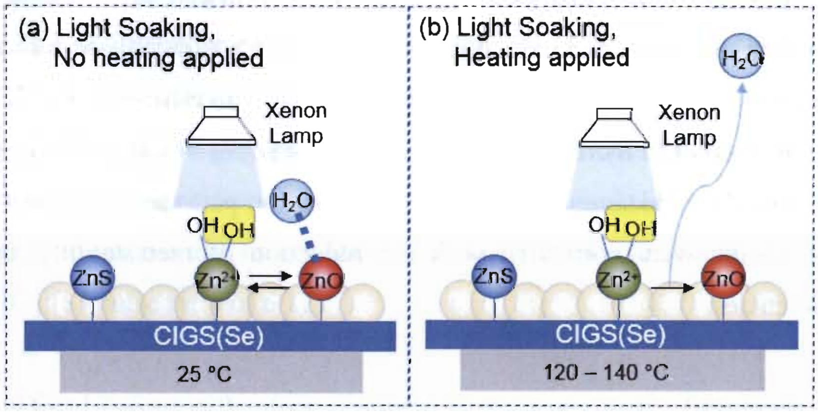

Figure 6.1 Light Soaking step (a) at room temperature, (b) with concurrent heating at 120–140 °C.

Additionally, the effectiveness of the light soaking step depends very much on the wavelength of the irradiation. With different short-wavelength cutoff filters of 400 nm, 500 nm, and 600 nm, Serhan demonstrated for devices with configuration of CIGS/CBD-Zn(O,S)/$Zn_{0.74}Mg_{0.26}O$ the importance of short wavelengths (400 nm) in improving the V_{OC} and J_{SC} during light soaking [17].

The second effect, which is the change in band alignment of the absorber/buffer interface, had been widely discussed. Varying the stoichiometry of Zn(O,S) by changing the oxygen-to-sulfur ([O]:[S]) ratio [1, 2] allowed for bandgap changes in this material. This enabled interfacial engineering and optimization of the conduction band offset (CBO) between the CIGSSe absorber and the Zn(O,S) buffer [4, 18].

Since elements in the CIGSSe absorber and the Zn(O,S) buffer may be varied to achieve band gap changes in the device, the approaches towards solving metastability in these Zn(O,S)/CIGSSe devices were

(1) Varying the absorber's stoichiometry by varying the sulfur content at the absorber surface
(2) Varying the buffer's stoichiometry by ALD

In this chapter, the link between a good combination of stoichiometries for both the absorber and buffer and reduction of metastability was established. Fundamental materials properties of the absorber and buffer were investigated by X-ray Photoelectron Spectroscopy (XPS). Temperature dependent current-voltage (I-V-T) measurements were performed to understand the major recombination pathway of a high efficiency solar cell. The results were correlated with the reduction of metastability and increase in cell efficiencies.

6.2. Experimental

6.2.1. Sample Preparation

CIGSSe thin films were deposited on Mo coated glass substrates using a single-stage sputtering process as described by Probst *et al.* [19]. At the absorber surface, the amount of [S]/[Se] was varied by introducing different quantities of sulfur during the sulfurization step. The absorbers were etched with 2.5 mol% NH_4OH solution for 5 min and a ~50 nm layer of ZnO or Zn(O,S) buffer was deposited on top of each absorber by means of atomic layer deposition (ALD) or chemical bath deposition (CBD). This was completed with an *i*-ZnO/AZO window by rf sputtering. Finally, an Al/Ni grid was evaporated to complete the devices with each cell having a cell area of 0.5 cm^2.

The ALD process [20-22] is described as follows. In order to vary [O] and [S] with ALD in each device, the quantity of water and hydrogen sulfide in each pulse was tuned to achieve various composition of [O]:[S] = 1:0, 6:1, 4:1, 2:1, and 1:1. Zn(O,S) deposition by ALD method was carried out on a Cambridge Nanotec Fiji 200 system using diethylzinc ($Zn(C_2H_5)_2$, DEZ, purchased from Aldrich, >99%), H_2O (18 MΩ/cm) and H_2S (2.5 % balanced in Ar) as the zinc, oxygen and sulfur sources, respectively. The reaction chamber and the precursor delivery line were maintained at 120 °C throughout the experiments. During the deposition process, a 40 sccm high purity argon gas was used as the process and purging gas, and the chamber pressure was maintained at 106 Pa. The ALD process contained a DEZ:Ar:H_2O or H_2S:Ar pulse cycle with pulse length of 0.08 s: 10 s : 0.08 s for H_2O or 0.1 s for H_2S : 10 s, respectively. The [O]:[S] content of the film was controlled by varying the S and O precursor pulse ratio in the ALD cycle. For example, a Zn(O,S) buffer layer using an average of six DEZ:Ar:H_2O:Ar cycles for every DEZ:Ar:H_2S:Ar cycle has a [O]:[S] pulse ratio of 6:1.

The ALD ZnO and ZnS growth rate are calibrated by measuring the film thicknesses on Si substrate using a spectroscopic ellipsometry (α-SE, J.A. Woollam).[23] The experimental curves are fitted with the theoretically simulated model to derive the film properties. The fitting oscillator modes and the optical constant used for fitting are provided by J.A. Woollam. The growth rates of ALD ZnO and ZnS at 120 °C are 0.18 nm/cycle and 0.13 nm/cycle, respectively, and all devices had 50 nm buffer thickness.

The CBD process was utilized to deposit the buffer in two different [O]:[S] ratios. The first route used in this work was developed by Ennaoui et al. $ZnSO_4$ was mixed with thiourea ($SC(NH_2)_2$) in an aqueous solution maintained at ~75 °C to form a $Zn(SCNH_2)_2)_n)$ complex. Ammonia (NH_3) was added to the base solution to complex with excess free Zn^{2+} ions. The pH of the solution was maintained around 10–11 throughout the deposition. After 10 min, the solution turned milky and the substrates were taken out and washed with 10% NH_3 solution to avoid uncontrolled precipitation of $Zn(OH)_2$ on the sample. The bilayer was annealed in air at 200 °C for 5 min before window layer deposition.

The alternative route developed by Nemec et al. was adapted from cadmium sulfide deposition by replacing $CdSO_4$ precursor with $ZnSO_4$ precursor [24]. The procedure is similar to the process developed by Ennaoui, except that an ammonia-free complexing agent is used. Due to confidentiality (patent pending), disclosure of the detailed concentration and experimental conditions is not to be made at the reporting date.

After the deposition of the Zn(O,S) thin films, the devices were completed by the addition of a *i*-ZnO/AZO window layer and an Al/Ni grid. Manual scribing was performed to define cell areas of ~0.5 cm^2.

6.2.2. Electrical Characterizations

Standard cell measurements were performed at the ZSW 1) as fabricated, 2) after annealing for 30 min at 200 °C, and 3) after light soaking for 30 min with a Xenon lamp at AM1.5G condition. Temperature-dependent electrical measurements were carried out for 0.5 cm^2 devices after the post-treatments. They were mounted in an Optistat DN-V nitrogen bath vacuum loading cryostat with quartz glass window. At each temperature step, I-V characteristics were measured by an Agilent 4155C Semiconductor Parameter Analyzer and a 50W OSRAM Halogen Lamp, and admittance spectroscopy was measured by a Hewlett Packard 4192A LF Impedance Analyzer.

6.2.3. Materials Characterizations

A VG ESCALAB 220i-XL system equipped with a concentric hemispherical energy analyzer was used for X-ray photoelectron spectroscopy (XPS) to determine differing $Cu(In_{(1-x)}Ga_x)(S_ySe_{(1-y)})_2$ stoichiometry at the absorber surface for Absorbers A, B, C, and D. The light source consists of a monochromatic Al Kα (1486.6 eV) for XPS characterization. A magnetic immersion lens was used to maximize the signal. Quantitative analysis was performed by first using a Shirley background subtraction before performing a least-square-error fit using a mixture of Gaussian-Lorentzian lineshapes [25]. Care was taken to ensure reasonable values for all the full width at half-maximum (FWHM) of the fitted components. The relative atomic concentrations were then calculated after taking into account the instrument transmission function together with the Scofield photoionization sensitivity factor [26]. All core-level peaks were references by assigning the adventitious carbon peak to 284.6eV.

6.3. Results and Discussion

6.3.1. Ideal absorber/buffer combination

It has been well-established that both the [Ga]:[In] and [S]:[Se] ratios shift the valence band and/or conduction band, resulting in bandgap change in the CIGSSe absorber [27]. Each component of the penternary CIGSSe system, consisting of Cu, In, Ga, S, and Se, can affect the CBM, VBM, and bandgap of the material, and have been used to create a grading effect in the absorber layer of these solar cells. From the four possible combinations of $CuIn(S_ySe_{(1-y)})_2$, $CuGa(S_ySe_{(1-y)})_2$, $Cu(In_{(1-x)}Ga_x)S_2$ and $Cu(In_{(1-x)}Ga_x)Se_2$ that obey their respective bowing parameters [28], the bandgap of the penternary $Cu(In_{(1-x)}Ga_x)(S_ySe_{(1-y)})_2$ may be described as a function of x and y. The range of bandgaps for the penternary CIGSSe absorber could then be derived from the quantity of these elements.

There is the possibility of widening the bandgap from the absorber surface to increase the conduction band minimum to a higher energy to reduce the CBO between the absorber and buffer [29]. Another advantage of a wider absorber surface bandgap is the increment of light absorbance at the front of the absorber, potentially increasing the possible current generated [3].

A relation for bandgap and valence band minimum of Zn(O,S) was established with the following equation that relates to energy bandgap values of 3.6 eV for ZnS and 3.2 eV for ZnO [30] and a bowing parameter $b = 3.0$ eV [1, 31],

$$E_g(\mathrm{Zn(O_{1-x}S_x)}) = x \cdot E_g(\mathrm{ZnS}) + (1-x) \cdot E_g(\mathrm{ZnO}) - b \cdot (1-x)x \tag{6.2}$$

The following equation describes the relationship between the conduction band offset (ΔE_{CB}), valence band offset (ΔE_{VB}), and the bandgaps of absorber E_g(CIGSSe) and buffer E_g(Zn(O,S), respectively [32],

$$\Delta E_{CB} = E_g(\mathrm{Zn(O,S)}) - E_g(\mathrm{CIGSSe}) - \Delta E_{VB} \tag{6.3}$$

For tunable ALD depositions, the extreme cases where [O]:[S] = 1:0 or 1:1 were first considered. From previous studies by other groups, pure ZnO yielded devices of lower V_{OC} compared to a Zn(O,S) buffered device, which translated into lower efficiencies [21]. On the S-rich side where [O]:[S] = 0:1, devices were found to have low efficiencies due to photocurrent blockage originating from an extremely high ΔE_{CB}.

Due to these considerations, moderate [O]:[S] values of 6:1–2:1 in the Zn(O,S) buffer were considered for fabrication into devices, and two compositions of CBD prepared samples were also evaluated for a comparison mainly based on composition, at a range where the $\Delta E_{CB} \approx 0$ eV. In this direction, absorbers with varying surface bandgaps were furnished with these different Zn(O,S) stoichiometries. In the experimental discussion in the subsequent sections, the materials and electrical properties of the solar cells were characterized to understand what leads to a highly efficient Zn(O,S)/CIGSSe solar cell which avoids metastability.

6.3.2. Absorber composition

An initial evaluation of the four absorber surface was made. XPS scans were obtained after a low voltage Ar-ion etching (5 s) of the CIGSSe surface to remove undesired carbon and other oxidized CIGSSe materials. Detected binding energies of the Cu $2p^{3/2}$, Ga $2p^{3/2}$, In $3d^{5/2}$, S $2p^{3/2}$, and Se $3d^{5/2}$ peaks were similar to related literature on CIGS characterization, and were tabulated in Table 6.1 [33]. The atomic ratio of elements at the surface of each CIGSSe absorber were quantified by these core levels of the CIGSSe material using the sensitivity factors from the database. However, it was important to note that a perfect stoichiometric CIGSSe was unavailable for calibration purposes, so the derived atomic ratios were not absolute but relative values.

Table 6.1 Binding energy of CIGSSe elements of four different absorbers surfaces (A, B, C, and D) based on the peaks for Cu $2p^{3/2}$, Ga $2p^{3/2}$, In $3d^{5/2}$, S $2p^{3/2}$, and Se $3d^{5/2}$.

Abs Surface	**A**	**B**	**C**	**D**
Cu $2p^{3/2}$	932.68	932.69	932.77	932.65
Ga $2p^{3/2}$	1117.91	1117.84	1118.61	1118.38
In $3d^{5/2}$	445.05	444.94	444.96	445.05
S $2p^{3/2}$	161.98	161.83	161.91	161.95
Se $3d^{5/2}$	54.24	54.35	54.20	54.21

The atomic ratios of elements [Cu], [In], [Ga], [S], and [Se] which were present at the surface of the absorber were obtained from XPS plotted as Figure 6.2(a). On the elemental breakdown of the four absorbers, the distribution of [Cu] and [S] appeared to differ the most. Since atomic ratios of a certain element with respect to another yielded more information about the absorber properties, they were tabulated to understand how a high or low ratio of certain elements affected the bandgap of the absorber or form certain undesired binary phases/defects in the absorber. The calculated atomic content for each absorber are presented in Figure 6.2(b). Also, the [S]/[Se] and [Cu]/[Ga]+[In] (CGI) ratios were tabulated in the same figure.

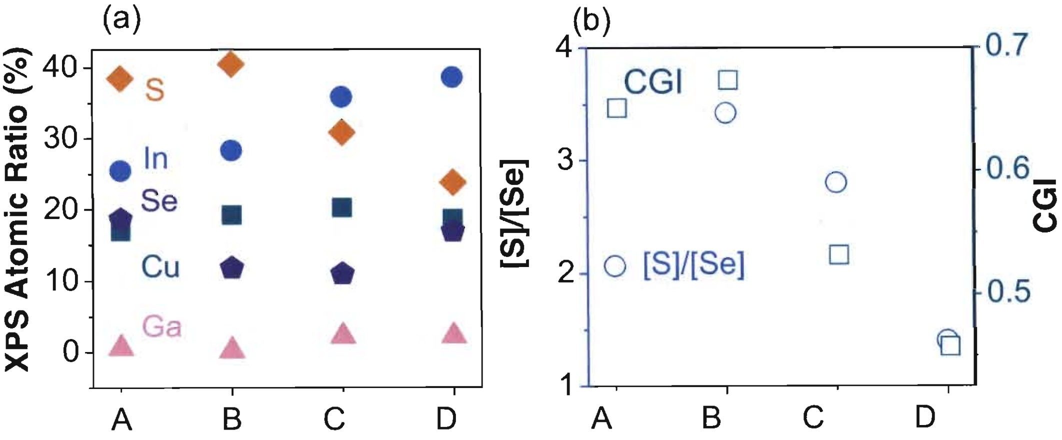

Figure 6.2 (a) XPS compositions of [S], [In], [Se], [Cu], and [Ga] at the surfaces of bare absorbers A, B, C, and D, and (b) corresponding [Cu]/[Ga]+[In] (CGI) and [S]/[Se] ratios for these absorbers.

To compare the performance of absorbers on an equal basis, devices were made with all absorbers with the following Zn(O,S) buffer combinations: [O]:[S] = 6:1, 4:1, and 2:1. Since an optimized efficiency of 16.5% was achieved on absorber B on Zn(O,S) [O]:[S] = 4:1, the performance of all absorbers at this stoichiometry of buffer were plotted in Figure 6.3 to compare their different response to annealing and light soaking. Clearly, absorbers A and D required annealing at 200 °C for 30 min to gain V_{OC}. Additional gains from light soaking of these devices came from the *FF*. Absorber C showed little improvement from the annealing step, and most of the gain came from the *FF* during light soaking. For absorber B, there was a negligible change as fabricated and after post-annealing and light soaking treatment.

Amongst the four absorbers, the copper content relative to gallium and indium was the highest for absorber B. Consistent with record efficiency solar cells which had a tendency to be Cu-excess [34], the highest efficiency solar cells in this series of experiments had the highest absorber CGI relative to the rest.

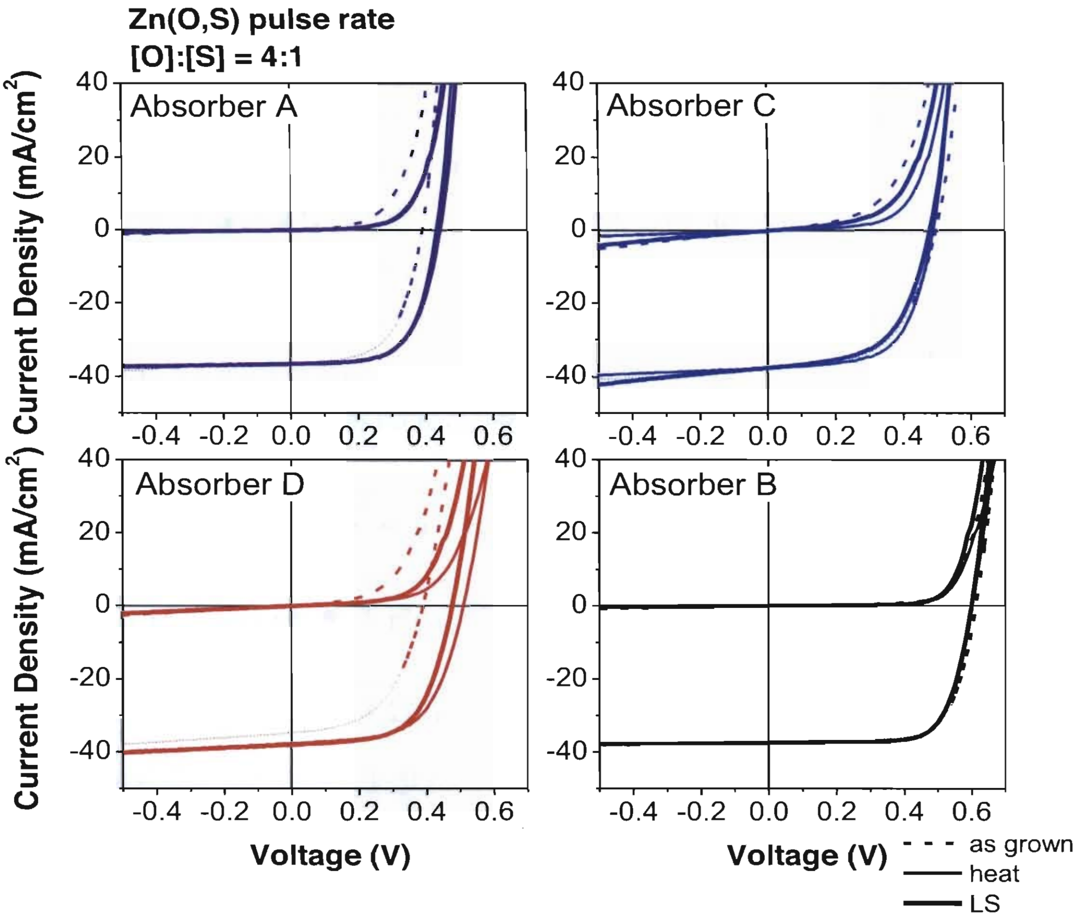

Figure 6.3 Absorbers A, B, C, and D prepared with [O]:[S] = 4:1 in the buffer, 1) as-fabricated, 2) after 30 min 200 °C annealing, 3) after 30 min light soaking under 1 Sun condition.

Thereafter, absorber B was selected for the next evaluation with different Zn(O,S) stoichiometries prepared with both ALD and CBD to give a comprehensive understanding on which stoichiometry is best used to avoid metastability. The range of Zn(O,S) stoichiometries tended to avoid a large ΔE_{CB} and all had high efficiencies after hot light soaking.

6.3.3. Buffer composition

XPS scans were obtained for different buffer compositions after a low voltage Ar-ion etching (5 s) of the Zn(O,S) buffer surface to remove undesired carbon and other oxidized Zn(O,S) material. Detected binding energies of the Zn $2p^{3/2}$, O $1s$, and S $2p^{3/2}$, peaks were similar to related literature on CIGS characterization, and were tabulated in Table 6.2 [33]. The ratio of each element at the surface of each Zn(O,S) buffer were quantified by these core levels of the Zn(O,S) material using the sensitivity factors from the database. As with the CIGSSe absorber, relative values were obtained for the Zn(O,S) material.

Table 6.2 Binding energy of Zn(O,S) elements based on the peaks for Zn $2p^{3/2}$, O $1s$, and S $2p^{3/2}$.

Buffer Surface	**1:0**	**6:1**	**4:1**	**1:1**	**CBD 1**	**CBD 2**
Zn $2p^{3/2}$	1022.5	1022.3	1022.1	1022.1	1022.3	1021.8
O $1s$	530.7	530.4	530.4	530.3	530.7	530.0
O $1s$ (OH)					532.4	531.5
S $2p^{3/2}$	162.1	161.7	161.7	162.0	163.5	161.6

The buffers, either prepared with ALD or CBD techniques, were categorized systematically in increasing sulfur content and plotted in Figure 6.4. For the ALD technique, none of the buffers had a characteristic peak for hydroxides. Hydroxides were persistent after hot light soaking of the CBD technique. This side product was assumed to be inert and not contribute much to the device characteristics [35]. It was evaluated on these CBD samples that the grading effect was not strongly present in the buffer layers prepared (Figure 6.4(c) and (d)), hence in subsequent analyses values were based on an average representative of the whole layer. Also, since the absolute atomic ratio (%) did not make much sense on its own, the [S]/([S]+[O]) and [S]/[Zn] ratios were discussed in more detail in the following section.

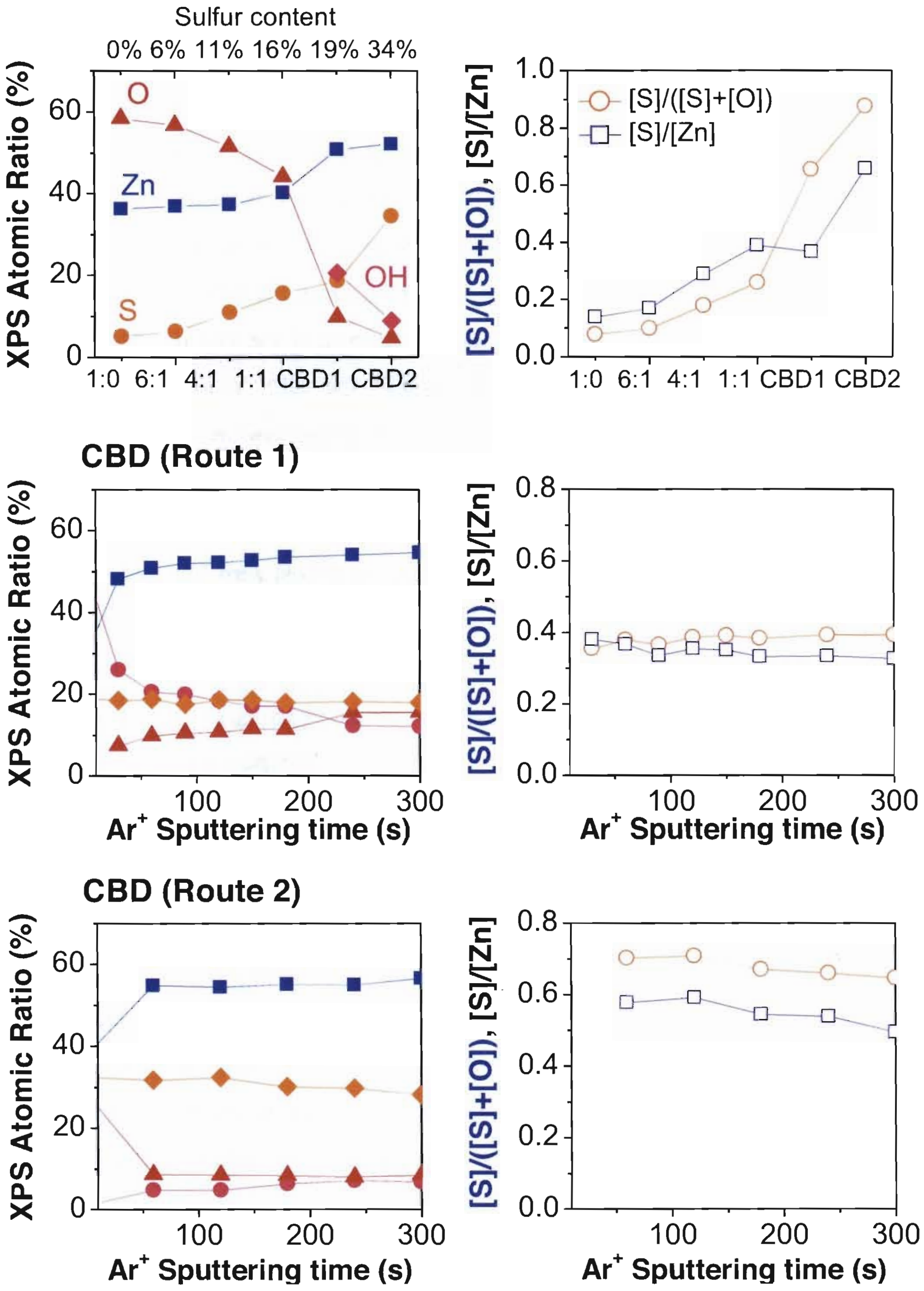

Figure 6.4 Chemical composition of elements present in ZnO or Zn(O,S) films deposited on CIGSSe in ALD, and their respective [S]/[Zn] and [S]/([S]+[O]) ratios. CBD samples were depth sputtered to evaluate effect of grading, which were found to be largely absent as shown in (c) and (d).

The following plot of ALD and CBD prepared devices in Figure 6.5 show the I-V parameters 1) as fabricated and 2) after HLS. For all ALD devices ranging from [O]:[S] = 6:1–2:1, V_{OC} and J_{SC} were constant as fabricated and not much was gained after hot light soaking. For [O]:[S] = 6:1–4:1, gains in *FF* were also negligible, leading to an increase in efficiency for both devices due to HLS. For [O]:[S] = 2:1, the gain in *FF* was more obvious, implying that an increase in sulfur in the buffer already started to influence the barrier at the absorber/buffer interface, even if the conduction band offset between absorber and buffer remain unchanged at the XPS ratio evaluated. An increase in conductivity due to increasing sulfur content could also be speculated to affect *FF* [36]. On the other hand, CBD prepared devices which were much more sulfur-rich (19% and 34% sulfur respectively from XPS) had to undergo HLS to gain in V_{OC} and J_{SC}. Furthermore, the more sulfur-rich case had an almost zero V_{OC} and J_{SC} immediately after window deposition and gained more during the HLS step. For ease of comparison, the atomic ratio of sulfur evaluated by XPS were used in the subsequent discussion to compare between the ALD and CBD devices' performances.

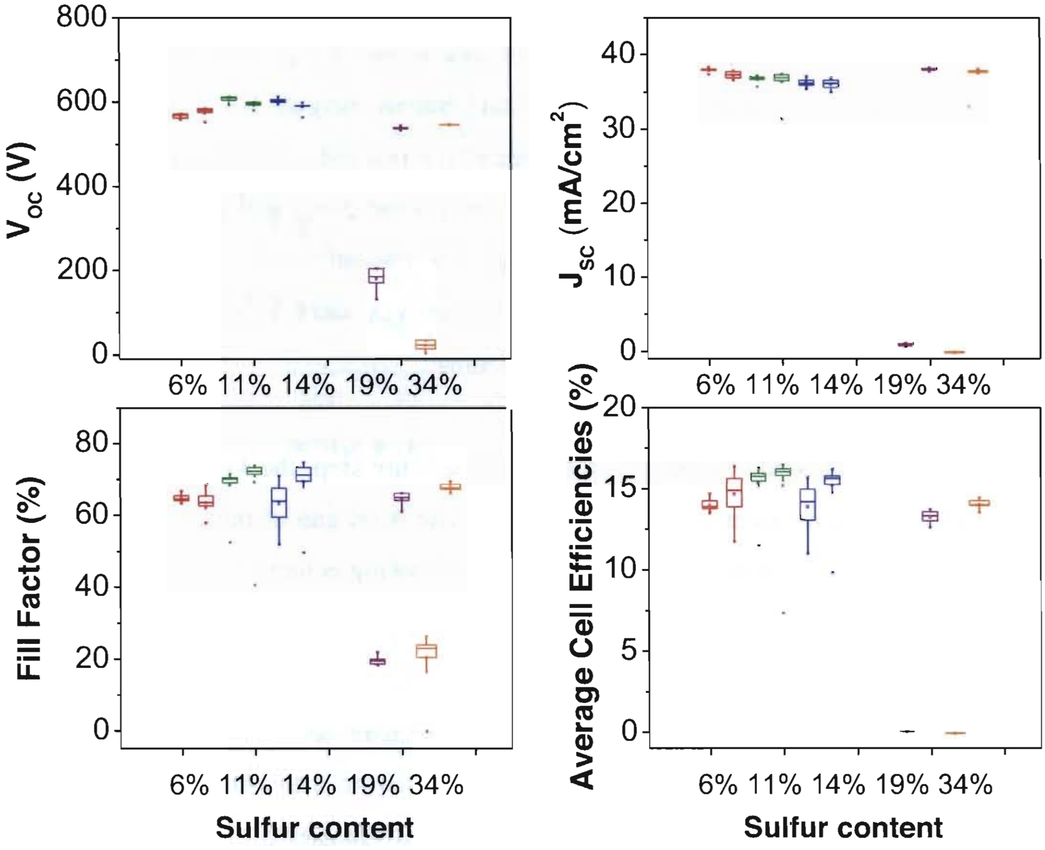

Figure 6.5 Plots of I-V parameters for different Zn(O,S) [O]:[S] ratios prepared with ALD and CBD, with their sulfur atomic% evaluated by XPS.

When one uses the same absorber and vary the buffer content, it became obvious that the sulfur content in the buffer played a key role in contributing towards metastability. Combining both the considerations of absorber and buffer, the key finding was that it appears that regardless of absorber, an application of Zn(O,S) of 11% sulfur ([O]:[S] $\leq$ 4:1) is necessary for the control of metastability.

6.3.4. Device properties

On top of the material properties obtained by XPS surface characterization of both layers, electrical properties in the form of I-V-T measurements were performed for two series of devices.

To identify whether the recombination occurs at the interface or the bulk of the CIGS absorber, and to calculate the back contact barrier height, I-V-T measurements were performed for individual cells at their respective relaxed or light soaked state. The light soaked cell was transferred to the cryostat and cooled down to 77 K immediately after 24 h Xenon lamp irradiation and illuminated I-V measurement. A temperature range of 77–360 K was selected for this study. I-V curves were recorded both under 1 Sun illumination and in the dark for all temperatures.

From the illuminated I-V curves at each temperature step, the V_{OC} values were extracted and plotted against temperature (Figure 6.6). The band gap of the absorber was found by extrapolating the V_{OC} to 0 K according to the following equation.

$$V_{OC} = \frac{E_a}{q} - \frac{AkT}{q}\ln\left(\frac{J_{00}}{J_L}\right) \tag{6.4}$$

Where E_a is the activation energy of the dominant recombination mechanism, q is elementary charge, A is the diode ideality factor, k is the Boltzmann constant, T is temperature in Kelvin, J_{00} is the saturation current density prefactor and J_L is the light generated current density. At 0 K, E_a/q directly equals the V_{OC} value since the temperature dependent factor becomes zero [37].

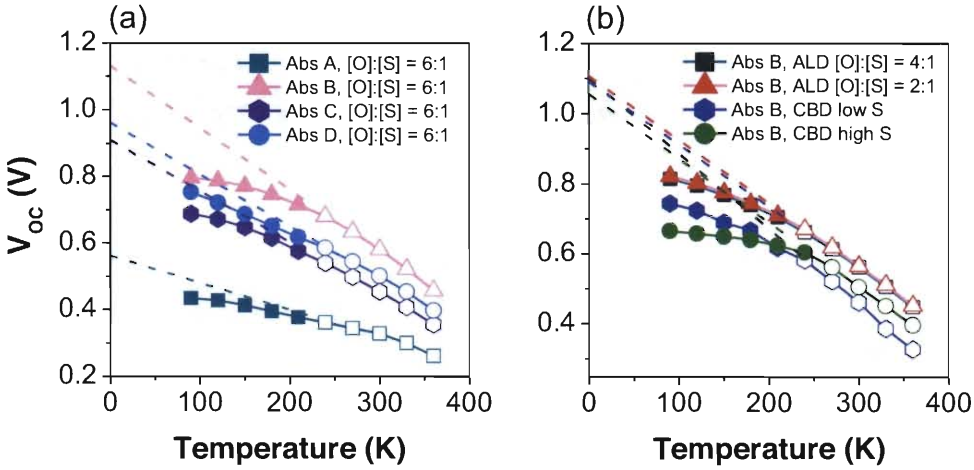

Figure 6.6 (a) Devices made with absorbers A, B, C, D and Zn(O,S) [O]:[S] = 6:1, and (b) Devices made with absorber B with various Zn(O,S) stoichiometries prepared with ALD and CBD techniques.

At the higher temperature regime of 240–360 K, there was a linear decrease of V_{OC} with increasing temperature from which E_a of the dominant recombination mechanism could be extrapolated at T = 0 K. At lower temperatures below 240 K, V_{OC} became saturated and temperature independent due to an additional back contact barrier [38]. From this deviating trend line, it was possible to calculate the difference between the extrapolated V_{OC} of relaxed and light soaked devices and get the value for the back contact barrier height at 0 K [39, 40].

The first series (Figure 6.6(a)) consisted of absorbers A, B, C, and D on a standard 6% sulfur ([O]:[S] = 6:1), in order to understand why they yielded different cell efficiencies and metastabilities with the same Zn(O,S) combination. The second series (Figure 6.6(b)) consisted different stoichiometries of buffers prepared by ALD or CBD on top of the high efficiency absorber B. All absorber bandgap values were found to be 1.1 eV by external quantum efficiency measurements performed at room temperature (Figure 6.7).

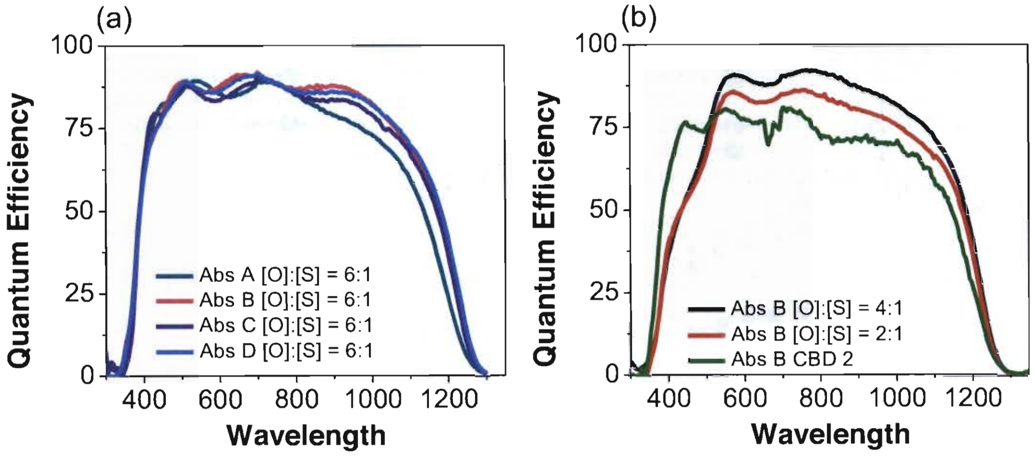

Figure 6.7 EQE measurements of (a) Devices made with absorbers A, B, C, D and Zn(O,S) [O]:[S] = 6:1, and (b) Devices made with absorber B with various Zn(O,S) stoichiometries prepared with ALD and CBD techniques.

The evaluation of the first series showed that the extrapolated bandgap at 0 K for absorber B was equivalent to the bandgap extracted from EQE measurement. From this value, it was inferred that bulk recombination is the major recombination pathway in the ideal device. On the other hand, the extrapolated bandgaps at 0 K for A, C and D were lower than the bandgaps extracted by EQE ($E_g = 1.1$ eV). When comparing [S]/[Se] ratios determined by XPS in Fig. 6.2, there was a trend of decreasing S at the absorber surfaces of B, C, and D, and this was expected to lead to a decrease in bandgap of the material at the surface in this order [29]. As absorber A differed from B, C, and D due to low [Cu] and high [S] content, there was a tendency to form CuS or CuSe binary compounds which lowered the bandgap of the material. Additionally, with a large excess of [In]/[Cu] (not tabulated) and low CGI in Absorber D, there will be a tendency for this absorber to form V_{Cu} in the absorber, which might affect the electrical properties in complete devices made with this absorber. From extrapolated bandgap values and XPS data, interface recombination dominated the recombination pathways in devices made with absorbers A, C, and D.

Concerning the second series, despite differing V_{OC} values at room temperature, bulk recombination occurred for all devices independent of the buffer stoichiometry or fabrication method. The back contact barrier was observed to be higher for CBD-buffered devices than ALD-buffered devices, but this effect was more obvious only at low temperatures of 90–240 K. This could be due to the increasing bandgap of Zn(O,S) when sulfur content increase, while keeping the absorber bandgap constant. This results in a larger back contact barrier when everything else remains constant.

From these two series of experiments, major recombination pathways could be concluded to be more dependent on the intrinsic absorber properties than that of the buffer stoichiometry.

6.4. Dark storage test and subsequent light soaking

Dark storage tests were performed for both ALD and CBD devices made with the absorber B, as it yielded the highest efficiency amongst the different absorbers evaluated here. From Figure 6.8, the best combination to avoid metastability over long term (>3 month) dark storage at ambient room temperature was to keep the [O]:[S] low, i.e. 11% sulfur. Even when ALD was utilized to prepare the buffer, any increase in sulfur stoichiometry (e.g. 13% sulfur) would lead to metastability in the device in the form of a crossover of the dark and illuminated I-V curve at the device's relaxed state. When comparing this with the CBD prepared devices of 19% S and 34% S, one can also observe the same trend. The device of 19% S showed a slight loss of efficiency accompanied with *FF* loss due to dark storage relaxation. On the other hand, the device of 34% S, under the same dark storage condition, showed a much more significant loss of cell efficiency with a characteristic kink in the fourth quadrant in its I-V curve for the relaxed device.

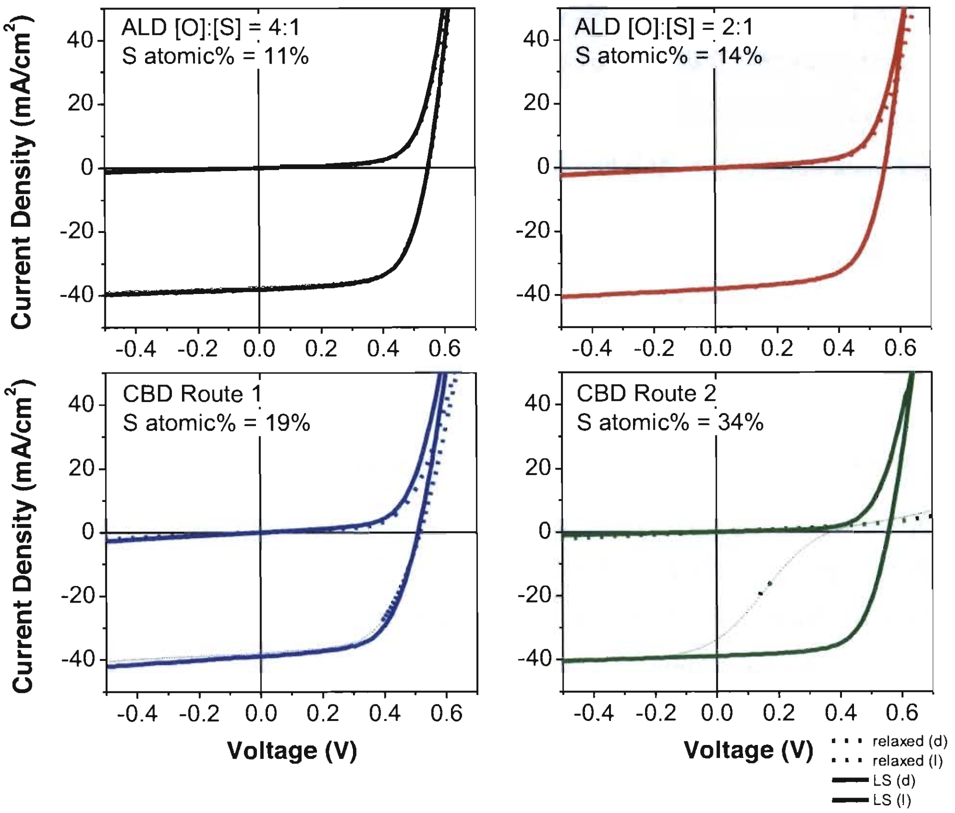

Figure 6.8 I-V curves after 3 month dark storage under ambient (dashed lines) and after a subsequent light soak (solid lines) for solar cells made with Zn(O,S) buffer (1) ALD [O]:[S] = 4:1, 11% sulfur, (2) ALD [O]:[S] = 2:1, 13% sulfur (3) CBD Route 1, 19% sulfur, and (4) CBD Route 2, 34% sulfur.

When changing the [S]/([S]+[O]) ratio of the buffer by methods such as ALD or CBD, the most common reason cited for the formation of the I-V kink is the conduction band offset between the buffer and absorber. In order to dispute that claim that CBO strongly affected metastability, the ratios of Zn(O,S) prepared had ([S]/([S]+[O]) of 0.3-0.7) translating into bandgap variations between 2.6-2.8 eV) [1]. This implies a negligible change to the CBO within the range of these devices prepared. Nevertheless, significant differences in the I-V characteristics were observed. Within a small window of 0–39% sulfur, the following could be quantified:

(1) Devices consisting of absorbers A, C, and D required HLS and had a wide range of efficiencies when the Zn(O,S) stoichiometry was kept at 11% sulfur (η=10–14%)

(2) For the same Zn(O,S) stoichiometry which constituted of 11% sulfur, devices made with absorber B had negligible metastability and did not require HLS to achieve a high efficiency (η=15–16%)

(3) Dark storage at 25 °C in air led to different extents of cell efficiency loss in accordance to sulfur content in the buffer. This effect was observed in the following magnitude of metastability, CBD Route 2, 34% sulfur > CBD Route 1, 19% sulfur > ALD [O]:[S] = 2:1, 13% sulfur. On the other hand, absorber B with 11% sulfur had no relaxation during the dark storage as negligible change in I-V parameters were observed from initial to dark storage to light soaked device.

6.5. Conclusion

Thus far, literature studies have focused the link between a small CBO to high cell efficiencies. This results from increment of built-in voltage that improves the collection of photogenerated carriers in absorber and reduction of recombination to improve J_{SC} and V_{OC}. At the same time, a reduction of saturation current of the dark I-V curve leads to slight improvement of photocurrent [2]. In this chapter, it was shown that even when different stoichiometries of Zn(O,S) may have the same CBO relative to the absorber, metastability still persists. The exact stoichiometry of each deposited ZnO or Zn(O,S) thin film, derived by XPS measurements allow the following conclusion to be drawn: (1) a low [S]/[Zn] ratio (between 0-11% sulfur) shows a low metastability and minimum changes after HLS treatment, (2) a low and optimal [S]/([S]+[O]) ratio, especially in the case of 11% sulfur, ensures low metastability and high cell efficiencies. From the absorber side, a high efficiency can be ensured from a high [S]/[Se] ratio of 3.4, and a high CGI ratio of 0.65.

References

[1] B. K. Meyer, A. Polity, B. Farangis, Y. He, D. Hasselkamp, T. Krämer, C. Wang, *Appl. Phys. Lett.* **2004**, *85*, 4929–4931.

[2] C. Platzer-Björkman, T. Törndahl, D. Abou-Ras, J. Malmström, J. Kessler, L. Stolt, *J. Appl. Phys.* **2006**, *100*, 044506.

[3] C. H. Fischer, M. Bär, T. Glatzel, I. Lauermann, M. C. Lux-Steiner, *Sol. Energy Mater. Sol. Cells* **2006**, *90*, 1471–1485.

[4] T. Nakada, M. Hongo, E. Hayashi, *Thin Solid Films* **2003**, *431–432*, 242–248.

[5] M. Igalson, C. Platzer-Björkman, *Sol. Energy Mater. Sol. Cells* **2004**, *84*, 93–103.

[6] http://www.solar-frontier.com/eng/news/2015/C051171.html, **2015**.

[7] K. Kushiya, M. Tachiyuki, T. Kase, Y. Nagoya, T. Miura, D. Okumura, M. Satoh, I. Sugiyama, O. Yamase, in *Photovoltaic Specialists Conference, 1997, Conference Record of the Twenty-Sixth IEEE*, **1997**, pp. 327-330.

[8] K. Kushiya, S. Kuriyagawa, K. Tazawa, T. Okazawa, M. Tsunoda, in *Conference Record of the 2006 IEEE 4th World Conference on Photovoltaic Energy Conversion, Vol. 1*, **2006**, pp. 348–351.

[9] M. Igalson, A. Urbaniak, P. Zabierowski, H. A. Maksoud, M. Buffiere, N. Barreau, S. Spiering, *Thin Solid Films* **2013**, *535*, 302–306.

[10] T. Nakada, M. Mizutani, Y. Hagiwara, A. Kunioka, *Sol. Energy Mater. Sol. Cells* **2001**, *67*, 255–260.

[11] M. Bär, A. Ennaoui, J. Klaer, T. Kropp, R. Sáez-Araoz, S. Lehmann, A. Grimm, I. Lauermann, C. Loreck, S. Sokoll, H.-W. Schock, C.-H. Fischer, M. C. Lux-Steiner, C. Jung, *J. Appl. Phys.* **2006**, *100*, 064911.

[12] W. Witte, D. Hariskos, A. Eicke, R. Menner, O. Kiowski, M. Powalla, *Thin Solid Films* **2013**, *535*, 180–183.

[13] K. Kushiya, O. Yamase, *Jpn. J. Appl. Phys.* **2000**, *39*, 2577.

[14] I. L. Eisgruber, J. E. Granata, J. R. Sites, J. Hou, J. Kessler, *Sol. Energy Mater. Sol. Cells* **1998**, *53*, 367–377.

[15] A. O. Pudov, J. R. Sites, M. A. Contreras, T. Nakada, H. W. Schock, *Thin Solid Films* **2005**, *480–481*, 273–278.

[16] D. Hariskos, M. Ruckh, T. Walter, H. W. Schock, *1st WCPEC (IEEE, Hawaii)* **1994**, 91.

[17] J. Serhan, Z. Djebbour, W. Favre, A. Migan-Dubois, A. Darga, D. Mencaraglia, N. Naghavi, G. Renou, J. F. Guillemoles, D. Lincot, *Thin Solid Films* **2011**, *519*, 7606–7610.

[18] S. Sharbati, J. R. Sites, *IEEE J. Photovoltaics* **2014**, *4*, 697–702.

[19] V. Probst, I. Koetschau, E. Novak, A. Jasenek, H. Eschrich, F. Hergert, T. Hahn, J. Feichtinger, M. Maier, B. Walther, V. Nadenau, *IEEE J. Photovoltaics* **2014**, *4*, 687-692.

[20] A. Shimizu, S. Chaisitsak, T. Sugiyama, A. Yamada, M. Konagai, *Thin Solid Films* **2000**, *361–362*, 193–197.

[21] E. B. Yousfi, B. Weinberger, F. Donsanti, P. Cowache, D. Lincot, *Thin Solid Films* **2001**, *387*, 29–32.

[22] T. Kobayashi, T. Kumazawa, L. Kao, T. Nakada, *Sol. Energy Mater. Sol. Cells* **2013**, *119*, 129–133.

[23] J. A. Woollam, *http://www.jawoollam.com/pdf/Alpha_Brochure.pdf*.

[24] P. Němec, I. Němec, P. Nahálková, Y. Němcová, F. Trojánek, P. Malý, *Thin Solid Films* **2002**, *403–404*, 9–12.

[25] M. P. Seah, I. S. Gilmore, S. J. Spencer, *Surf. Sci.* **2000**, *461*, 1–15.

[26] J. H. Scofield, *J. Electron. Spectrosc. Relat. Phenom.* **1976**, *8*, 129–137.

[27] M. Bär, W. Bohne, J. Röhrich, E. Strub, S. Lindner, M. C. Lux-Steiner, C.-H. Fischer, T. P. Niesen, F. Karg, *J. Appl. Phys.* **2004**, *96*, 3857–3860.

[28] S. H. Wei, A. Zunger, *J. Appl. Phys.* **1995**, *78*, 3846–3856.

[29] M. Turcu, I. M. Kötschau, U. Rau, *J. Appl. Phys.* **2002**, *91*, 1391–1399.

[30] O. Madelung, *Semiconductors: Data Handbook*, Springer Berlin Heidelberg, **2012**.

[31] A. Grimm, J. Just, D. Kieven, I. Lauermann, J. Palm, A. Neisser, T. Rissom, R. Klenk, *Phys. Status Solidi RRL* **2010**, *4*, 109–111.

[32] T. Adler, M. Botros, W. Witte, D. Hariskos, R. Menner, M. Powalla, A. Klein, *Phys. Status Solidi A* **2014**, *211*, 1972–1980.

[33] T. Adler, TU Darmstadt **2013**.

[34] K. Sakurai, R. Hunger, R. Scheer, C. A. Kaufmann, A. Yamada, T. Baba, Y. Kimura, K. Matsubara, P. Fons, H. Nakanishi, S. Niki, *Prog. Photovoltaics Res. Appl.* **2004**, *12*, 219–234.

[35] J. B. Varley, V. Lordi, *Appl. Phys. Lett.* **2013**, *103*, 102103.

[36] S. Tao, J. T. McGoffin, J. R. Sites, *IEEE J. Photovoltaics* **2014**, *4*, 942–947.

[37] V. Nadenau, U. Rau, A. Jasenek, H. W. Schock, *J. Appl. Phys.* **2000**, *87*, 584–593.

[38] C. P. Thompson, S. Hegedus, W. Shafarman, D. Desai, in *33rd IEEE Photovoltaic Specialists Conference*, **2008**, pp. 1–6.

[39] T. Eisenbarth, T. Unold, R. Caballero, C. A. Kaufmann, H.-W. Schock, *J. Appl. Phys.* **2010**, *107*, 034509.

[40] T. Eisenbarth, R. Caballero, M. Nichterwitz, C. A. Kaufmann, H.-W. Schock, T. Unold, *J. Appl. Phys.* **2011**, *110*, 094506.

Chapter 7

Summary and Future Work

7.1. Results from Thermal Stability Tests

From the initial evaluation of cadmium sulfide (CdS) and zinc oxysulfide (Zn(O,S)) buffered CIGSSe solar cells, it could be shown that regardless of buffer, all solar cells studied in this thesis passed the accelerated stability test at 105 °C over 1000 h. However, it was noted that during the experiment, Zn(O,S) buffered devices experienced a gradual loss of efficiency over the 1000 h time period. Although this effect was recoverable with a post-experiment light soaking step, the effect, termed "metastability", caused a reduction of cell efficiency in days, and required some time to improve under sunlight. This additional light soaking step was impractical for modules deployed externally due to the inability to predict the minimum expectable output of the solar cell.

The major findings of Chapter 4 were that Zn(O,S) buffered devices prepared with chemical bath deposition (CBD) showed a decrease in cell efficiency at both 60 °C and 105 °C dark storage, and the rate was governed by the temperature applied.

Additionally, there was an *acceleration* of cell relaxation for Zn(O,S) buffered devices after light soaking recovery of devices heated over 1000 h at 105 °C. These recovered devices that experienced dark storage at 25 °C showed an acceleration of cell efficiency drop from its initial rate of > 5 days to less than 1 day. XPS of the CIGSSe/Zn(O,S) bilayer revealed that there was an outdiffusion of sulfur after 1000 h of heating from the absorber into the buffer bulk. This indicated a consistent trend of increasing metastability in Zn(O,S) buffer with higher sulfur content. The postulation that the amount of sulfur played a role in metastability of these Zn(O,S) buffered solar cells prompted a deeper study of the mechanism(s) of metastability undertaken in Chapter 5 with experiments and supported by SCAPS-1D simulations.

7.2. Origins of Metastability in CIGSSe/Zn(O,S) Devices

It has been confirmed in Chapter 5 that defects in the *p-n* junction or its interface can create a barrier that impedes the forward current of an illuminated CIGS solar cell. The root cause(s) have been summarized in Figure 7.1.

The three factors that may contribute to a transient reduction of efficiency in Zn(O,S)/CIGSSe devices are:

(1) Buffer

(2) Absorber

(3) Back contact

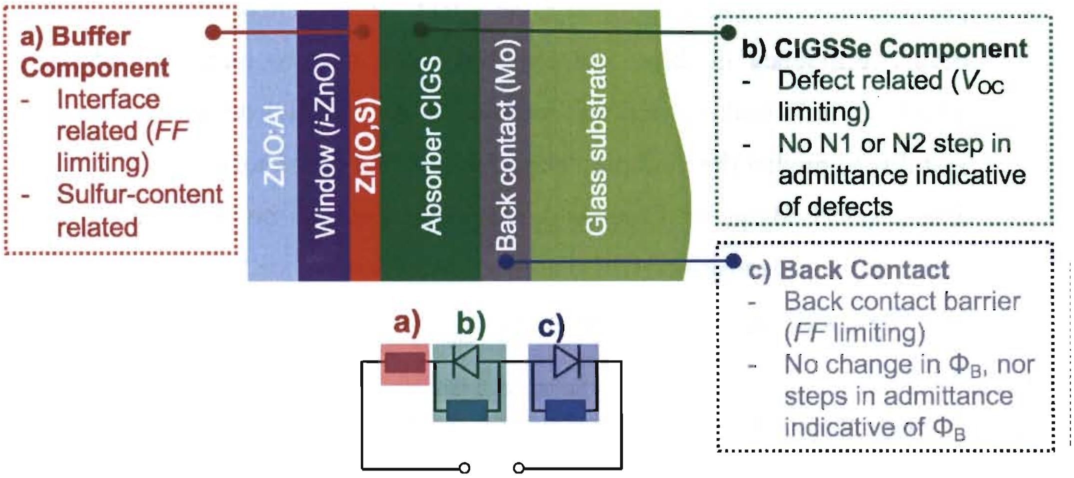

Figure 7.1 Possibility of contribution to metastability mechanism from a) buffer, b) CIGSSe absorber, and c) back contact.

One could rule out the contributions of the absorber with the following reasoning: from admittance spectroscopy of good and poor absorbers at their relaxed or light soaked states, negligible change in capacitance or activation energy was observed for all cases, indicating that the contribution from the defects in the absorber was not apparent in metastability.

Furthermore, the main recombination pathways, determined from the V_{OC} (0 K), whether they are bulk recombination for good devices or interface recombination for poor devices, stayed constant at the relaxed and light soaked states. Also, it was possible to rule out the contribution of the back contact induced by light soaking as neither the back contact barrier, derived from the low-temperature regime of <200 K, nor the N1 defect in admittance spectroscopy differed when characterizing both relaxed and light soaked devices.

Concerning the buffer component, it was verified in this chapter that the origin of *FF* losses comes from the buffer by SCAPS-1D simulation. Of which, the likely reasons were 1) increased CBO between the absorber and buffer that comes from increasing bandgap, and 2) increasing quantity of V_{Zn} acceptor in the Zn(O,S) which inevitably changed it from an *n*-type compensated semiconductor to slightly *p*-type. The presence of a kink in the illuminated I-V curve when excessive acceptor states are present was verified with SCAPS-1D simulation, and the CBO between the absorber and buffer led to a crossover of the dark and illuminated I-V curve at this acceptor density.

The following possibilities of interface issues arising from the absorber/buffer/window interface may then contribute to the kink in the illuminated I-V curve:

(a) A highly doped absorber surface populated with metastable states or defects (the so-called “p+ layer”)
(b) Metastable charges in the buffer layer
(c) Charged interface states at the absorber/buffer interface
(d) Charged interface states at the buffer/window interface

Of which, (a) was not likely due to admittance and I-V-T measurements showing unchanged activation energy/recombination pathway before and after light soaking. (d) was also not plausible as the TRPL experiments have demonstrated that the impeded charge separation is a result of changing composition of the buffer resulting in a barrier at the absorber/buffer interface, and the main contributor is not the buffer/window emitter.

Finally, (b) and (c) are the plausible causes leading to the kink. Since the main variation came from the buffer, it was possible to isolate the main contributor to the metastable behavior of these devices as a result of the changing the properties of the buffer.

With this simulated hypothesis, TRPL performed on ALD-Zn(O,S) buffered devices showed that with increasing sulfur in the buffer, effectiveness of charge separation was reduced and there was an increase in radiative recombination, especially when the ratio of [O]:[S] was 2:1. Metastable devices were apparent at [O]:[S] = 2:1 and even higher sulfur contents when the Zn(O,S) was prepared by ALD. In this study, the metastable 2:1 device showed an improvement of cell efficiency and reduction of I-V crossover after it was light soaked. Correspondingly, the TRPL showed disappearance of its τ_2 after light soaking, indicating an improvement of charge separation and reduction of radiative recombination.

7.3. Mitigation Strategies

The experiments in Chapter 5 proved that the metastability behavior of Zn(O,S)/CIGSSe devices does not only depend on the buffer, but rather, the combination of the absorber and buffer leads to an ideal device that has high efficiency and low metastability.

The correlation of the buffer [O]:[S] ratio, independent of deposition technique of ALD and CBD, were applied on the CIGSSe absorber and their metastability evaluated. It was generally observed that regardless of absorber surface, a low sulfur content in the buffer (S = 0%–11%) improves the performance of the cells and reduce the requirement for HLS treatment to attain high efficiencies. Aside from that, comparing across different absorber batches, Absorber "B" exhibits the highest efficiency and the lowest metastability for ALD-Zn(O,S) of 6–16% sulfur applied onto the absorber.

Table 7.1 Summary of metastability in devices with varying chemical composition at absorber surface and buffer.

	Zn(O,S) S %					
Abs.	**0**	**6**	**11**	**16**	**19**	**34**
A	O	O	O	Δ	X	X
B		◎	◎	◎		X
C		O	O	O		X
D	O	O	O	X	X	X

Red = ALD (ZnO, $ZnO_{0.85}S_{0.15}$, $ZnO_{0.8}S_{0.2}$, $ZnO_{0.66}S_{0.33}$, $ZnO_{0.5}S_{0.5}$);
Green = CBD ($ZnO_{0.4}S_{0.6}$, $ZnO_{0.3}S_{0.7}$).

◎ = no metastability, O = low metastability, = moderate metastability, X = high metastability.

7.4. Future Work

While a plausible explanation for the mechanism and the subsequent proof-of-concept had been achieved in this PhD thesis with regards to metastabilities in Zn(O,S) buffered CIGSSe devices, there remains a few unaddressed questions.

First, there is now an experimental proof to show that the metastabilities in these solar cells can be quantified by TRPL technique. In order to refine this technique, an external voltage bias might be applied to perturb the *p-n* junction [1, 2] and simulate the I-V curve at points where an electronic barrier appears. V_{OC} related metastabilities have been reported in co-evaporated CIGS devices [3, 4] but not in CIGSSe absorbers prepared by the two-stage sputtering process, as used in the devices here. In order to expand the understanding of metastabilities of Zn(O,S)/CIGSSe devices where the CIGSSe absorber is prepared by co-evaporation, the TRPL characterization technique could be employed to compare any similarities/differences. Furthermore, the different deposition methods of the buffer, e.g. sputtering, CBD, which are commonly used for fabricating modules in industry, could be characterized as full devices and up to the buffer layer with this technique.

Second, even as a method of controlling the stoichiometry of the buffer can be devised to mitigate metastabilities in Zn(O,S)/CIGSSe devices, there are alternative ways to avoid HLS by controlling the quantity of O_2 during window layer sputtering [5] or adding another material like indium in the buffer [6]. Techniques in the direction of buffer/window characterization from the materials, electrical, and optical aspects need to be refined.

The original hypothesis was that metastability in Zn(O,S) buffered CIGSSe devices is attributed to the properties of the CIGSSe/Zn(O,S) heterojunction. It became clear now that within the scope of devices studied in this PhD work that the Zn(O,S) buffer was the main contributor towards metastability. Through a systematic evaluation of ALD Zn(O,S) of various oxygen and sulfur content, an increase of sulfur to 16% and beyond leads to metastabilities in the solar cells. In terms of mechanism, the conventional electrical methods of characterizations, namely admittance spectroscopy (AS) and temperature-dependent current-voltage (I-V-T) measurements, were found ineffective in identifying the change in device characteristics at their relaxed and light soaked states. These conventional electrical characterization techniques were typically utilized to characterize V_{OC} related metastable changes that were correlated to the absorber or the back contact. However, since fill factor related metastabilities occurred with a different mechanism, an alternative method of characterization of the devices were required. As such, it inspired the development of TRPL as a viable method to characterize the effectiveness of charge separation and radiative recombination near the surface of the absorber at the *p-n* junction.

The second part of the thesis, which was based on a hypothesis that the conduction band offset (CBO) matching between the absorber and buffer, was shown to be partially true in solving the problem of metastability in these devices. By comparing the ALD and CBD prepared devices, one can conclude that the high sulfur (19% and 34% sulfur) CBD devices came with a higher than ideal CBO (>0.3 eV) which created an additional barrier between the absorber and buffer for charge transport. However, when comparing the different ALD buffered devices, one might also distinguish that a moderate sulfur content of 16% already leads to metastabilities in the device when the conduction band offset of this device is expected to be the same as a device with less sulfur (6% or 11%). Clearly, the CBO theory alone was unable to explain the observations for these ALD devices, and with the understanding of the mechanism and related simulation results, it was found out that a combination of the CBO theory and increasing amount of V_{Zn} acceptors in the buffer bulk were the reasons that contributed to metastability. As such, an ideal combination for buffer and absorber surface was achieved.

Copyright Clearance Center RightsLink®

Home | Create Account | Help | Live Cha

IEEE
Requesting permission to reuse content from an IEEE publication

Title: Improved Stability of CIGS-Based Thin-Film PV Modules

Conference Proceedings: Photovoltaic Energy Conversion, Conference Record of the 2006 IEEE 4th World Conference on

Author: Kushiya, K.; Kuriyagawa, S.; Tazawa, K.; Okazawa, T.; Tsunoda, M.

Publisher: IEEE

Date: May 2006

LOGIN

If you're a copyright.com user, you can login to RightsLink using your copyright.com credentials. Already **a RightsLink user** or want to learn more?

Thesis / Dissertation Reuse

The IEEE does not require individuals working on a thesis to obtain a formal reuse license, however, you may print out this statement to be used as a permission grant:

Requirements to be followed when using any portion (e.g., figure, graph, table, or textual material) of an IEEE copyrighted paper in a thesis:

1) In the case of textual material (e.g., using short quotes or referring to the work within these papers) users must give full credit to the original source (author, paper, publication) followed by the IEEE copyright line © 2011 IEEE.
2) In the case of illustrations or tabular material, we require that the copyright line © [Year of original publication] IEEE appear prominently with each reprinted figure and/or table.
3) If a substantial portion of the original paper is to be used, and if you are not the senior author, also obtain the senior author's approval.

Requirements to be followed when using an entire IEEE copyrighted paper in a thesis:

1) The following IEEE copyright/ credit notice should be placed prominently in the references: © [year of original publication] IEEE. Reprinted, with permission, from [author names, paper title, IEEE publication title, and month/year of publication]
2) Only the accepted version of an IEEE copyrighted paper can be used when posting the paper or your thesis on-line.
3) In placing the thesis on the author's university website, please display the following message in a prominent place on the website: In reference to IEEE copyrighted material which is used with permission in this thesis, the IEEE does not endorse any of [university/educational entity's name goes here]'s products or services. Internal or personal use of this material is permitted. If interested in reprinting/republishing IEEE copyrighted material for advertising or promotional purposes or for creating new collective works for resale or redistribution, please go to http://www.ieee.org/publications_standards/publications/rights/rights_link.html to learn how to obtain a License from RightsLink.

If applicable, University Microfilms and/or ProQuest Library, or the Archives of Canada may supply single copies of the dissertation.

BACK | CLOSE WINDOW